UNIVERSITY OF CALIFORNIA, SAN DIEGO

Single-Molecule Magnets Assembled from Oxime Stabilized Mn_3^{III} Triangles

A Thesis submitted in partial satisfaction of the requirements for the degree Master of Science

in

Chemistry

by

Casey Justin Stephenson

Committee in charge:

Professor David N. Hendrickson, Chair
Professor William C. Trogler
Professor Michael J. Tauber

2009

The Thesis of Casey Justin Stephenson is approved, and it is acceptable in quality and form for publication on microfilm and electronically:

_____

_____

_____

Chair

University of California, San Diego

2009

To Min-Jung, my family, and to the memory of my mother.

Table of Contents

Chapter Five

List of Figures

Chapter One

Chapter Two

Chapter Three

Chapter Four

Chapter Five

List of Tables

Chapter Two

Chapter Three

Chapter Four

List of Schemes

Chapter Two

Chapter Four

Chapter Five

Acknowledgements

First and foremost I would like to thank my advisor Professor Hendrickson for providing me with the opportunity to work in his lab. Under his guidance I have learned how to become an independent scientist. I would also like to thank my coworkers: my good friend Chris Beedle who first mentored me and got me excited about research, Patrick Feng for his help with magnetic and synthetic problems with the manganese chemistry, Katie Heroux who taught me X-ray crystallography, and Gavin Ogawa for being the finest lackey one could ask for. I'd also like to thank the Figueroa Lab for the use of their glove boxes and solvent system. A big thanks goes to Dr. Rick Wang of the Cohen Lab for the gas adsorption measurements and PXRD analysis. Lastly, I'd like to thank my parents for being so supportive throughout my life.

ABSTACT OF THE THESIS

Single-Molecule Magnets Assembled from Oxime Stabilized Mn_3^{III} Triangles

by

Casey Justin Stephenson

Master of Science in Chemistry

University of California, San Diego 2009

Professor David N. Hendrickson, Chair

A series of progressively larger molecules assembled from oxo-centered Mn_3^{III} triangles is presented. All reported complexes have been characterized by bulk magnetic susceptibility and X-ray diffraction.

A series of three "single decker" trigonal bipyrimidal $[Mn_2^{II}Mn_3^{III}]^{+13}$ single-molecule magnets (SMMs) is reported. The complexes have the general formula of $[NEt_4]_3[Mn_5(R\text{-salox})_3O(N_3)_6X_2]$ where R = H, Me, or Et; and X^- = Cl^- or Br^-. The complexes consist of an oxime stabilized μ_3-O^{2-} Mn_3^{III} triangular core capped with two azide bridged Mn^{II} ions. Complexes were synthesized using oxime ligands with increasingly larger alkyl groups pendent to the oximate carbon. Crystal packing of these alkyl groups induced structural distortions which have marked effects on crystal packing, molecular symmetry, and magnetic exchange interactions.

Structural distortions were induced by crystal packing effects in two "double decker" complexes of the formula $[X]_2[Mn_8(salox)_6O_2(N_3)_6(MeOH)_2Cl_2] \bullet 2S$, where X^+ is either NPr_4^+ or NBu_4^+ and S is either MeOH or $CHCl_3$, which resulted in changes in magnetic behavior. A third compound that is an antiferromagnetic one dimensional chain magnet constructed from Mn_8 units bridged by N_3^- ions is described.

Two larger compounds are also reported, one comprised of four interconnected oxo-centered Mn_3^{III} triangles. The other is a magnetic 3D metal-organic framework (MOF) synthesized using a modified salicylaldoxime. The complex has the formula $[Mn_{13}Na_9O_4(EtO\text{-}salox)_{12}(N_3)_6(MeOH)_6(H_2O)_{10}Cl_3]_\infty$ where EtO-salox is 3-ethoxysalicylaldoxime. The MOF exhibited gas adsorption behavior in addition to magnetic data suggestive of a negative D.

Finally, a salicylaldehyde functionalized fullerene has been synthesized and characterized through NMR and mass spectrometry.

Chapter One

Introduction

1.1 Introduction

Interest in magnets has evolved from the use of loadstone in primitive compasses to a multibillion dollar industry today, with applications ranging from magnetic separators and sensors to high density information storage devices. Currently, hard drives and other magnetic information storage devices are made of ferromagnetic metal oxides. Their ability to store information as bits arises from the ordering of magnetic domains in a spin up or spin down configuration. There is an ever growing interest in increasing the storage density of these devices. In order to accomplish this, the size of the magnetic particles must be decreased. Nanometer-sized magnetic materials have been known for quite some time.[1] Their preparation involved many approaches ranging from electrochemical growth to chemical vapor deposition to the precipitation of colloidal nanoparticles.[2] Fragmentation of metal oxide particles is another route to magnetic nanoparticles. This "top down" approach to the synthesis of nanosized magnetic materials yielded a distribution of particle sizes and shapes which made the characterization of their properties difficult.

The "bottom up" approach consists of using molecules rather than large lattices of metal oxides. The first reported molecular compound to exhibit bulk properties such as magnetic ordering was the ferrimagnetic complex $Mn^{II}Cu^{II}$(pbaOH), where pbaOH is 2-hydroxy-1,3-propylenebis(oxamato).[3] This compound consists of a crystalline, regular array of interacting $Mn^{II}Cu^{II}$ units which exhibits three dimensional magnetic ordering. The family of Prussian blue analogues is another example of this type of magnetic compound, such as the ferrimagnet $Cr^{III}/V^{II}/V^{III}$ analogue which orders at room

temperature.[4] The origin of magnetic properties in these types of systems is the long range magnetic ordering due to intermolecular magnetic exchange interactions.

It was not until 1993 when a molecule that behaved as an individual magnet was discovered.[5] The first such magnetic molecule is the dodecanuclear manganese complex $[Mn_{12}O_{12}(OAc)_{16}(H_2O)_4]\bullet 2CH_3COOH \bullet 4H_2O$ (Mn_{12}-OAc), where OAc^- is the acetate anion, which was first reported in 1980.[6--8] The magnetic core consists of four Mn^{IV} ions arranged in a $Mn_4^{IV}O_4$ cubane core, bridged to eight Mn^{III} ions by μ_2-oxide ions. Antiferromagnetic coupling of the Mn^{IV} ions with the ferromagnetically coupled Mn^{III} ions results in an S = 10 ground state. Because the magnetization had a molecular origin, it lead to the observance of quantum effects in the magnetization hysteresis loops.

Since their first discover, chemists have synthesized hundreds of these single-molecule magnets (SMMs). The majority are manganese carboxylate clusters which range in nucleariy from $[Mn_2]$ to $[Mn_{84}]$.[9, 10] SMMs have been synthesized using a variety of transition metals and lanthanides as well.[11-13] Their study has lead to the discovery of a number of magnetic and quantum phenomena including the observance of regular steps in the magnetization versus hysteresis which is due to quantum tunneling of the direction of magnetization (QTM), thermally assisted tunneling, quantum phase interference (Berry phase), and spin parity effects.[14-19] Furthermore, SMMs have been proposed as candidates for quantum computing. As opposed to a single bit memory which consists of spin up versus spin down states, an S = 10 SMM can have (2S+1) = 21 states.[20]

SMM behavior is the result of a large spin ground state (S) coupled with easy-axis type magnetoanisotropy , characterized by a negative D, where D is the parameter

describing axial zero-field splitting (DS_z^2), which gives rise to a barrier for the reversal of magnetization.[6-8, 21] The thermodynamic barrier (U) to magnetization reversal is given by $|D|S^2$ or $|D|(S-1/4)^2$ for integer and half-integer molecules, respectively. The magnetic bistability of a SMM can be described by the potential energy plot for an S = 10 molecule as shown in Figure 1. As a result of zero-field splitting, the S = 10 ground state splits into (2S+1) = 21 states. At room temperature there is enough thermal energy (kT) for the magnetization to reorient quickly. But as the temperature is lowered in an applied field, only the lowest energy states are populated and a preferred orientation arises. Magnetization can no longer reorient except through quantum tunneling mechanisms. Experiments which characterize quantum tunneling of magnetization (QTM) and other relaxation behavior will now be discussed.

1.2 Magnetization Hysteresis and Quantum Tunneling of Magnetization

As with bulk magnets, SMMs also show magnetization hysteresis. The origin of the hysteresis is not due to a collective behavior such as the irreversible reordering of domain walls as in bulk magnets. In SMMs, hysteresis is the result of an isolated molecule interacting with an external magnetic field. This has been confirmed in experiments where Mn_{12}-OAc molecules were isolated in a frozen glass and shown to still exhibit the same hysteresis loops.[22, 23] At high temperatures, there is a Boltzmann distribution of spin states. The spins of an SMM are flipping from spin up to spin down through thermal activation (kT). Below the blocking temperature, these classical magnetization relaxation pathways are blocked, which leads to the observance of a hysteresis loop. At very low temperatures only quantum tunneling provides an efficient

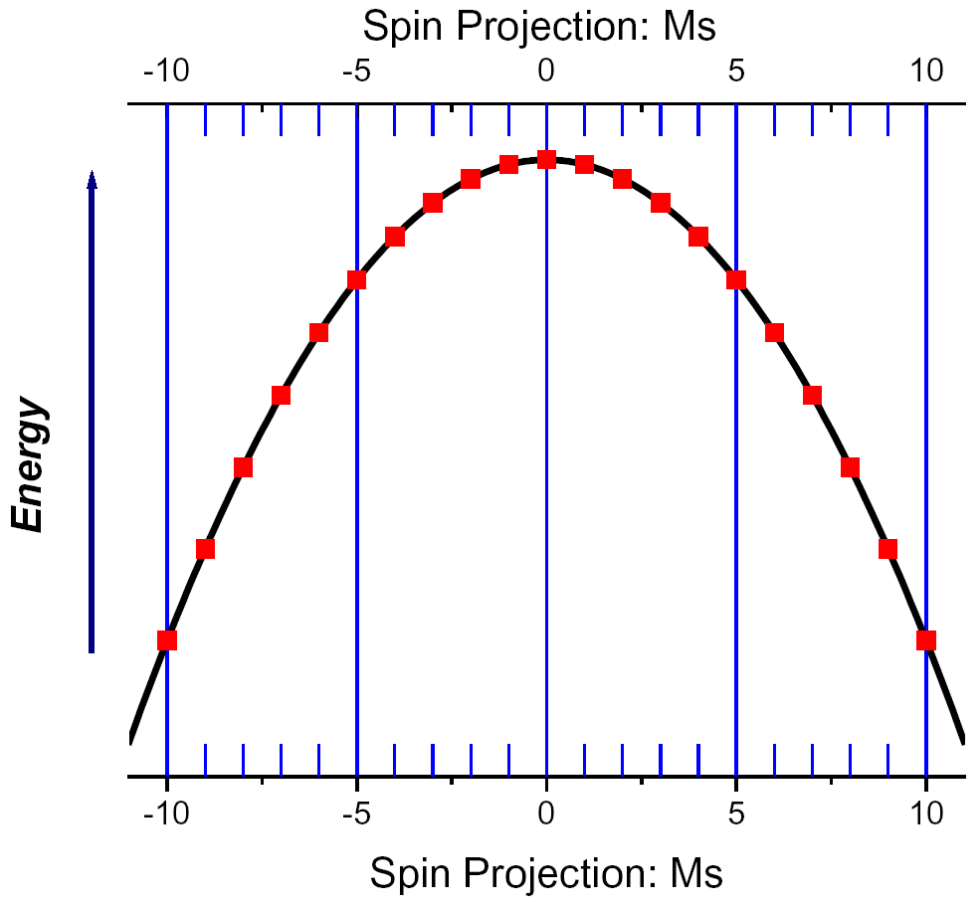

Figure 1. Schematic representation of the potential energy barrier of an S = 10 molecule, split by negative zero-field splitting, i.e. D < 0, in the absence of an applied magnetic field.

pathway for magnetization relaxation. Tunneling can occur when spin up and spin down states are in resonance, that is, the states have the same energy. An applied field can also induce tunneling resonances. When a field is applied, M_s states that are parallel to the applied field decrease in energy while M_s states that are antiparallel to the applied field increase in energy. M_s states can be brought into resonance and field induced tunneling can occur as illustrated in Figure 2. For Mn_{12}-OAc which has S_4 molecular symmetry in the crystal, tunneling resonances induced by an applied field follow the spin Hamiltonian[24]:

$$\hat{H} = \hat{H}_A + \hat{H}_Z + \hat{H}_T \tag{1.1}$$

where the first term accounts for axial zfs, which are given as

$$\hat{H}_A = D[\hat{S}_z^2 - S(S+1)/3] \tag{1.2}$$

the second term, $\hat{H}_Z$, is the Zeeman term which is given by

$$\hat{H}_z = g u_B \hat{H}_z \hat{S}_z \tag{1.3}$$

tunneling between $\pm M_s$ states through an energy barrier requires transverse terms, $\hat{H}_T$, to mix wavefunctions. Some of the terms for a molecule with S_4 symmetry are given by:

$$\hat{H}_T = g\mu_B \hat{H}_x \bullet \hat{S}_x - E(\hat{S}_x^2 - \hat{S}_y^2) - B_4^4 O_4^4 \tag{1.4}$$

where $\hat{H}_x$ is the transverse magnetic field, $(\hat{S}_x^2 - \hat{S}_y^2)$ is the rhombic zfs operator, and O_4^4 is the quartic zero-field operator.

The plot of magnetization hysteresis for a single crystal of Mn_{12}-OAC aligned with the magnetic field along the molecular easy axis is shown in Figure 3.[9] In the

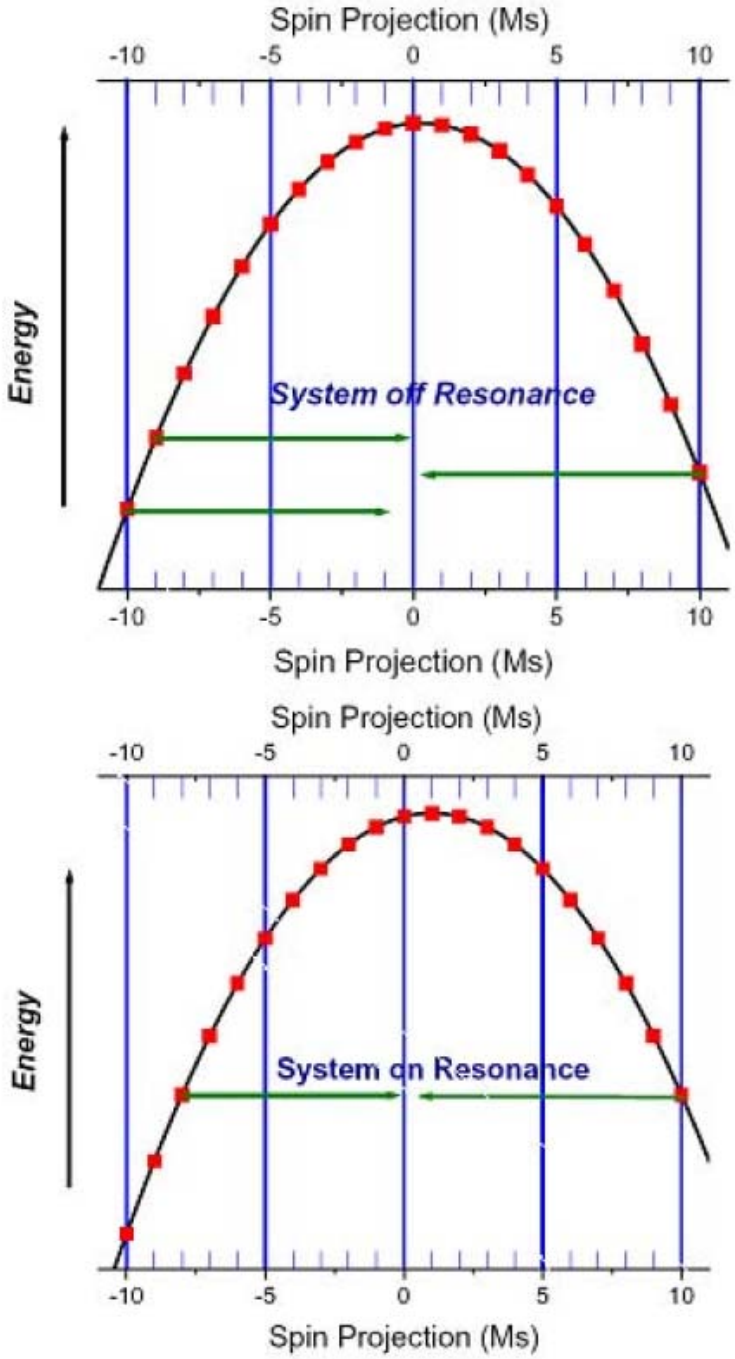

Figure 2. Schematic representations of the potential energy barrier of an S = 10 molecule in an applied field where a difference in energy of M_s states prevents tunneling (top) and where tunneling resonances are allowed due to alignment of M_s states (bottom).

magnetization hysteresis experiment, an applied field is increased in one direction at a rate of 0.004 T/s until the magnetization reaches saturation where the magnetization no longer increases with increasing field strength. The field is then decreased at the same rate to zero, instead of returning to zero the magnetization goes to a remnant magnetization. A field applied in the opposite direction, called the coercive field, then returns the magnetization to zero. The process is repeated in the opposite direction giving rise to a hysteresis loop. Tunneling events are represented by the vertical steps in the hysteresis plot where the tunneling transition induces a rapid change in magnetization. It is important to note from the plot that tunneling events, which should be dictated by the S_4 molecular symmetry in the crystal, and therefore only occur at resonances of $|\Delta m_s| = 2n$, where n is an integer number, occur at all resonances. The symmetry forbidden tunneling resonances can be caused by a distribution of microenvironments within the crystal due solvent loss, structural disorder, or crystalline defects which lowers the molecular symmetry enabling an applied field to induce tunneling transitions. This illustrates the need for systems with no disorder, no solvent molecules, high crystal site symmetry, and high crystal quality.

1.3 AC Susceptibility

In an ac susceptibility measurement, an alternating current of a few Oersted is applied to a polycrystalline sample in the absence of an applied dc field.[25] The dynamics of magnetization are investigated by changing the frequency of the ac field. The time dependent behavior of the magnetization can be described by the following equation[26]:

$$M_{AC} = M_0 \cos\theta \cos(\omega t) + M_0 \sin\theta \sin(\omega t) = \chi' H_0 \cos(\omega t) + \chi'' H_0 \sin(\omega t) \quad (1.5)$$

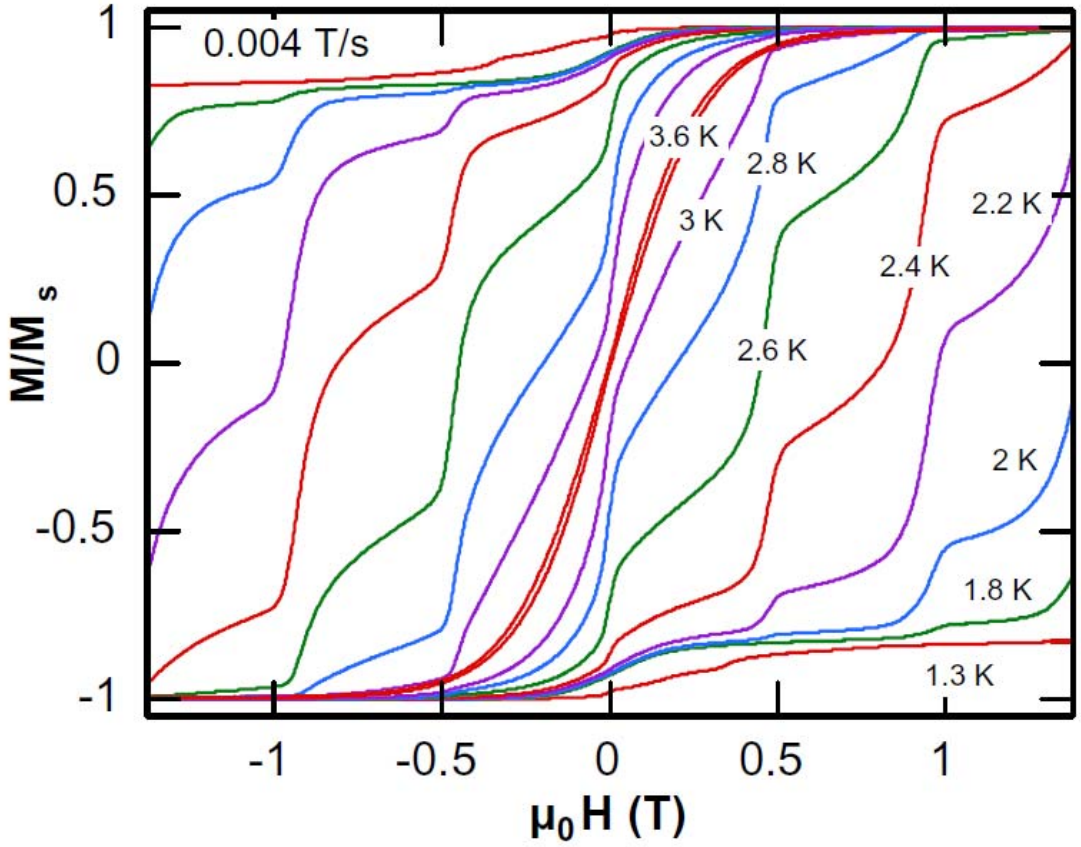

Figure 3. Magnetization versus magnetic field in Mn_{12}-OAc at a sweep rate of 0.004 T/s in a temperature range of 1.3-3.6 K. Vertical steps indicate QTM resonances.

where χ' is the in-phase component and χ" is the out-of-phase component. An out-of-phase signal in the ac response occurs because the relaxation time of the SMM is slower than the rate of the oscillating field. The magnetic moment of the SMM cannot stay in phase with the field, giving rise to a peak in the out-of-phase response. With increasing frequency, the peak positions shift to higher temperatures due to increasing relaxation rates. To determine if more than one relaxation process is occurring in an ac susceptibility experiment, the ac response at each frequency is fit to either Gaussian or Lorentzian behavior. A fit to a single Gaussian indicates that only one relaxation process is present. A Lorentzian is a distribution of Gaussians, which suggests multiple relaxation pathways are present. The effective kinetic energy barrier to magnetization relaxation (U_{eff}) can be measured by applying the Arrhenius equation to the ac susceptibility data:

$$\ln(1/\tau) = \ln(1/\tau_o) - U_{eff}/kT \qquad (1.6)$$

where k is the Boltzmann constant, T is the absolute temperature, τ is the relaxation time, and τ_0 is the pre-exponential factor. An Arrhenius plot is constructed in which the natural log of the reciprocal of the oscillating frequency is plotted against the inverse of the temperature at which a peak maximum occurs for each frequency. U_{eff} is obtained by calculating the slope of the Arrhenius plot.

1.4 DC Susceptibility

The dc susceptibility measurement is made on a powdered sample at a constant applied dc field but variable temperature, in a temperature range of 1.8-300 K. The temperature dependent data can be used to determine the nature of exchange coupling between metal centers. Coupling between metal centers can be described by the Heisenberg-Dirac-Van Vleck Spin Hamiltonian[26:]

$$\hat{H} = \sum_{i>j}^{n} -J_{ij} S_i S_j \qquad (1.7)$$

where S_i and S_j represent the spins of neighboring metal centers that are experiencing a magnetic exchange interaction and J is the isotropic exchange coupling constant. J has a sign which is dependent upon the nature of the coupling between metal centers. If J is positive, the spins are aligned in the same direction and there is ferromagnetic coupling. If J is negative, the spins align in opposite directions and antiferromagnetic coupling occurs.

The J value can be determined from variable-temperature magnetic susceptibility data. Depending on the nuclearity and symmetry of a molecule the Kambe vector model[27] can be used to fit magnetic susceptibility data. The Kambe vector model can also be used to determine the eigenenergies of the spin states of a complex. The energy of each spin state (S_T) is determined by an operator replacement method. The energies are substituted into the Van Vleck equation which relates the spin states and magnetic susceptibility[26]:

$$\chi_M = \left(\frac{Ng^2\mu_B^2}{3kT} \right) \frac{\sum [S_T(S_T+1)(2S_T+1)e^{\frac{-E(S_T)}{k_B T}}}{\sum (2S_T+1)e^{\frac{-E(S_T)}{k_B T}}} \qquad (1.8)$$

where N is Avogadro's number, g is the Lande factor, μ_B is the Bohr magneton, k is the Boltzmann constant, and T is the absolute temperature.

1.5 Variable Field Magnetic Susceptibility (Reduced Magnetization)

The magnetic anisotropy of an SMM, which is represented by the zfs term D, can be determined by analyzing the field dependence of the magnetization at very low

temperatures. In the reduced magnetization experiment, high magnetic fields of 1-5 T are applied to a polycrystalline sample in a temperature range of 1.8-4.0 K. A plot of reduced magnetization ($M/N\mu_B$) versus field divided by temperature (H/T) is obtained, where M is the magnetization, N is Avogadro's number, μ_B is the Bohr magneton, and H/T is the magnetic field divided by the absolute temperature. The temperature must be kept low in order ensure that only the ground state is populated and that zero-field splitting is larger than kT so that the moments align with the applied field. In a molecule with no zero-field splitting, the iso-fields will be superimposed and follow a Brillouin function where the reduced magnetization saturates at a value of g•S in high magnetic fields. Nonsuperimposable isofields are indicative of a non-zero zfs term. The use of polycrystalline samples results in a random orientation of crystallites. A powder average must be used in which magnetization is integrated over all possible orientations of the external field. Magnetization can be calculated by diagonalization of the spin Hamiltonian[26]:

$$\hat{H} = g\mu_B \mathrm{H}\cdot S + D[S_z^2 - S(S+1)/3] + E[S_x^2 - S_y^2] \qquad (1.9)$$

where the second term is the second order zfs term D, and the third term E, is the second order rhombic term. The eigenvalues are substituted into the Van Vleck equation[25]:

$$M = \frac{\sum_{i=-S}^{S} (\partial E_i / \partial H)\exp(-E_i / kT)}{\sum_{i=-S}^{S} \exp(-E_i / kT)} \qquad (1.10)$$

from the spin Hamiltonian it can be noted that, potentially, all three terms (D, E, and S) can be determined by a least-squares fit of data.

1.6 Oxo-Centered Mn_3 Triangles and Related Compounds

Since most of the complexes reported in this work are built up from oxo-centered Mn_3^{III} triangles, it is important to give an overview of this large class of compounds. There are many examples of oxo-centered triangles in a variety of transition metals, although the most common metals are Fe, Mn, and Cr.[28-31] Most complexes have coordinated carboxylate and solvate ligands and are of the general formula $[M_3O(O_2CR)_6L_3]^+$ where R = Me, Et, Ph, etc. and L = pyr, H_2O, MeOH, etc.[31, 32] Magnetic exchange is mediated through the carboxylate ligands and a planar μ_3-oxo ligand. The complexes exhibit spin frustrated antiferromagnetic behavior with small spin ground states (S = 0 or 1) which precluds SMM behavior.

It was only recently that a ferromagnetic example of an oxo-centered manganese triangle was reported. The first example with an S = 6 ground state, has the formula $[Mn_3O(O_2CMe)_3(mpko)_3](ClO_4) \bullet 3CH_2Cl_2$, where mpko = 2-prydyl ketone oxime.[33, 34] The complex differs from other Mn_3 triangles in that it possesses a significantly out-of-plane O^{2-} of 0.30 Å and three of the carboxylates and three solvate molecules had been replaced by three N,N,O-oximate ligands.[34] It was suggested that the strength of the antiferromagnetic exchange through the O^{2-} increases with increasing overlap of the p-π orbitals of the central oxo and the d-π orbitals of the metal centers. The ferromagnetic behavior results from the out-of-plane O^{2-} breaking this planarity.[34]

A related series of triangles of the formula $[Mn_3O(O_2CR)_3(salox)_3]$ where R = Me, Ph; salox = salicylaldoxime, were reported as part of a DFT study by Cano et al.[35] These complexes also possess an out-of-plane O^{2-} approximately 0.34 Å above the Mn_3 plane, yet exchange within the triangles were found to be largely antiferromagnetic.

From this result it was concluded that the out-of-plane O^{2-} was not the dominant interaction governing ferromagnetic exchange in $[Mn_3O(O_2CMe)_3(mpko)_3]^+$ as once thought. These complexes differed from the ferromagnetic $[Mn_3O(O_2CMe)_3(mpko)_3]^+$ complex in that they possessed a planar oximate moiety. The DFT study suggested that the alignment of the Jahn-Teller axes, out-of-plane μ-oxo, and the distortion of the Mn-N-O-Mn oximate linkage all play a part in determining the net magnetic properties of the triangles. However, magnetic behavior could not be attributed to a single determining factor.

Milios et al.[36-38] systematically induced structural distortions in a family of Mn_6 SMMs, which represented the first attempt to build up oxime-stabilized Mn_3^{III} triangles into larger topologies. The first Mn_6 complexes have the formula $[Mn_6O_2(R\text{-salox})_6(O_2CPh)_2(EtOH)_4]$ where R is H or Et, and consisted of two offset oxo-centered Mn_3^{III} triangles.[36, 37] As expected, magnetic exchange within the complex with the most planar Mn-N-O-Mn moiety was largely antiferromagnetic. The H_2-salox analogue has an average Mn-N-O-Mn torsion angle of $\theta = 17.5^o$. As illustrated in Figures 4 and 5, the oximate torsion angle is defined as the angle between two planes, one containing one metal and the N and O atom of the oximate, and the other plane defined by the second metal and the N and O atoms. The small torsion angles results in a complex consisting of two antiferromagnetically coupled Mn_3^{III} triangles with a S = 4 ground state. Magnetic exchange becomes more ferromagnetic as the size of the alkyl group, and the resulting distortion of the Mn-N-O-Mn moiety increases. Torsion angles in the Et-salox analogue increases to an average of $\theta = 39.1^o$ which results in a ferromagnetic complex with a S = 12 ground state. The large axial anisotropy coupled with a

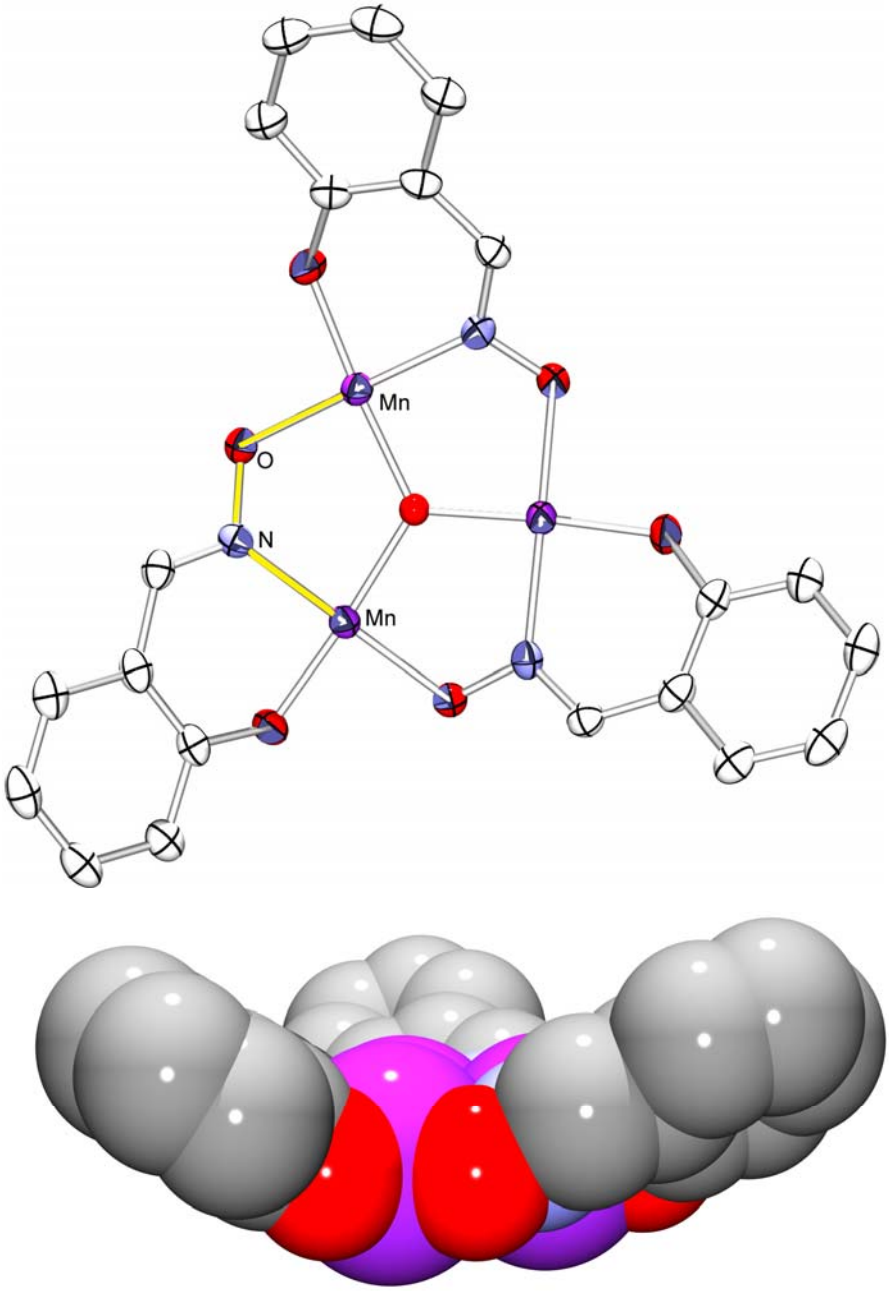

Figure 4. A salicylaldoxime stabilized Mn_3^{III} triangle with the bonds of the Mn-N-O-Mn moiety highlighted in yellow (top). Space filling model of an oxime stabilized Mn_3^{III} triangle with a torsion angle of $\theta = 33.5^{o}$ (bottom).

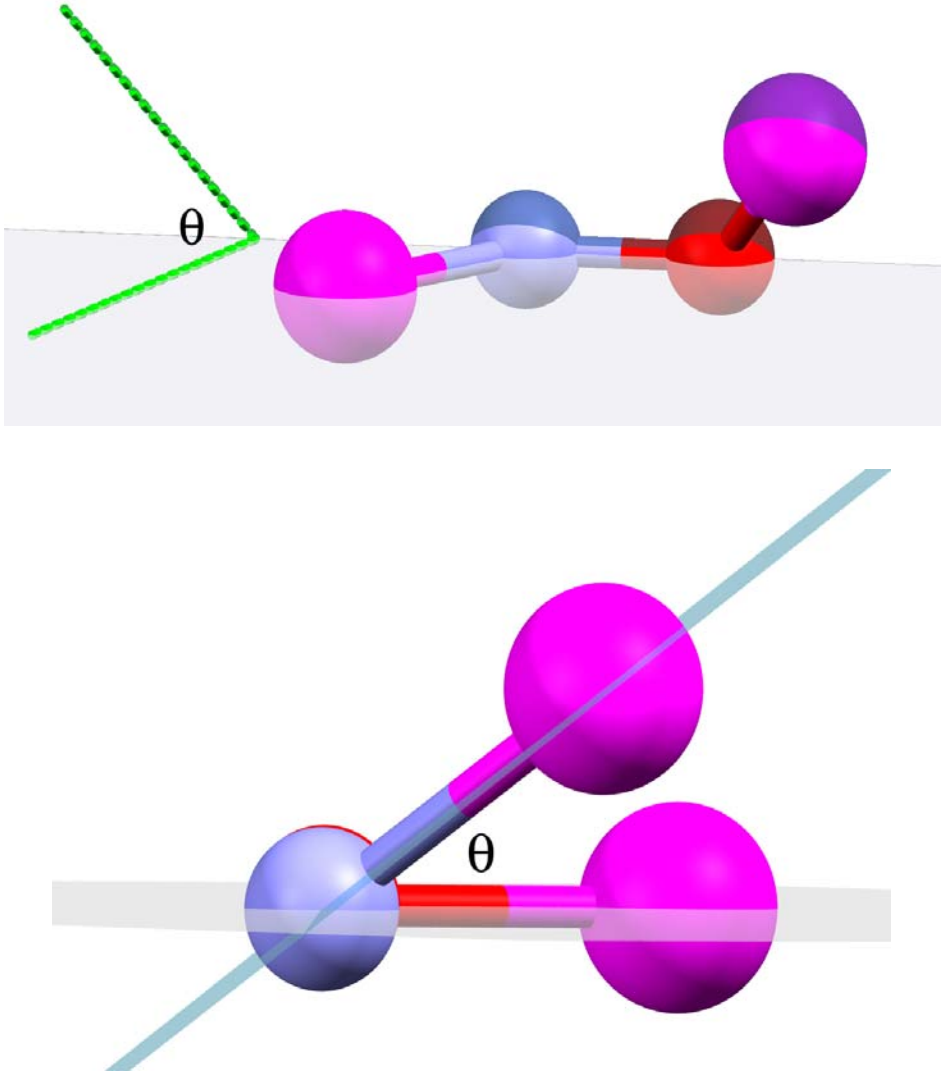

Figure 5. Representation of the Mn-N-O-Mn moiety where purple spheres represent manganese, blue spheres represent nitrogen, and red spheres represent oxygen. The torsion angle, θ, is formed by the intersection of the two Mn-N-O planes (top). View down the N-O bond (bottom).

S = 12 ground state resulted in the largest effective barrier reported in a SMM of U_{eff} = 86.4 K.[37] Further magneto-structural correlations in the family of Mn_6 SMMs suggested a turnover angle from antiferromagnetic to ferromagnetic exchange in the Mn-N-O-Mn torsion angle of ~32°. This trend is consistent in a variety of complexes with many types of axially coordinated ligands (carboxylates, alcohols, azides).[38, 39]

A trigonal bipyramidal $Mn_2^{II}Mn_3^{III}$ complex of the formula $[NEt_4]_3[Mn_5(salox)_3O(N_3)_6Cl_2]$ where salox is salicylaldoxime, was reported by Yang et al.[40] The complex consists of a central μ_3-O^{2-} centered Mn_3^{III} triangle capped above and below the plane of the triangle by μ_2–η^1: η^1 azide bridged Mn^{II} ions. Azide is known to mediate ferromagnetic exchange at a wide range of bonding angles between a variety of metals.[41, 42] Exchange within the complex was ferromagnetic resulting in a S = 11 spin ground state. However, fits of dc magnetization revealed weak ferromagnetic exchange between the Mn^{II} and Mn^{III} ions with $J(Mn^{III}\text{-}Mn^{II})$ = 0.22 cm^{-1}. Single crystal magnetization versus field hysteresis measurements revealed significant axial anisotropy with $|D|/g$ = 0.51 cm^{-1}. Combined with an S = 11 ground state, these values yield a theoretical barrier of DS_z^2 = 176 K. The presence of a first excited state 3.2 cm^{-1} above the ground state reduced the effective barrier to U_{eff} = 40.3 K. It is important to note that this complex crystallizes in the hexagonal R3c space group with one molecular orientation and no solvent molecule. Both of these properties are important in orientated single-crystal hysteresis and high-frequency electron paramagnetic resonance (HFEPR) as the former implies that the molecular easy-axis is aligned with the easy-axis of the crystal and the latter leads to a reduction in micro-environments which results in sharper HFEPR signals. This complex provides an ideal starting point for inducing structural

distortions in order to strengthen exchange interactions possibly leading to slower relaxation rates.

A series of oxime-stabilized Zn_2Mn_3 molecules that were structurally identical to the $Mn_2^{II}Mn_3^{III}$ complex were reported by Feng et al.[43, 44] Structural distortions were induced by varying the oximate ligand and by changing the counter-cation or coordinated terminal halides. Through these structural distortions, the spin ground state of the complexes was switched from S = 1 to S = 6 complexes with variable ferromagnetic exchange.[43] Further studies utilizing orientated single crystal magnetization hysteresis were conducted on two analogues, $[NEt_4]_3[Zn_2Mn_3(salox)_3O(N_3)_6X_2]$, X = Cl or Br.[45] These analogues crystallized in the hexagonal space group R3c in one orientation, possessed no solvent molecules, and were well isolated, with the closest Mn•••Mn contact larger than 10 Å. Magnetization hysteresis experiments performed on these complexes revealed for the first time, the observance of symmetry behaved tunneling resonances. A derivative plot of magnetization hysteresis loop is shown in Figure 6. In Figure 6, peaks corresponding to tunneling resonances for k = 0, 1, 2, and 3 are observed at intervals of approximately 0.85 T. A C_3 symmetric molecule should exhibit a series of QTM peaks associated with tunnel resonances at intervals of $\Delta m_s = 3n$. Two symmetry allowed tunneling resonances correspond to k = 0 and k = 3.[44] Initially it was thought that the k = 1 resonance was a symmetry forbidden tunneling resonance. However, the k = 1 resonance appears above 1.5 K; this suggests that an excited state is populated before a symmetry allowed QTM transition occurs.

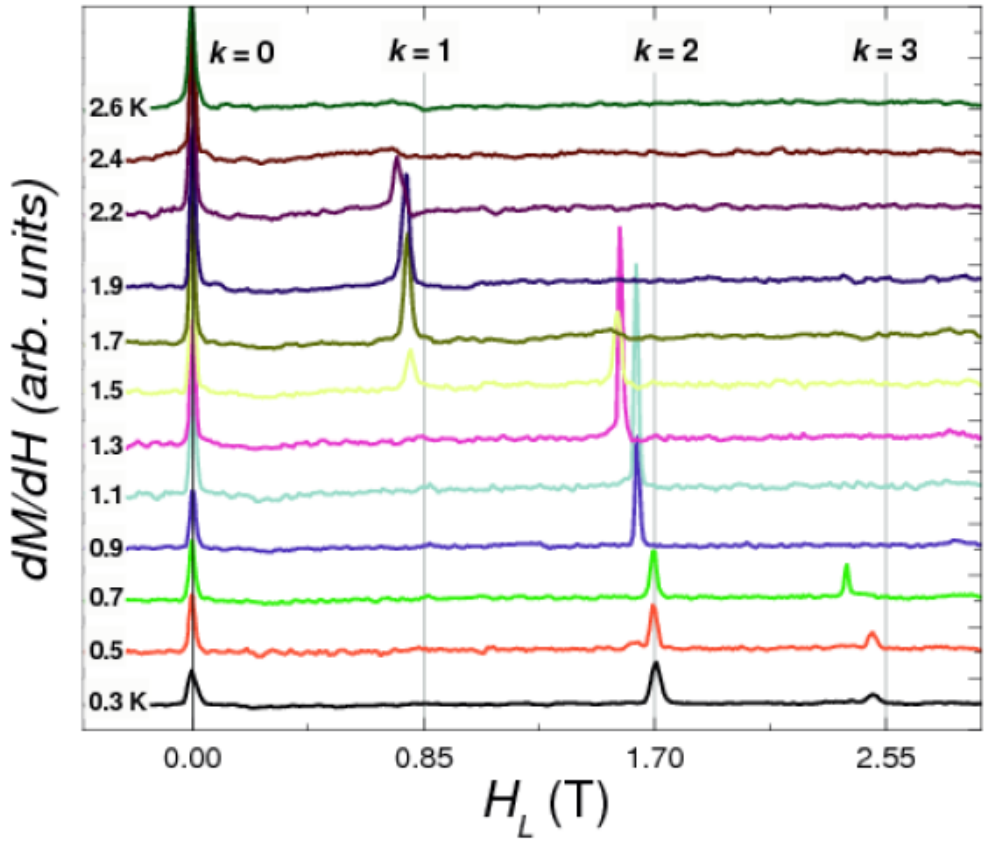

Figure 6. Derivative plot of orientated single crystal magnetization hysteresis data for $[NEt_4]_3[Zn_2Mn_3(salox)_3O(N_3)_6Cl_2]$ in a temperature range of 0.3-2.6 K at a sweep rate of 1 T/min. The magnetic field was aligned along the easy axis.[44]

These studies illustrate the versatility of oxime stabilized Mn_3 triangles. These triangles serve as a flexible platform of study for both synthetic chemists and physicists. By carefully tuning their environment and their magnetic properties, they can provide insight into the physics of SMM behavior. They can also serve as building blocks for larger topologies where their potential for axial anisotropy and ferromagnetic exchange can result in SMMs with larger barriers to reversal of magnetization. In this thesis I will describe my efforts to characterize new polynuclear Mn complexes incorporating as many as four $Mn_3^{III}O$ units.

1.7 Magnetic Metal-Organic Frameworks (MOFs)

The industrial applications of porous materials are multifold: from catalytic applications such as the use of zeolites in cracking petroleum to adsorption of hydrogen or carbon dioxide gas. Metal-organic frameworks (MOFs) are one, two, or three dimensional materials composed of metal ions coordinated by bridging chelating ligands.[46] These frameworks can be highly porous. Typically, the pores are filled with solvate molecules which can be removed by heating and/or applying a sufficiently strong vacuum. The surface area of these complexes tends to be very high; Yaghi's MOF-5 has one of the largest reported surface areas of 3,000 m^2/g.[47] Void spaces in these complexes can be incredibly high as well, with some examples in excess of 70% of the total crystal volume. Applications for these porous materials have principally concerned gas storage (N_2, H_2, CH_4, etc) but other applications include gas separation, catalysis, and sensing.[48-51]

Magnetism is another property that can be exhibited by MOFs.[52] A magnetic MOF could function as a magnetic porous membrane. One possible application of a

magnetic MOF would be the separation of paramagnetic and diamagnetic particles. Magnetic zeolites have been in use for some time and have been used to remove lead ions from water.[53] The use of transition metals with unpaired spins is not necessarily enough to impart magnetic behavior in a MOF. Magnetic ordering is required, otherwise a system of uncorrelated spins can result. Bridging ligands commonly used in MOF synthesis can mediate magnetic exchange interactions between metal centers if the bridging distance is short. MOFs constructed from short bridging ligands such as cyanide or azide can potentially impart stronger magnetic exchange interactions than the larger aryl dicarboxylates used in the MOFs with the largest pores. If magnetic exchange is to be maximized the distances between metal centers needs to be short. However, if there is to be any sizable void space there needs to be some distance between the metal centers whose coordination geometry gives rise to the structural framework.

Thus, it is not surprising that only a handful of three dimensional magnetic MOFs have been reported.[52] Imparting SMM behavior in a MOF is even more of a challenge. SMM behavior requires appreciable axial anisotropy in addition to a large spin ground state. MOFs tend to have very high symmetry which would preclude a D term. It would be possible to devise a MOF with SMM behavior if the core building blocks could function as a SMM. The building blocks could be built up through bulky ligands or by coordination to diamagnetic metals such as Zn^{+2} that would isolate each SMM unit.

1.7 Incorporation of SMMs into Devices

Since one of the goals of SMM research is to incorporate SMMs into nanoscale devices it is important to first understand the effects resulting from attaching a SMM to a system with an electronic band structure. A few approaches to this problem have

included: (1) attaching SMMs to gold surfaces,[54] (2) assembling chains of SMMs in an arrangement of alternating Au/SMM building blocks,[54] and (3) placing SMMs between break junctions.[56] Placing SMMs on surfaces can be problematic as it leads to a random orientation of SMMs on a surface which can lead to a distribution of microenvironments, resulting in quantum decoherence.[20] Ideally the system would be crystalline, as that would provide an ordered environment which would minimize microenvironments.

Cocrystallization of an SMM with a conductor or superconductor is another approach to coupling a conductor with an SMM. This approach is plagued with the difficulty of establishing a strong interaction between conducing electrons in the bands of the conductors and the unpaired electrons of the magnetic metal centers. Coronado et al.[57] co-crystallized magnetic $[Mn^{II}Cr^{III}(C_2O_4)_3]^-$ ions with bis(ethylenedithio)tetrathiofulvalene (BEDT-TTF), a potential superconductor. Although $[Mn^{II}Cr^{III}(C_2O_4)_3]^-$ is not an SMM, this example illustrates the difficulty of invoking a strong interaction between these types of particles. Two distinct layers emerged and the interaction between magnetic and conductor layers was found to be very weak. The magnetic properties of the $Mn^{II}Cr^{III}$ ions were unchanged; essentially the material was behaving as two independent layers. No long range interaction between the metal centers and the conductor electrons was observed (i.e. no Kondo effect).

Work in this thesis explores the synthesis of a fullerene functionalized with salicylaldehyde. C_{60} is well known for its conducting and superconducting behavior.[58] It is hoped that the proximity of the fullerene to the SMM will provoke a strong interaction between the two. Future work will entail the formation of a oxime through a condensation reaction and the subsequent synthesis of a SMM with this ligand.

1.8 Outline of Thesis

This thesis concerns the assembly of oxime-stabilized oxo-centered Mn^{III} triangles into larger topologies, some of which possess possible multi-functionality.

Chapter 2 presents magneto-structural correlations in a family of Mn_5 "single-deckers" SMMs of the formula $[NEt_4]_3[Mn_2^{II}Mn_3^{III}O(R\text{-salox})_3(N_3)_6X_2]$ where R = H, Me, or Et; and X = Cl or Br. The work entails their synthesis and characterization by X-ray diffraction and bulk magnetic susceptibility and the role variation in certain structural geometries plays in magnetic exchange within each molecule.

In Chapter 3, structural distortions are induced in two Mn_8 "double-decker" SMMs of the formula $[NX_4]_2[Mn_2^{II}Mn_6^{III}O_2(salox)_6(N_3)_6(MeOH)_2Cl_2] \bullet 2sol$, where X = n-Pr or n-Bu; Sol = $CHCl_3$ or MeOH, by changing the cocrystallizing counter-ions. A one dimensional chain is constructed from the core of this complex through end-on bridging azides to form a complex of the formula $[NEt_4]_2[Mn_2^{II}Mn_6^{III}O_2(salox)_6(N_3)_8(MeOH)_3]_\infty \bullet MeOH$. The characterization of these complexes by X-ray diffraction and magnetic susceptibility measurements is discussed.

Chapter 4 details two very distinct molecules assembled from oxo-centered Mn_3^{III} triangles. The first, of the formula $[Mn_{12}^{III}O_4(salox)_{12}(N_3)_4(MeOH)_8(H_2O)_2] \bullet 4MeOH \bullet 2H_2O$ consists of a $[Mn^{III}_6(\mu_3\text{-}O^{2-})_2(\mu_3\text{-}OR)_2]^{+12}$ core capped with two Mn_3^{III} triangles by bridging azides. Its characterization by X-ray diffraction and bulk susceptibility will be presented. The second complex, of the formula $[Mn_{13}Na_9O_4(EtO\text{-}salox)_{12}(N_3)_6(MeOH)_6(H_2O)_{10}Cl_3]_\infty$ where EtO-salox is 3-ethoxysalicylaldoxime, forms a three dimensional

structure with substantial porosity. Work towards its characterization as a MOF will be discussed in addition to its structural and magnetic properties.

Chapter 5 will cover the synthesis and characterization of a salicylaldehyde functionalized fullerene. The chapter will also discuss possible applications of this ligand.

References

1. Thiaville, A; Miltat, J., Magnetism: small is beautiful. *Science* **1999**, 284, (5289), 938-940.

2. Wernsdorfer, W., Classical and quantum magnetization reversal studied in nanometer-sized particles and clusters. *Advanced Chemical Physics* **2001**, 118, 88-190.

3. Kahn, O; Pei, Y; Verdaguer, M; Renard, J. P.; Sletten, J., Magnetic Orderin of $Mn^{II}Cu^{II}$ Bimetallic Chains: Design of a Molecular-Based Ferromagnet *Journal of the American Chemical Society* **1988**, 110, 3, 782-789.

4. Ferlay, S., Mallah, T.; Ouahes, R.; Veillet, P.; Verdaguer, M. A room-temperature organometallic magnet based on Prussian blue. *Nature* **1995**, 378, 701-703

5. Lis, T., Preparation, structure, and magnetic-properties of a dodecanenuclear mixed-valence manganese carboxylate. *Acta Crystallographica Section B-Structural Science* **1980,** 36, (SEP), 2042-2046.

6. Caneschi, A.; Gatteschi, D.; Sessoli, R.; Barra, A. L.; Brunel, L. C.; Guillot, M., Alternating-current susceptibiliy, high-field magnetization, and millimeter band EPR evidence for a ground S=10 state in $[Mn_{12}O_{12}(CH_3COO)_{16}(H_2O)_4]\cdot 2CH_3COOH\cdot 4H_2O$. *Journal of the American Chemical Society* **1991,** 113, (15), 5873-5874.

7. Sessoli, R.; Tsai, H. L.; Schake, A. R.; Wang, S. Y.; Vincent, J. B.; Folting, K.; Gatteschi, D.; Christou, G.; Hendrickson, D. N., High-Spin Molecules - [Mn12o12(O2cr)16(H2o)4]. *Journal of the American Chemical Society* **1993,** 115, (5), 1804-1816.

8. Sessoli, R.; Gatteschi, D.; Caneschi, A.; Novak, M. A., Magnetic Bistability in a Metal-Ion Cluster. *Nature* **1993,** 365, (6442), 141-143.

9. Miyasaka, M.; Clèrac, R.; Wernsdorfer, W.; Lecren, L.; Bonhomme, C.; Sugiura, K.; A. A Dimeric Manganese(III) Tetradentate Schiff Base Complex as a Single-Molecule Magnet, *Angewandte Chemie International Edition,* **2004**, *43*, 2801.

10. Tasiopoulos, T. J.; Vinslava, A.; Wernsdorfer, W.; Abboud, K. A.; Christou, G. Giant single-molecule magnets: A {Mn-84} torus and its supramolecular nanotubes, *Angewandte Chemie International Edition.* **2004**, *43*, 2117.

11. Mishra, A.; Wernsdorfer, W.; Abboud, K. A.; Christou, G. Initial observation of magnetization hysteresis and quantum tunneling in mixed manganese - Lanthanide single-molecule magnets, *Journal of the American Chemical Society,* **2004**, *126*, 15648.

12. Soler, M.; Rumberger, E.; Folting, K.; Hendrickson, D. N.; Christou, G., Synthesis, characterization and magnetic properties of [Mn30O24(OH)(8)(O2CCH2C(CH3)(3))(32)(H2O)(2)(CH3NO2)(4)]: the largest manganese carboxylate cluster, *Polyhedron* **2001**, *20*, 1365-1369.

13. Yang, E. C.; Hendrickson, D. N.; Wernsdorfer, W.; Nakano, M.; Zakharov, L. N.; Sommer, R. D.; Rheingold, A. L.; Ledezma-Gairaud, M.; Christou, G. *Journal of Applied Physics,* **2002**, *91*, 7382.

14. del Barco, E.; Kent, A. D.; Hill, S.; North, J. M.; Dalal, N. S.; Rumberger, E. M.; Hendrickson, D. N.; Chakov, N.; Christou, G., Magnetic quantum tunneling in the single-molecule magnet Mn-12-acetate. *Journal of Low Temperature Physics* **2005,** 140, (1-2), 119-174.

15. del Barco, E.; Kent, A. D.; Rumberger, E. M.; Hendrickson, D. N.; Christou, G., Symmetry of magnetic quantum tunneling in single molecule magnet Mn-12-acetate. *Physical Review Letters* **2003,** 91, (4).

16. Gonzalez, G.; Leuenberger, M. N., Berry-phase blockade in single-molecule magnets. *Physical Review Letters* **2007,** 98, (25).

17. Leuenberger, M. N.; Mucciolo, E. R., Berry-phase oscillations of the kondo effect in single-molecule magnets. *Physical Review Letters* **2006,** 97, (12).

18. Wegewijs, M. R.; Romeike, C.; Schoeller, H.; Hofstetter, W., Magneto-transport through single-molecule magnets: Kondo-peaks, zero-bias dips, molecular symmetry and Berry's phase. *New Journal of Physics* **2007,** 9.

19. Chudnovsky, E. M., Quantum hysteresis in molecular magnets. *Science* **1996,** 274, (5289), 938-939.

20. Stamp, P. C. e., Gaita-Arin, G. Spin-based quantum computers made by chemistry; hows and whys. *Journal of Materials Chemistry*, **2009**, 19, 1718-1730.

21. Sessoli, R.; Tsai, H. L.; Schake, A. R.; Wang, S. Y.; Vincent, J. B.; Folting, K.; Gatteschi, D.; Christou, G.; Hendrickson, D. N., High-Spin Molecules -

[Mn12o12(O2cr)16(H2o)4]. *Journal of the American Chemical Society* **1993,** 115, (5), 1804-1816.

22. McInnes,E L,; Pidcock, L; Oganesyan, V. S.; Cheesman,M. R.,; Powell, A. K.; Thomson, A. J. Optical Detection of Spin Polarization in Single-Molecule Magnets [Mn12O12(O2CR)16(H2O)4] *Journal of the American Chemical Society* **2002** 124 (31), 9219-9228

23. Christou, G.; Gatteschi, D.; Hendrickson, D. N.; Sessoli, R., Single-molecule magnets. *Mrs Bulletin* **2000,** 25, (11), 66-71.

24. Caneschi, A.; Gatteschi, D.; Sangregorio, C.; Sessoli, R.; Sorace, L.; Cornai, A.; Novak, M. A.; Paulsen, C.; Wernsdorfer, W. The Molecular Approach to Nanoscale Magnetism, *The Journal of Magnetism and Magnetic Materials*, **1999**, 200, 1-3, 182-201.

25. Dante Gatteschi, R. S., and Jacques Villain, ***Molecular Nanomagnets***. Oxford University Press: New York, **2005**.

26. Kahn, O., Molecular Magnetism. ed.; VcH, Weinheim: **1993**; 'Vol.' p.

27. Kambe, K., On the paramagnetic susceptibilities of some polynuclear complex salts, *The Journal of the Physical Society of Japan*, **1950**, 5, 48-51.

28. Bauman, J. A.; Salmon, D. J.; Wilson, S. T.; Meyer, T. J.; Hatfield, W. E. Electronic Structure and Redox Properties of Clusters [Ru3O(CH3CO2)6L3]n+. *Inorganic Chemistry* **1978** 3342-3344

29. Vincent, J. B.; Chang, H. R.; Folting, K.; Huffman, J. C.; Christou, G.; Hendrickson, D. N. Preparation and Physical Properties of Trinuclear Oxo-Centered Manganese Complexes of the General Formulation [Mn3O(O2CR)6L3]0,+ (R = Me or Ph, L = a Neutral Donor Group) and the Crystal-Structures of [Mn3O(O2CME)6(Pyr)3](Pyr) and [Mn3O(O2CPH)6(Pyr)2(H2O)]0.5MeCN, *Journal of the American Chemical Society* **1987** 109 19 5703-5711.

30. R. D. Cannon and R. P. White, Chemical and Physical-Properties of Triangular Bridged Metal-Complexes, *Progress in Inorganic Chemistry*, **1988**, 36, 195-298.

31. Castro S. L.; Streib, W. E.; Sun J. S.; Christou G,Structural, spectroscopic, and magnetochemical characterization of the trinuclear vanadium(III) carboxylates [V3O(O(2)CR)(6)L(3)](ClO4) (R=various groups; L=pyridine, 4-picoline, 3,5-lutidine), *Inorganic Chemistry*, **1996**, 35, 15, 4462-4468.

32. Jones, D. H.; Sams, J. R.; and Thompson, R. C. The magnetic behavior of clusters of the type $[M_3O(RCOO)_6]^+$. An isotropic model involving dynamic distortions, *Journal of Chemical Physics*, **1984**, 81 440.

33. Stamatatos, T. C.; Foguet-Albiol, D.; Stoumpos, C. C.; Raptopoulou, C. P.; Terzis, A.; Wernsdorfer, W.; Perlepes, S. P.; Christou, G.; Initial Example of a Triangular Single-Molecule Magnet from Ligand Induced Structural Distortion of a [MnIII3O]7+ Complex, *Journal of the American Chemical Society*, **2005**, 127, 15380-15381.

34. Stamatatos, T. C.; Foguet-Albiol, D.; Lee, S. C.; Stoumpos, C. C.; Raptopoulou, C. P.; Terzis, A.; Wernsdorfer, W.; Hill, S. O.; Perlepes, S. P.; Christou, G. "Switching on" the Properties of Single-Molecule Magnetism in Triangular Manganese(III) Complexes, *Journal of the American Chemical Society*, **2007**, *129*, 9484–9499.

35. Cano, J.; Cauchy, T.; Ruiz, E.; Constantinos, J M; Constantinos, C.; Stoumpos, C.; Stamatatos, C.; Spyros, P. P.; Christou, G.; Brechin, B. K. On the origin of ferromagnetism in oximato-based [Mn3O]7+ triangles. *Dalton* **2008** 234-240.

36. Milios, C. J.; Vinslava, A.; Wood, P. A.; Parsons, S.; Wernsdorfer, W.; Perlepes, S. P.; Christou, G.; and Brechin, E. K., A Single-Molecule Magnet with a "Twist" *Journal of the American Chemical Society*, **2007**, 129, 8-9.

37. Milios, C. J.; Vinslava, A.; Wood, P. A.; Parsons, S.; Wernsdorfer, W.; Perlepes, S. P.; Christou, G.; and Brechin, E. K., A Record Anisotropy Barrier for a Single-Molecule Magnet, *Journal of the American Chemical Society*, **2007**, 129, 10 2754-2755.

38. Milios, C. J.; Piligkos, S.; Brechin, E. K. Ground state spin-switching via targeted structural distorsion: twisted single-molecule magnets from derivatised salicyaldoximes *Dalton* **2008**, 1809-1817.

39. Inglis, R.; Jones, L. F.; Milios, C. J.; Datta, S.; Collins, A.; Parsons, S.; Wernsdorfer, W.; Hill, S.; Perlepes, S. P.; Piligkos, S.; Brechin, E. K. Attempting to understand (and control) the relationship between structure and magnetism in an extended family of Mn6 single-molecule magnets, *Dalton Transactions*, **2009,** 3404-3423.

40. Yang, C. I.; Wernsdorfer, W.; Lee, G. H.; Tsai, H. L. A pentanuclear manganese single-molecule magnet with large anisotropy. *Journal of the American Chemical Society*, **2007**, 129, 455-457.

41. Stamatatos, T. C.; Christou, G. Azide Groups in Higher Oxidation State Manganese Chemistry: From Structural Aesthetics to Single-Molecule Magnets. *Inorganic Chemistry*, **2009**, 48, 8, 3308-3322.

42. Zeng, Y. F.; Hu, X.; Liu, F. C.; Bu, X. H. Azido-mediated systems showing different magnetic behaviors. *Chemical Society Reviews*, **2009**, 38, 469-480.

43. Feng, P.; Changhyun, K.; Henderson, J.; Nakano, M; Hill, S.; del Barco, E.; Hendrickson, D. N.; Single-molecule-magnet behavior and spin changes affected by crystal packing effects. *Inorganic chemistry*, **2008**, 47, 19 8610-8612.

44. Feng, P.; Changhyun, K.; Henderson, J.; Manning, P.; Nakano, M; Hill, S.; del Barco, E.; Hendrickson, D. N.; Nanomodulation of Molecular Nanomagnets. *Inorganic Chemistry*, **2009**, 48, 8480-3492.

45. Henderson, J. J.; Koo, C.; Feng, P. L.; del Barco, E.; Hill, S.; Tupitsyn, I. S.; Stamp, P. C. E.; Hendrickson, D. N. Manifestation of Spin Selection Rules on the Quantum Tunneling of Magnetization of Single Molecule Magnets, *Physical Review Letters*, **2009**, 103, 017202.

46. Rowsell, J. L. C.; Yaghi, O. M., Metal-Organic Frameworks: A New Class of Porous Materials, *Microporous Mesoporous Mater.*, **2004**, *73*, 3-14

47. Yaghi, O'Keeffe, Ockwig, Chae, Eddaoudi, and Kim. Reticular synthesis and the design of new materials. *Nature*. **2003** 423 705.

48. Duren, T.; Sarkisov, L.; Yaghi, O. M.; Snurr R. Q. Design of New Materials for Methane Storage *Langmuir* **2004**, 20, 2683-2689.

49. Rowsell, J. L. C.; Millward, A. R.; Park, K. S.; Yaghi, O. M. Hydrogen Sorption in Functionalized Metal-Organic Frameworks, *J. Am. Chem. Soc.*, **2004**, *126*, 5666-5667.

50. Sudik, A. C.; Ockwig, N. W.; Millward, A. R.; Côté, A. P.; Yaghi, O. M. Design, Synthesis, Structure, and Gas (N_2, Ar, CO_2, CH_4 and H_2) Sorption Properties of Porous Metal-Organic Tetrahedral and Heterocuboidal Polyhedra, *J. Am. Chem. Soc.*, **2005**, *127*, 7110-7118.

51. Achmann, S.; Hagen, G.; Kita, J.; Malkowsky, I. M.; Kiener, C.; Moos, R., Metal-Organic Frameworks for Sensing Applications in the Gas Phase, *Sensors* **2009**, 9, 1574-1589.

52. Kurmoo, Mohamedally, Magnetic metal-organic frameworks, *Chemical Society Reviews*, **2009**, 38, 1353-1379.

53. Nah, W.; Hwand Y. K.; Jeon, C.; Choi, H. B. Removal of Pb ion from water by magnetically modified zeolite. *Minerals Engineering*, **2006**, 19, 1452.

54. Zobbi, L.; Mannini, M.; Pacchioni, M.; Chastanet, G.; Bonacchi, D.; Zanardi, C.; Biagi, R.; Del Pennino, U.; Gatteschi, D.; Cornia, A.; Sessoli, R., Isolated single-molecule magnets on native gold. *Chemical Communications*, **2005**, (12), 1640-1642.

55. Hiraga, H., Miyasaka, H.; Clerac, R.; Fourmigue, M.; Yamashita, M. [MIII(dmit)2]- Coordinated MnIII Salen-Type Dimers (MIII = NiIII, AuIII; dmit2- = 1,3-dithiol-2-thione-4,5-dithiolate): Design of Single-Component Conducting Single-Molecule Magnet-Based Materials, *Inorganic Chemistry* **2009**, 48, 2887-2898.

56. Ni, C.; Shah, S; Hendrickson, D. H.; Bandaru, P. R., Enhanced differential conductance through light induced current switching in Mn-12 acetate molecular junctions, *Applied Physics Letters*, **2006**, 89, 21, 212104

57. Coronado, E.; Galan-Mascaros, J. R.; Gomez-Garcia, C. J.; Laukhin, V., Coexistance of ferromagnetism and metallic conductivity in a molecule-based layered compound, *Nature*, **2000**, 408, 23, 447-449.

58. Forro, L.; Mihaly, L., Electronic properties of doped fullerenes, *Reports on Progress in Physics*, **2001,** 64, 649.

Chapter Two

Ligand Induced Structural Distortions in a Family of "Single-Decker" $[NEt_4]_3[Mn_5(R\text{-}salox)_3O(N_3)_6X_2]$ Single-Molecule Magnets

2.1 Introduction

There is much interest in polynuclear transition metal complexes known as single-molecule magnets (SMMs). Since the discovery of the first SMM, $[Mn_{12}O_{12}(CH_3COOH)_{16}(H_2O)_4]\bullet 2CH_3COOH\bullet 4H_2O$, "$Mn_{12}Ac$", a wide range of quantum effects have been discovered, including quantum tunneling of magnetization, thermally assisted tunneling, quantum phase interference, and spin parity effects.[1-5] SMMs are characterized by a large spin ground state, S, and large uniaxial anisotropy which is described by a negative axial zero-field splitting term, $D\hat{S}_z^2$ where D is the axial zfs parameter. The energy barrier to the reversal of magnetization between spin up and spin down states is given by $|D|\hat{S}^2$ in integer systems and $|D|(\hat{S}^2\text{-}1/4)$ in half-integer systems.

SMMs represent a "bottom-up" approach in the synthesis and characterization of nanoscale magnetic devices which has yielded a wide array of complexes. For instance, manganese SMMs range in the nuclearity from Mn_2 to Mn_{84} are known.[6, 7] The ability to alter the magnetic properties of a complex by deliberately inducing structural distortions through modifications of a ligand illustrates the synthetic versatility of SMMs. This approach has also been used to modulate intermolecular exchange interactions in $Mn_{12}Ac$, Mn_4 cubane, and Ni_4 cubane complexes resulting in the observance of new magnetic behavior.[8-10]

Recently, much attention has been given to $\mu_3\text{-}O^{2-}$ centered Mn_3^{III} triangles stabilized by tridentate oximate ligands.[11, 12] A planar arrangement of the oxime and oxo moieties promotes antiferromagnetic exchange. The structural distortion induced by increasing the torsion angle of the oximate moiety breaks the planarity of the oximate and

oxo bridging ligands that results in reduced overlap of orbitals which contribute to antiferromagnetic exchange.[13] Magneto-structural correlations in a family of Mn_6 SMMs, which consist of two off-set μ_3-O^{2-} centered Mn_3^{III} triangles, have revealed that torsion angles less than 31^o lead to antiferromagnetic exchange while angles greater than approximately 32^o lead to ferromagnetic exchange.[14, 15] The change in torsion angles was induced through the use of increasingly bulkier oximate ligands.

In the previous examples of μ_3-oxo-bridged Mn_3^{III} complexes the axial coordination sites of oxime stabilized μ_3-O^{2-} centered Mn_3^{III} triangles were occupied by solvent or carboxylate ligands. The labile nature of these axial ligands means that they can be easily replaced by other ligands. These μ_3-O^{2-}-centered Mn_3^{III} triangles provide an ideal building block for larger topologies.

A trigonal bipyramidal $Mn_2^{II}Mn_3^{III}$ complex of the formula $[NEt_4]_3[Mn_5(salox)_3O(N_3)_6Cl_2]$ where salox is salicylaldoxime, was reported by Yang et al. [16] The complex consists of a central μ_3-O^{2-} centered Mn_3^{III} triangle capped above and below the plane of the triangle by μ_2–η^1: η^1 azide bridged Mn^{II} ions. Exchange within the complex is ferromagnetic, leading to a S = 11 spin ground state. However, fits of dc magnetization indicated weak exchange between the Mn^{II} and Mn^{III} ions. Single crystal magnetization versus field hysteresis measurements revealed significant axial anisotropy with $|D|/g = -0.51\ cm^{-1}$. This complex also crystallized in one molecular orientation with no solvent molecules. It was thought that by changing the terminal halides or the coordinating oxime ligand in this complex with increasingly bulkier alkyl groups that

structural distortions would result in significant changes in magnetic exchange interactions.

Thus, a family of three trigonal bipyramidal $Mn_2^{II}Mn_3^{III}$ SMMs with identical connectivity have been synthesized in this work. The complexes have the general formula of $[NEt_4]_3[Mn_5(R\text{-salox})_3O(N_3)_6X_2]$ where R = H, Me, or Et; and X = Cl^- or Br^-. Although the three complexes possess the same overall topology and nearly identical bond connectivity, modification of the salox ligand at the oximate carbon with increasingly larger alkyl groups results in changes in structural geometry, symmetry, and crystal packing that has lead to marked changes in magnetic properties (vide infra).

2.2 Experimental Section

All procedures were carried out under aerobic conditions. Reagents were used as received unless otherwise noted. The saloxH$_2$ analogues (see Scheme 1), were synthesized according to literature procedure.[17] **Caution!** Azide salts are highly toxic and potentially explosive. Although no problems were encountered in this work, they should be prepared in small quantities and handled with care.

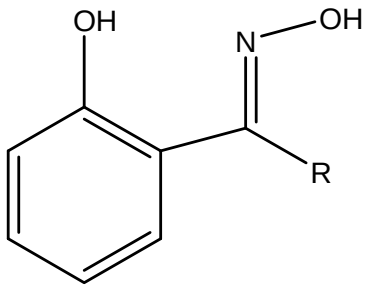

Salox

R = H, Me, Et

Scheme 1. Functionalized Salicylaldoximes

2.2.1 Compound Synthesis

$[NEt_4]_3[Mn_5O(salox)_3(N_3)_6Br_2]$ (1). $MnBr_2{\cdot}4H_2O$ (477 mg, 1.67 mmol) was dissolved in methanol (40 mL), affording a pale pink solution. NaN_3 (130 mg, 2.00 mmol) and H_2salox (137 mg, 1.0 mmol) were added consecutively. The dark green solution was stirred for 5 minutes before a 20% aqueous solution of tetraethylammonium hydroxide (0.7 mL) was added drop-wise. The dark green solution was stirred for 15 minutes before being gravity filtered and then the filtrate was layered with diethyl ether (2:1 v:v). A mixture of dark green trigonal prisms and dark brown parallelograms formed over 3 days. The prisms washed with MeOH and were hand separated in 30% yield (based on Mn). Select IR: 3387 cm^{-1} (m), 2977 cm^{-1} (m), 2078 cm^{-1} (s), 1594 cm^{-1} (m), 1436 cm^{-1} (m), 1039 cm^{-1} (m), 665 cm^{-1} (m). Elemental Analysis calculated: 36.06 %C 5.04 %H 22.43 %N. Experimental: 36.49 %C 5.14 %H 2.78 %N.

$[NEt_4]_3[Mn_5O(Me\text{-}salox)_3(N_3)_6Cl_2]$ (2). $MnCl_2{\cdot}4H_2O$ (330 mg, 1.67 mmol) was dissolved in ethanol (25 mL), affording a pale pink solution. NaN_3 (130 mg, 2.0 mmol) and Me-salox (137 mg, 1.0 mmol) were added consecutively. The dark green solution

was stirred for 5 minutes before 0.7 mL of a 20% aqueous solution of tetraethylammonium hydroxide was added drop-wise, resulting in a dark green precipitate. The dark green solution was stirred for 45 minutes before being gravity filtered and the filtrate was layered with diethyl ether (2:1 v:v). A mixture of thin dark brown plates and dark green trigonal prisms formed over 7 days. The prisms were washed with water and hand separated in 8% yield (based on Mn). Select IR: 3432 cm^{-1} (b), 2979 cm^{-1} (w), 2074 cm^{-1} (s), 1594 cm^{-1} (m), 1312 cm^{-1} (m), 670 cm^{-1} (m). Elemental Analysis calculated: 39.7 %C 5.62 %H 23.15 %N. Experimental: 37.22 %C 4.53 %H 9.07 %N.

$[NEt_4]_3[Mn_5O(Et\text{-}salox)_3(N_3)_6Cl_2]$ (3). $MnCl_2{\cdot}4H_2O$ (330 mg, 1.67 mmol) was dissolved in ethanol (25 mL), affording a pale pink solution. NaN_3 (130 mg, 2.0 mmol) and Et-salox (162 mg, 1.0 mmol) were added consecutively. The dark green solution was stirred for 5 minutes before 0.7 mL of a 20% aqueous solution of tetraethylammonium hydroxide was added drop-wise, resulting in the formation of a large amount of dark brown precipitate. The dark green solution was stirred for 45 minutes before being gravity filtered. Vapor diffusion with diethyl ether yielded thin dark green needles over 3 weeks. The crystals were washed with water and hand separated in 6% yield (based on Mn). Select IR: 3433 cm^{-1} (b), 2064 cm^{-1} (s), 1597 cm^{-1} (m), 1282 cm^{-1} (m), 1029 cm^{-1} (m), 918 cm^{-1} (m), 680 cm^{-1} (m). Elemental Analysis calculated: 41.00 %C 5.81 %H 22.5 %N. Experimental: 41.00 %C 5.36 %H 17.62 %N.

2.2.2 X-ray Crystallography

Diffraction data were collected using a Bruker Smart Apex CCD diffractometer at 100 K. The data were integrated using the Bruker SAINT software program and scaled using the SADABS software program. Complexes were solved by direct methods (SHELXL-97), developed by successive difference Fourier syntheses, and refined by full-matrix least-squares on all F^2 data. All non-hydrogen atoms were refined anisotropically by full-matrix least-squares (SHELXL-97). All hydrogen atoms were placed using a riding model. Their positions were constrained relative to their parent atom using the appropriate HFIX command in SHELXL-97.

The carbons on two of the alkyl arms of the $[NEt_4]^+$ group in complex **2** are disordered over two positions and were modeled via partial occupancy. Carbons (11, 11A), (12, 12A), and (15, 15A) were modeled with 50% occupancy. A disordered $[NEt_4]^+$ group of complex **3** was treated with the PLATON program SQUEEZE. The electron density accounted for only the one disordered $[NEt_4]^+$ group.

2.2.3 Magnetic Studies

Variable temperature dc and ac magnetic susceptibility data were collected on well ground polycrystalline samples restrained in eicosane to prevent torquing of the sample in the magnetic field. Dc magnetic susceptibility measurements were performed on a Quantum Design MPMS-5 SQUID magnetometer equipped with a 5.5 T magnet in a temperature range of 300-1.8 K in magnetic fields ranging from 0.01 to 5.0 T. AC magnetic susceptibility data were collected in a 3 Oe ac field from 10-997 Hz in zero applied dc field in a temperature range of 1.8-7.0 K. The measurements were performed

using a Quantum Design MPMS-2 SQUID magnetometer equipped with a 3 T magnet. Diamagnetic corrections were estimated from Pascal's constants[18] and subtracted from the experimental susceptibility data to obtain the molar paramagnetic susceptibility of the compounds.

2.2.4 Other Physical Measurements

Elemental analysis data were performed by Numega Resonance Laboratories (San Diego, CA). IR spectra were collected samples on powder samples in a KBr pellet on a Thermo-Nicolet Avatar 360 spectrophotometer in a range of 400-4000 cm^{-1}.

2.3 Results and Discussion

2.3.1 Discussion of Synthesis

Complexes **1**-**3** were synthesized by the addition of stoichiometric quantities of reagents to methanolic or ethanolic solutions followed by crystallization by layering or diffusion with Et_2O. Oximate ligands with increasingly larger alkyl substituents on the oximate carbon were used to increase torsion angles within the central Mn_3^{III} triangle. The functionalized salicylaldoximes were synthesized through a condensation reaction of the corresponding salicylaldehyde derivative with hydroxylamine hydrochloride. These reactions were quantitative, yielding very pure products on a large scale.

The synthesis of complexes **2** and **3** was very challenging. The complexes would form exclusively from layering or vapor diffusion. The reactions gave very poor yields and formed as many as two or three different side products. Variations in solubility had to be exploited in order to isolate products and even then it was extremely difficult to

obtain pure products. Crystals had to be hand-sorted and then washed with the appropriate solvent to ensure magnetic measurements would be made on pure samples. Carbon and hydrogen content from elemental analysis data is consistent with the expected composition. However, nitrogen content is much lower than the expected values in all three complexes. This result can be attributed to the azides thermally decomposing into N_2 gas during the analysis.

As Mn^{II} salts were used as starting material and the products are mixed valent $Mn^{II}Mn^{III}$ complexes, it is apparent that Mn^{III} ions were formed by oxidation by atmospheric O_2. The oxidation was accessed by the rapid darkening of the solution following addition of base, either NEt_4OH or NaOH, to the solution. The amount of time a reaction was stirred in air was crucial to the success of a reaction. For instance, if the reaction involving complex **2** were allowed to stir overnight, it would form a $Mn^{II}_2Mn^{III}_6$ type complex almost exclusively.

2.3.2 Description of Structures

Crystallographic data for complexes **1-3** can be found in Table 1. ORTEP representations of complexes **1-3** can be found in Figures 1-4. Summarized structural parameters for the complexes **1-3** and the $[NEt_4]_3[Mn_5(salox)_3O(N_3)_6Cl_2]$, "Mn(salox)Cl", analogue reported by Yang[16] are found in Table 2. The complexes have the general formula of $[NEt_4]_3[Mn_5(R\text{-}salox)_3O(N_3)_6X_2]$ where R = H (**1**), Me (**2**), or Et (**3**); and X = Cl^- (**2** and **3**) or Br^- (**1**). Complexes **1-3** possess a trigonal bipyramidal $Mn_3^{III}Mn_2^{II}$ topology in which a planar μ_3-oxo-centered Mn_3^{III} core is capped above and below the equatorial μ_3-O^{2-} by two axial, azide-bridged Mn^{II} ions. The three Mn^{III} ions

Table 1. Crystallographic Data for Complexes **1-3**

	1	2	3
Empirical formula	C45 H75 Br2 Mn5 N24 O7	C48 H81 Cl2 Mn5 N24 O7	C51 H87 Cl2 Mn5 N24 O7
Formula weight	1498.81	1452.18	1494.05
Temperature	100(2) K	100(2) K	100(2) K
Wavelength	0.71073 Å	0.71073 Å	0.71073 Å
Crystal system	Hexagonal	Hexagonal	Monoclinic
Space group	R3c	R3c	Cc
Unit cell dimensions	a = 13.481(5) Å	a = 13.6691(13) Å	a = 23.411(14) Å
	b = 13.481(5) Å	b = 13.6691(13) Å	b = 13.534(8) Å
	c = 60.88(2) Å	c = 60.259(6) Å	c = 22.641(12) Å
	α= 90°	α= 90°	α= 90°
	β= 90°	β= 90°	β= 101.323(8)°
	γ = 120°	γ = 120°	γ = 90°
Volume	9583(6) $Å^3$	9750.7(16) $Å^3$	7034(7) $Å^3$
Z	6	6	4
Density (calculated)	1.558 Mg/m^3	1.422 Mg/m^3	1.411 Mg/m^3
Absorption coefficient	2.277 mm^{-1}	1.090 mm^{-1}	1.012 mm^{-1}
F(000)	4584	4152	3104
Crystal color/habit	green prism	green prism	green needle
Theta range for data collection	1.87 to 27.77°	1.85 to 26.60°	1.75 to 25.55°.
Reflections collected	40270	16767	39781
Independent reflections	4079 [R(int) = 0.0611]	4153 [R(int) = 0.0401]	11738 [R(int) = 0.0724]
Completeness to theta = 25.00°	99.9 %	100.0 %	100.0 %
Data / restraints / parameters	4079 / 1 / 250	4153 / 1 / 288	11738 / 2 / 721
Goodness-of-fit on F^2	1.033	1.060	0.970
Final R indices [I>2sigma(I)]	R1 = 0.0277, wR2 = 0.0678	R1 = 0.0594, wR2 = 0.1622	R1 = 0.0497, wR2 = 0.0943
R indices (all data)	R1 = 0.0322, wR2 = 0.0693	R1 = 0.0669, wR2 = 0.1664	R1 = 0.0754, wR2 = 0.1040
Largest diff. peak and hole	0.589 and -0.488 $e.Å^{-3}$	1.186 and -0.527 $e.Å^{-3}$	0.307 and -0.349 $e.Å^{-3}$

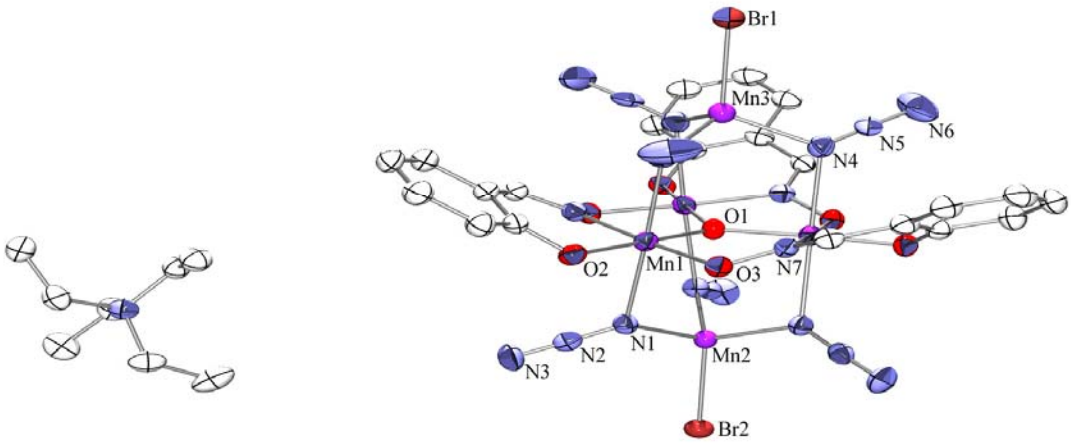

Figure 1. ORTEP of $[NEt_4]_3[Mn_5(salox)_3O(N_3)_6Br_2]$ (**1**) in POV-RAY format with thermal ellipsoids at the 50% probability level. Hydrogen atoms omitted for clarity.

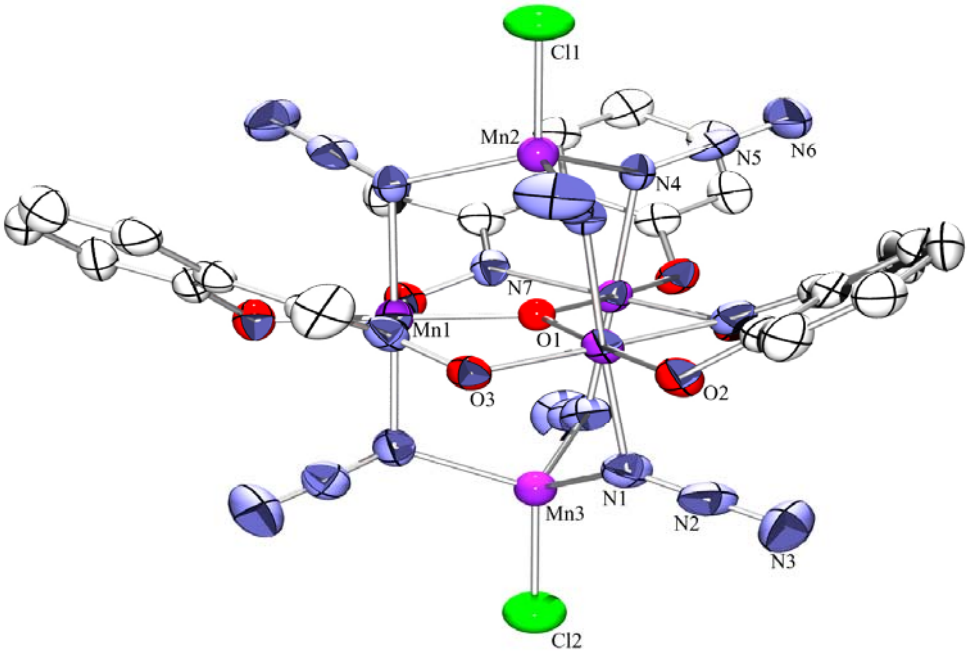

Figure 2. ORTEP of $[NEt_4]_3[Mn_5(Me\text{-}salox)_3O(N_3)_6Cl_2]$ (**2**) in POV-RAY format with thermal ellipsoids at the 50% probability level. Hydrogen and counter-ion atoms omitted for clarity.

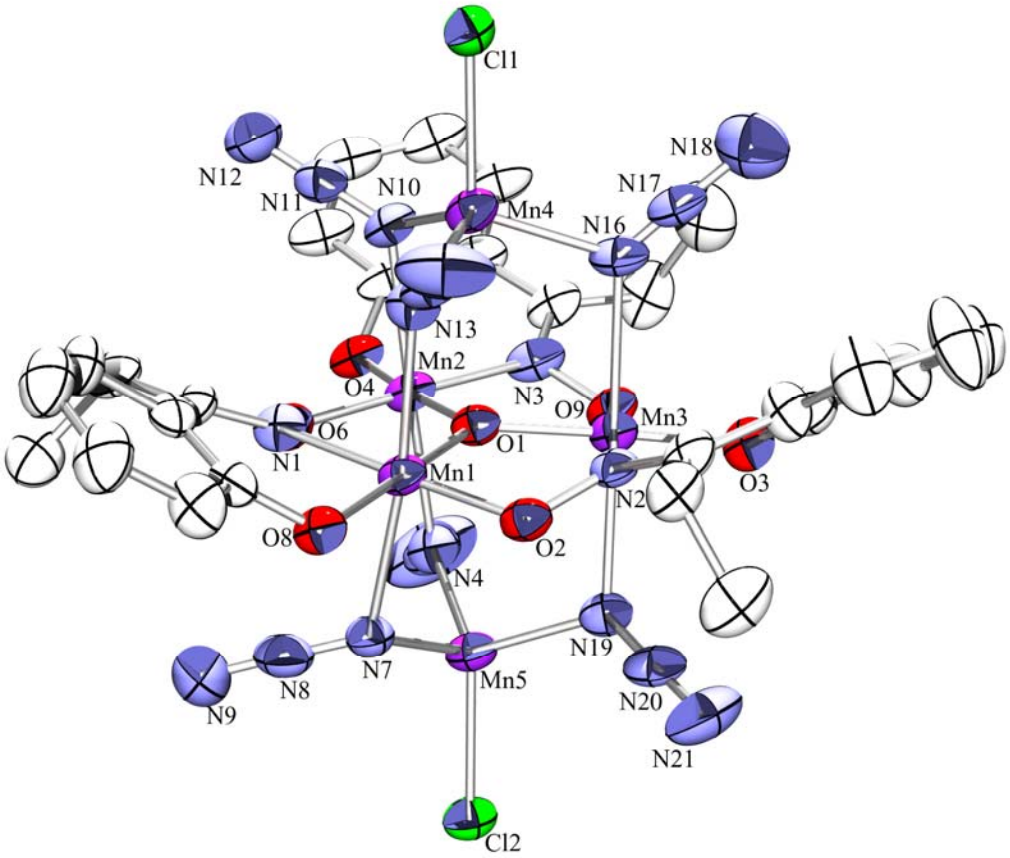

Figure 3. ORTEP of $[NEt_4]_3[Mn_5(Et\text{-}salox)_3O(N_3)_6Cl_2]$ (**3**) in POV-RAY format with thermal ellipsoids at the 50% probability level. Hydrogen and counter-ion atoms omitted for clarity.

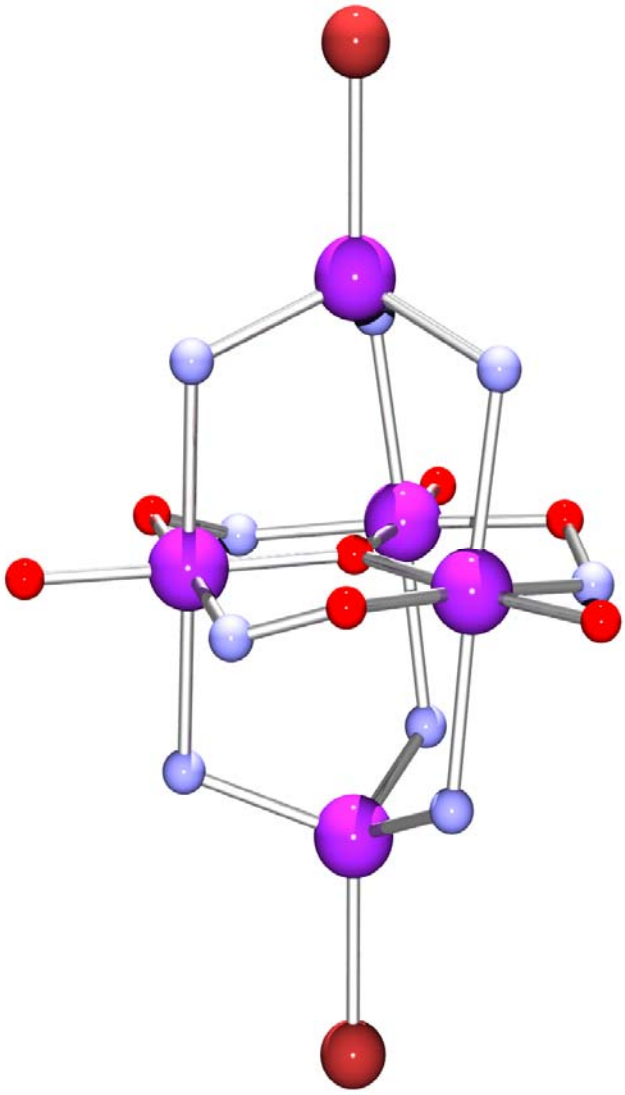

Figure 4. Rendering of the $[NEt_4]_3[Mn_5(R\text{-salox})_3O(N_3)_6X_2]$ core in POV-RAY format.

are bound by a μ_3-O^{2-}, three μ_2–η^1: η^1: η^1 oximate ligands, and six axially coordinated μ_2–η^1:η^1 azides. The azides are axially coordinated to the Mn^{III} ions (forming the Jahn-Teller axes) and bridge two tetrahedrally coordinated Mn^{II} ions with terminal halides (Cl^- or Br^-). The μ_3-O^{2-} atom of complex **1** is 0.059 Å above the plane of the Mn_3^{III} ions. The Mn(1)-N(7)-O(3)-Mn(1') moiety has a torsion angle of $\theta = 33.52^o$. The angle of the bridging azide above (Mn1-N4-Mn2) and below (Mn1-N1-Mn3) the μ_3-O^{2-} are $\theta = 109.9^o$ and 108.3^o respectively. The Mn^{III}-N_{azide} (Mn1-N4) and N_{azide}-Mn^{II} (N4-Mn2) bond distances above the μ_3-O^{2-}, respectively. The Mn^{III}-N_{azide} (Mn1-N4) and N_{azide}-Mn^{II} (N4-Mn2) bond distances above the μ_3-O^{2-} are 2.32 Å and 2.09 Å, respectively. The Mn^{III}-N_{azide} (Mn1-N1) and and N_{azide}-Mn^{II} (N1-Mn3) bond distances below the μ_3-O^{2-} are 2.31 Å and 2.07 Å, respectively.

Complex **2** has the same connectivity as complex **1**, although its terminal halides are chlorides and Me-saloxH$_2$ was used in place of saloxH$_2$. Complex **2** possesses a μ_3-O^{2-} that is 0.086 Å out of the Mn_3^{III} plane. A structural distortion induced by packing of the methyl group pendant to the oximate carbon results in a large Mn(1)-N(7)-O(2)-Mn(1') torsion angle of $\theta = 37.10^o$. The larger torsion angle causes compression of the Mn(1)-N(2)-Mn(2) angle to $\theta = 105.5^o$ and an increase in the Mn(1)-N(5)-Mn(3) angle to $\theta = 112.3^o$. The Mn^{III}-N_{azide},N(1)-Mn(3), and N_{azide}-Mn^{II}, N(4)-Mn(2) bond distances above the μ_3-O^{2-} are 2.36 Å and 2.09 Å, respectively. The Mn^{III}-N_{azide}, Mn(1)-N(1), and N_{azide}-Mn^{II}, N(1)-Mn(3), bond distances below the μ_3-O^{2-} are 2.35 Å and 2.10 Å, respectively. The increased Mn(1)-N(5)-Mn(3) angle lead to an antiferromagnetic contribution from Mn(3), resulting in a smaller spin system than complex **1**.

Complexes **1** and **2** crystallize in the hexagonal space group R3c, where an axial C_3 axis contains the apical Mn^{II} ions and the central μ_3-O^{2-}. The asymmetric unit of complexes **1** and **2** consist of 1/3 of a molecule, and one $[NEt_4]^+$ cation, the rest of the molecule being related by the C_3 axis. The complexes pack in one orientation along the c axis as a result of the c-glide crystallographic operation, as seen in Figure 3. The complexes possess only one molecular orientation and are well isolated by $[NEt_4]^+$ cations. The closest intermolecular Mn-Mn contacts for complexes **1** and **2** are 8.79 Å and 8.8 Å, respectively. Hydrogen bonding occurs between phenyl protons and the terminal halide of adjacent complexes occurs at a distance of approximately 3.35 Å. H-bonding also occurs between the terminal nitrogen of the azides and the protons of the ethyl arms of the $[NEt_4]^+$ groups at distances of 3.26 Å. Additional H-bonding occurs between the oximate and phenolate oxygens and the $[NEt_4]^+$ groups at distances of 3.19 Å and 3.95 Å.

Complex **3** is a lower symmetry analog that crystallizes in the monoclinic space group Cc as seen in the packing diagram in Figure 6. Although complex **3** has the same connectivity as complexes **1** and **2**, use of Et-saloxH$_2$ in the synthesis of this complex results in asymmetric packing of the ethyl arm pendent to the oximate carbon which results in the loss of the 3-fold symmetry axis. The complex possesses an out-of-plane μ_3-O^{2-} of 0.097 Å and large Mn-N-O-Mn torsion angles (θ = 36.05, 37.28º, 35.70º). Mn^{III}-N_3-Mn^{II} bridging angles are intermediate values above (θ = 105.31º, 105.76 º, 106.22 º) and below (θ = 108.06 º, 108.81 º, 109.27 º) the μ_3-O^{2-}. The Mn^{III}-N_{azide} bond distances are 2.34 Å, 2.37 Å, and 2.33 Å above the μ_3-O^{2-} and 2.40 Å, 2.36 Å, and 2.39 Å

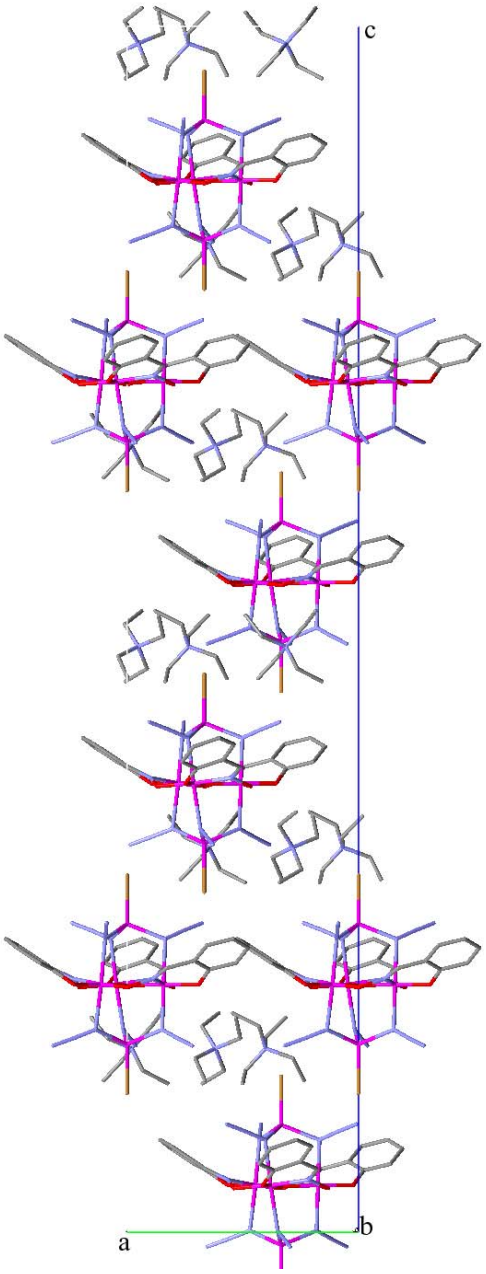

Figure 5. Crystal packing in complexes **1** and **2** as viewed down the b-axis.

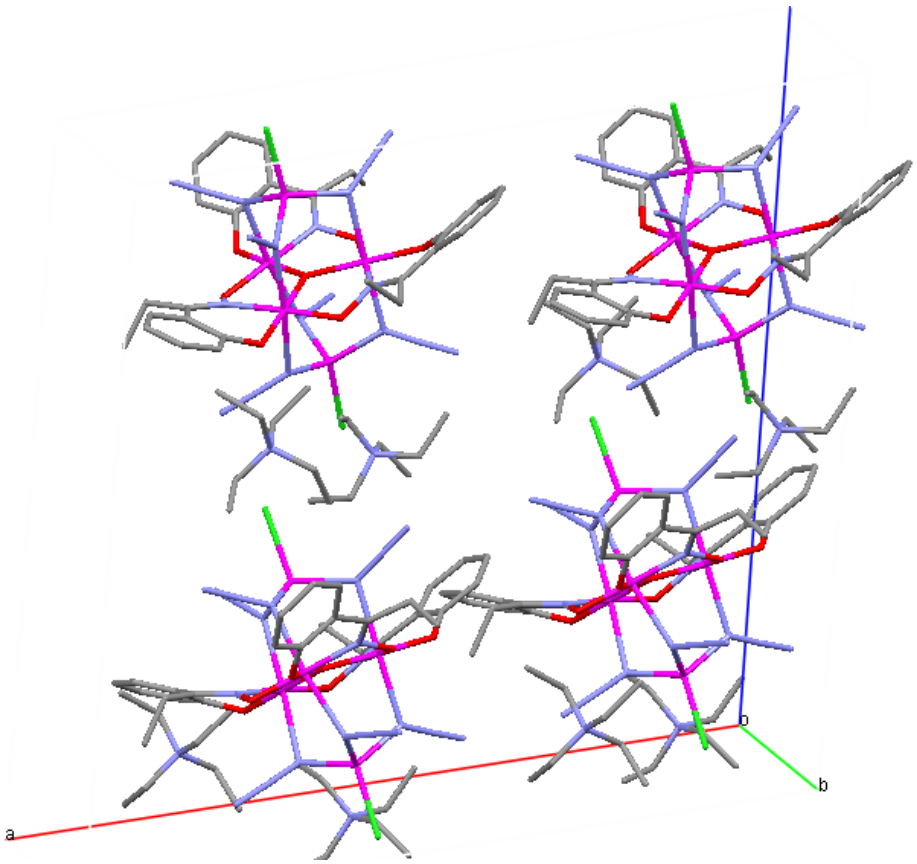

Figure 6. Crystal packing in complex **3**.

Table 2. Select Structural Parameters for Mn_5 Complexes.

Compound	Formula	out of plane μ_3-O^{-2}	Mn-N-O-Mn torsion angle (deg.)	Mn^{III}-N_3-Mn^{II} angle (a)	Mn^{III}-N_3-Mn^{II} angle (b)	Mn^{III}-N_3 bond distance (a)	N_3-Mn^{II} bond distance (a)	Mn^{III}-N_3 bond distance (b)	N_3-Mn^{II} bond distance (b)
Yang	$(NEt_4)_3[Mn_5O(salox)_3(N_3)_6Cl_2]$	0.034	33.0	107.6	109.6	2.34	2.12	2.33	2.10
1	$(NEt_4)_3[Mn_5O(salox)_3(N_3)_6Br_2]$	0.059	33.5	110	108.3	2.32	2.09	2.31	2.07
2	$(NEt_4)_3[Mn_5O(Me\text{-}salox)_3(N_3)_6Cl_2]$	0.086	37.2	105.6	112.4	2.36	2.09	2.35	2.09
3	$(NEt_4)_3[Mn_5O(Et\text{-}salox)_3(N_3)_6Cl_2]$	0.097	36.1 37.3 35.7	105.3 105.7 106.2	108.1 108.8 109.3	2.3 2.37 2.33	2.14 2.11 2.06	2.40 2.36 2.39	2.10 2.08 2.06

below the μ_3-O^{2-}. The N_{azide}-Mn^{II} bond distances are 2.14 Å, 2.11Å, and 2.06 Å above the μ_3-O^{2-} and 2.09 Å, 2.08 Å, 2.06 Å below the μ_3-O^{2-}.

The asymmetric unit of complex **3** (Figure 6) contains one molecule and three symmetry independent $[NEt_4]^+$ cations, one of which was disordered and treated with Platon SQUEEZE. The complex packs in two orientations within the unit cell as a result of application of the c-glide crystallographic operation. Weak hydrogen bonding between complexes occurs through the terminal nitrogen of the azides and the phenyl protons of adjacent complexes approximately 3.6 Å and 3.7 Å. Bond angles at distances of 3.2 Å and 3.2 Å. Very weak H-bonding also occurs between the terminal chlorides and $[NEt_4]^+$ groups with distances of approximately 3.6 Å and 3.7 Å.

2.3.3 DC Magnetic Susceptibility

Variable-temperature magnetic susceptibility measurements were preformed on complexes **1-3** using magnetic field strengths of 0.01, 0.1, and 1.0 T in a temperature range of 300-1.8 K. Bulk magnetic susceptibility measurements were carried out on well ground polycrystalline samples restrained in eicosane to prevent torquing in the applied magnetic field. Plots of molar susceptibility versus temperature (χ_mT vs. T) for complexes **1-3** are shown in Figures 7-9. Dc susceptibility data for complexes **1-3** were verified by performing measurements a minimum of two times on fresh samples.

For complex **1**, χ_mT in a 0.1 T magnetic field at 300 K is 18.44 cm^3 mol^{-1} K and increases with decreasing temperature at a gradual rate until approximately 50 K. Below 50 K, the magnetization increases rapidly with decreasing temperature to a maximum of 52.7 cm^3 mol^{-1} K at 2.81 K, followed by a sharp decrease to a local minimum of 49.9 cm^3

mol^{-1} K at 1.79 K. The drop in susceptibility is indicative of Zeeman effects and zero-field splitting. The plot of $\chi_m T$ vs. T for complex **1** in a 1.0 T field follows the same general trend as the 0.1 T plot but exhibits a smaller $\chi_m T$ max of 42.4 cm^3 mol^{-1} K at a higher temperature of 11.9 K. Below 11.9 K the $\chi_m T$ vs. T decreases rapidly to a minimum of 14.4 cm^3 mol^{-1} K at 1.8 K. The $\chi_M T$ vs. T at 300 K is larger than the 17.8 cm^3 mol^{-1} K expected using the spin only formula for a high spin $Mn^{II}_2Mn^{III}_3$ complex with g = 2.00. This and the rise to a maximum in the $\chi_M T$ supports the idea that there is ferromagnetic coupling within the $Mn^{III}_3Mn^{II}_2$ core and suggests the presence of an S=11 ground state. Previously published analogous complexes have shown that the nature of the Mn-N-O-Mn torsion angle determines exchange between Mn^{III} ions in oxime stabilized Mn_3^{III} triangles.[14] A turnover angle in the Mn-N-O-Mn torsion angle has been correlated with the sign of magnetic exchange between Mn ions. Torsion angles greater than 31-30^o tend to mediate ferromagnetic exchange interactions between the Mn^{III} ions. As complex **1** possesses Mn-N-O-Mn torsion angles of 33.5^o, ferromagnetic coupling is expected between Mn^{III} ions of the Mn_3^{III} central triangle. Exchange between Mn^{III} and Mn^{II} ions is dictated by the geometry of the end-on μ_2–η^1,η^1-azides. The most important factors in determining exchange between azide bridged metal centers in an end-on manner are the metal-N_{azide}-metal bond angle and to a lesser extent, the metal-N_{azide} bond distances.[19, 20] The $\chi_M T$ data suggests the exchange interaction between Mn^{III} and Mn^{II} ions is ferromagnetic, for the Mn-N_{azide}-Mn bond angles of 108.25^o and 109.29^o would mediate ferromagnetic exchange between Mn^{III}-Mn^{II} ions.

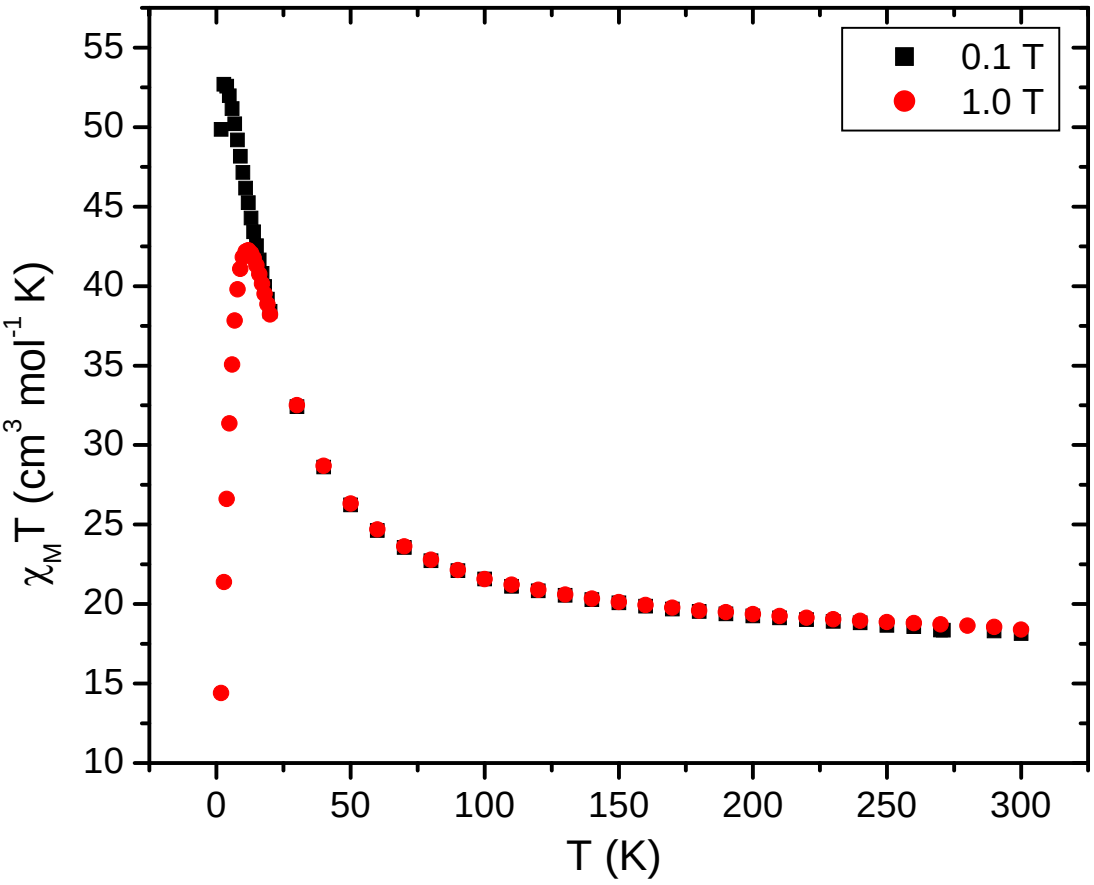

Figure 7. Plot of DC magnetic susceptibility of $[NEt_4]_3[Mn_5(salox)_3O(N_3)_6Br_2]$ (**1**).

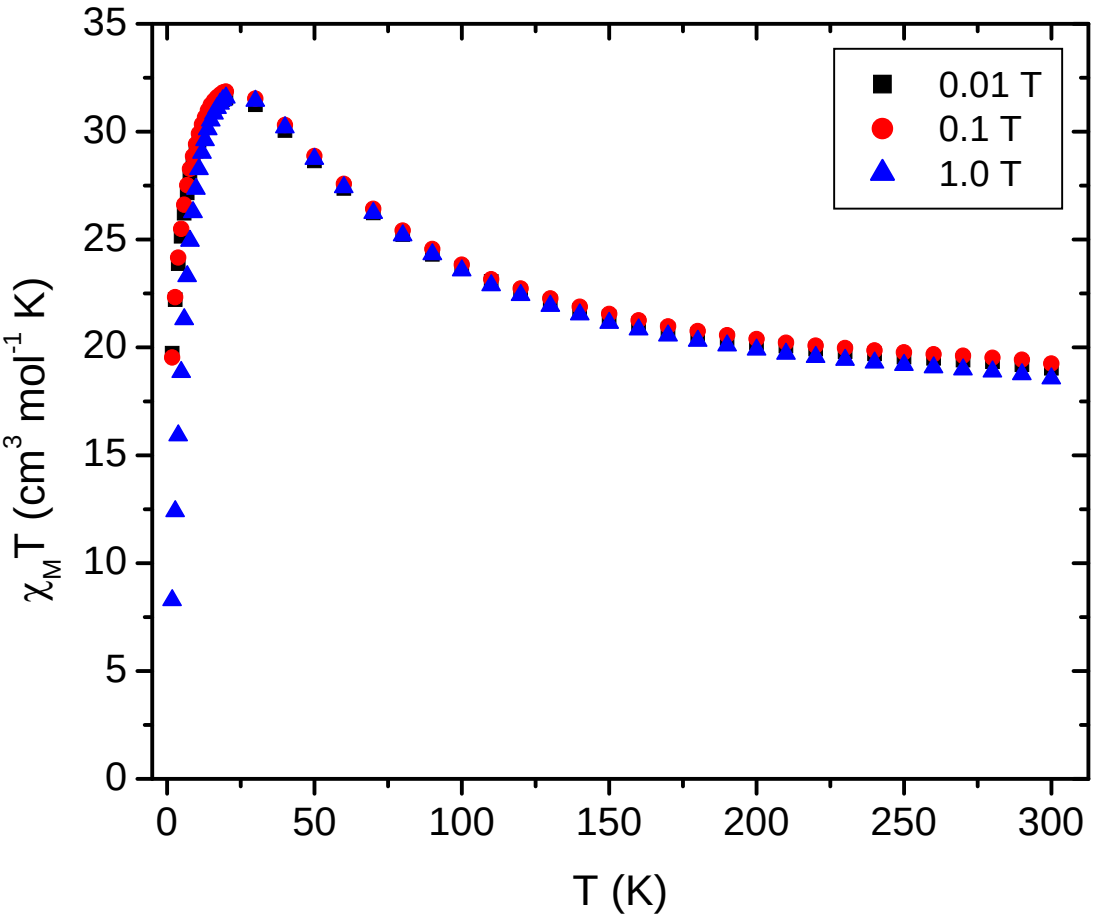

Figure 8. Plot of DC magnetic susceptibility of $[NEt_4]_3[Mn_5(Me\text{-}salox)_3O(N_3)_6Cl_2]$ (**2**).

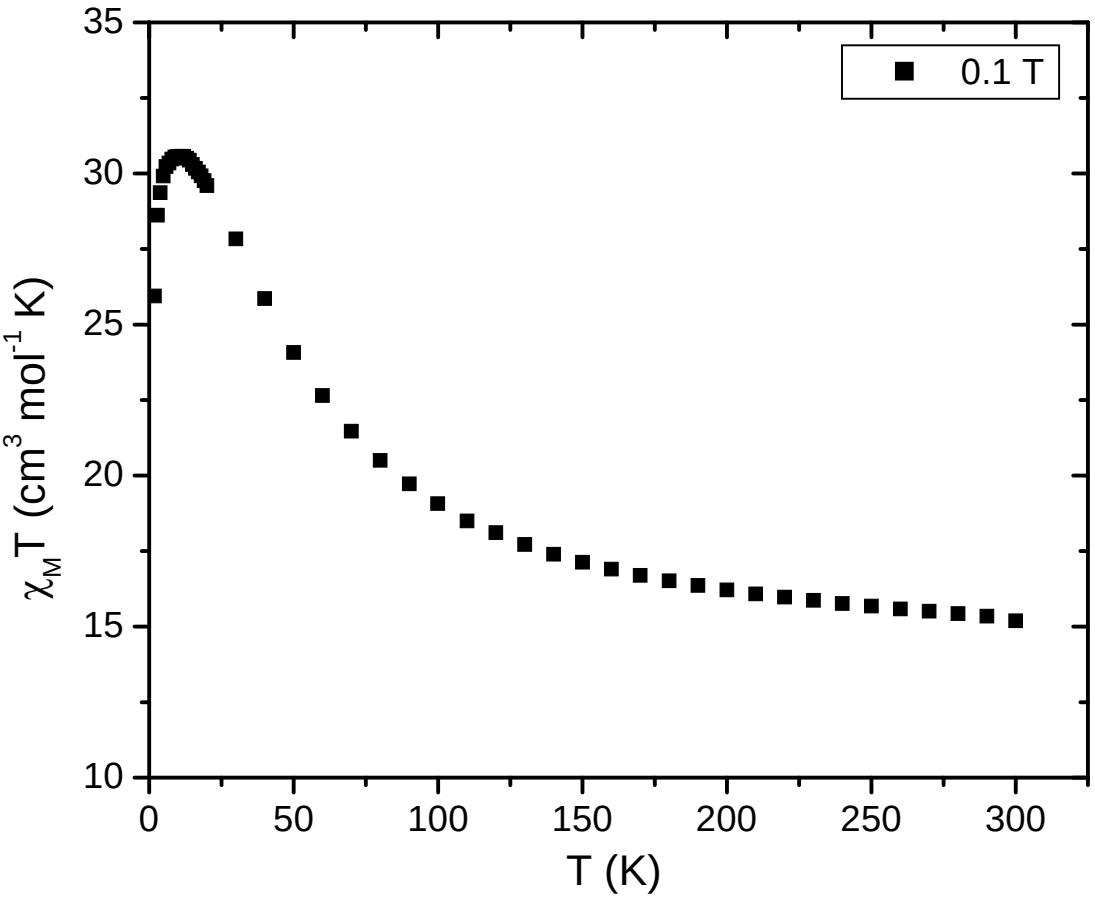

Figure 9. Plot of DC magnetic susceptibility of $[NEt_4]_3[Mn_5(Et\text{-}salox)_3O(N_3)_6Cl_2]$ (**3**).

In a field of 0.01 T at 300 K, $\chi_m T$ for complex **2** is 19.0 cm^3 mol^{-1} K and then increases with decreasing temperature at a steady rate until approximately 120 K, at which point the magnetization increases more rapidly to a maximum of 31.6 cm^3 mol^{-1} K at 20 K and then decreases rapidly to 19.7 cm^3 mol^{-1} K at 1.8 K. The value of $\chi_M T$ at 300 K is also larger than the expected $\chi_M T$ for non-interacting $Mn^{III}_3Mn^{II}_2$ ions with g = 2.00. The $\chi_m T$ vs. T plots for complex **2** in 0.1 and 1.0 T fields follow the same general trend as in the 0.01 T field but exhibits a slightly larger $\chi_m T$(max) of 31.9 cm^3 mol^{-1} K and 31.6 cm^3 mol^{-1} K, respectively, both of which occur at approximately 20 K. Below 20 K the $\chi_m T$ vs. T for 0.1 and 1.0 T fields decrease rapidly to a minima of 19.5 cm^3 mol^{-1} K and 8.23 cm^3 mol^{-1} K at 1.8 K, respectively. The plot clearly demonstrates ferromagnetic behavior but the smaller $\chi_M T$ max at the same fields as complex **1** indicates that the Mn ions within the complex are not entirely ferromagnetically aligned. The large Mn-N-O-Mn torsion angle of 37.1° would imply ferromagnetic exchange within the central Mn_3 triangle. The decrease in the Mn^{III}-N_{azide}-Mn^{II} (Mn1-N5-Mn3) bond angle "above" the μ_3-oxo to 105.5° is in the range of mediating ferromagnetic exchange. The increase in the Mn^{III}-N_{azide}-Mn^{II} (Mn1-N5-Mn3) bond angle "below" the μ_3-oxo to 112.32° possibly results in an antiferromagnetic contribution from Mn(3). The antiferromagnetic Mn^{II} ion would cancel the contribution from the ferromagnetic Mn^{II} ion, resulting in an S = 6 ground state from the ferromagnetically coupled Mn_3^{III} core.

In a 0.1 T field, $\chi_M T$ for complex **3** begins at 15.2 cm^3 mol^{-1} K at 300 K and increases with decreasing temperature at a steady rate until about 150 K, at which point it increases rapidly with decreasing temperature to a maximum of 30.6 cm^3 mol^{-1} K at 9.9

K. $\chi_M T$ then decreases rapidly to a minimum of 25.9 cm^3 mol^{-1} K at 1.8 K. Again, the decrease in $\chi_M T$ data is suggestive of an antiferromagnetic contribution from one of the Mn^{II} ions. This lower symmetry analogue has three unique Mn-N-O-Mn torsion angles which are all over 35^o and Mn-N_{azide}-Mn bond angles less than 110^o. However, the Mn^{III}-N_{azide} bond distances on the "lower" half of the triangle are close to 2.4 Å. The increased bond distance, coupled with the larger Mn-N_{azide}-Mn angle of approximately 109^o possibly results in antiferromagnetic exchange from the "lower" Mn^{II} ion due to decreased overlap between orbitals between the Mn^{III} ions and the azide.

Variable-field magnetic susceptibility studies were performed on complexes **1**-**3** in order to determine both the spin of the ground state and the magnitude of the zero-field splitting parameter for D. In the reduced magnetization experiment, high magnetic fields of 1-5 T are applied in a temperature range of 1.8-4.0 K. A plot of reduced magnetization ($M/N\mu_B$) versus field (H/T) is obtained, where M is the magnetization, N is Avogadro's number, μ_B is the Bohr magneton, and H/T is the magnetic field divided by the absolute temperature. At these low temperatures it is hoped that only the ground state is populated.

Susceptibility data were fit using the program AXFIT which assumes a well isolated spin ground state and incorporates a full powder average. The data were least-squares fit in order to determine a global minimum for parameters. Plots of reduced magnetization data for complexes **1**-**3** are shown in Figures 10-12.

For complex **1**, magnetization reaches a saturation value close to 19 $M/N\mu_B$ at the highest field and lowest temperature which is slightly less than the expected value of g•S

= 22 for a S = 11 ground state for a ferromagnetically coupled $Mn^{II}_2Mn^{III}_3$ complex with g = 2.0. For complex **1**, least-squares fitting of reduced magnetization data for fields of 2-5 T yielded parameters of S = 10, g = 1.99, and D = -0.20 cm^{-1} (-0.29 K). This fit confirms ferromagnetic coupling within the $Mn_2^{II}Mn_3^{III}$ magnetic core.

For complex **2**, the magnetization saturates near 12 $M/N\mu_B$. Least-squares fitting of the 3, 4, and 5 T data revealed an S = 7 ground state, with g = 2.01, and D = -0.71 cm^{-1} (-1.02 K). The S = 7 ground state confirms the suspected antiferromagnetic contribution from Mn(3) due to the large Mn^{III}-N_{azide}-Mn^{II} bond angle.

Magnetization for complex **3** saturates at 13 $M/N\mu_B$. The 1-5 T magnetization data for complex **3** was least-squares fit, yielding parameters of S = 7, g = 1.95, and D = -0.50 cm^{-1} (-0.72 K). As with complex **2**, structural distortions in the bridging azide resulted in an antiferromagnetic contribution from the "lower" Mn^{II} ion.

An analogous complex of the formula $[NEt_4]_3[Mn_5(salox)_3O(N_3)_6Cl_2]$ reported by Yang et al.[16] possesses a ferromagnetically coupled Mn_5 core. The complex has structural geometries similar to complex **1**. The Mn-N-O-Mn torsion angle is approximately 33°. The Mn-N_{azide}-Mn bond angles are 107.6° above the μ_3-oxo and 109.6° below the μ_3-oxo with comparable bond distances. A least-squares fit of reduced magnetization data gave parameters of S = 11, g = 1.90, and D = -0.22 cm^{-1} (-0.32 K) with a calculated barrier of 26.6 cm^{-1}.ref A fit of the $\chi_M T$ data using a two J value Kambe model revealed an S = 10 excited state that was separated by only 3.2 cm^{-1}. The model treated exchange between Mn^{III}-Mn^{II} ions as equivalent, even though crystallographic data clearly indicates that the geometries of the Mn^{II} ions are different. The J values obtained by the fit are J(Mn^{III}-Mn^{II}) = 0.23 cm^{-1} and J(Mn^{III}-Mn^{III}) = 2.41

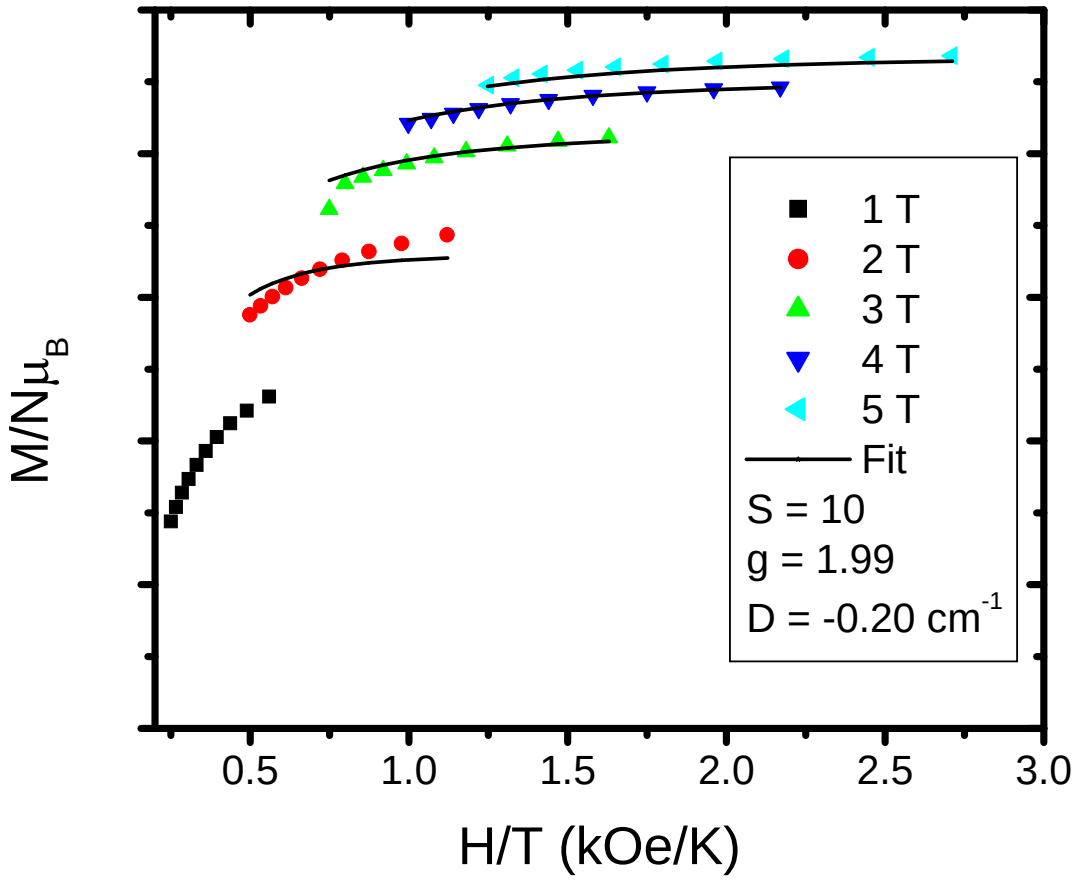

Figure 10. Plot of reduced magnetization for $[NEt_4]_3[Mn_5(salox)_3O(N_3)_6Br_2]$ (**1**).

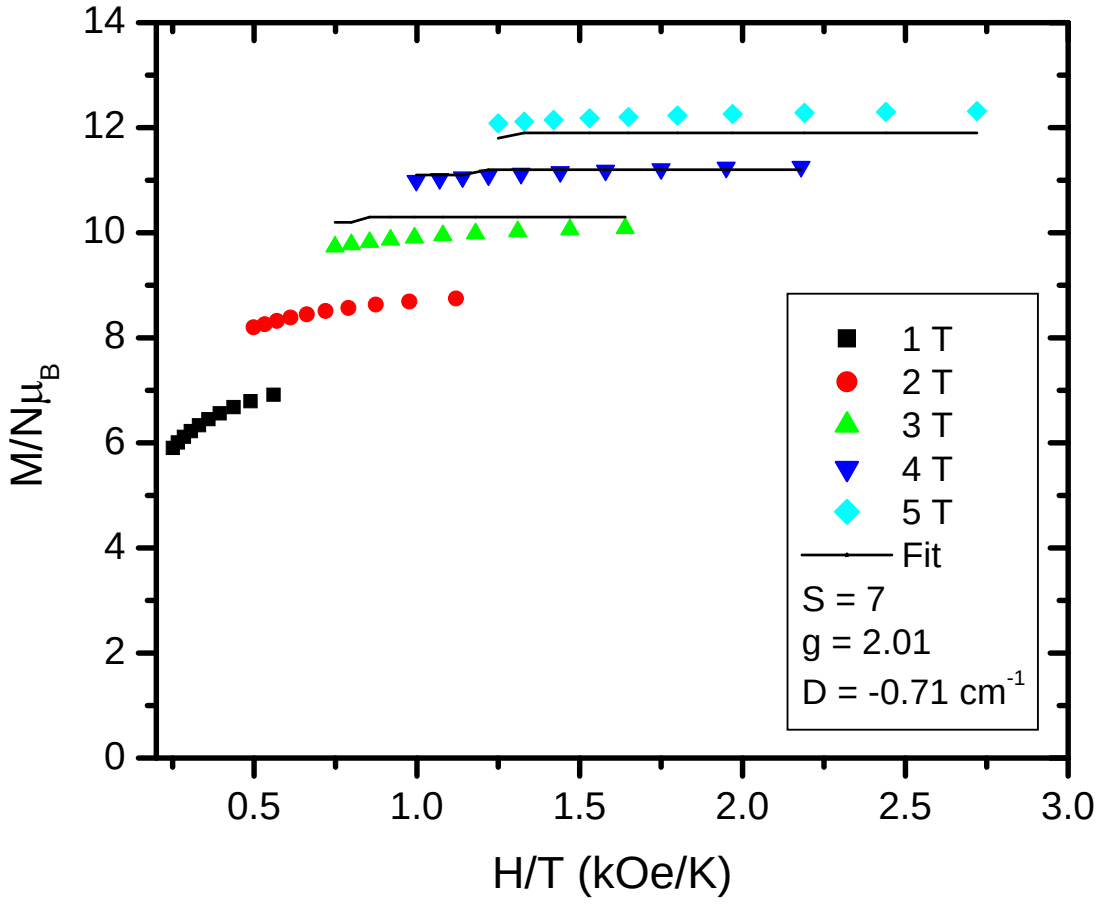

Figure 11. Plot of reduced magnetization for $[NEt_4]_3[Mn_5(Me\text{-}salox)_3O(N_3)_6Cl_2]$ (**2**).

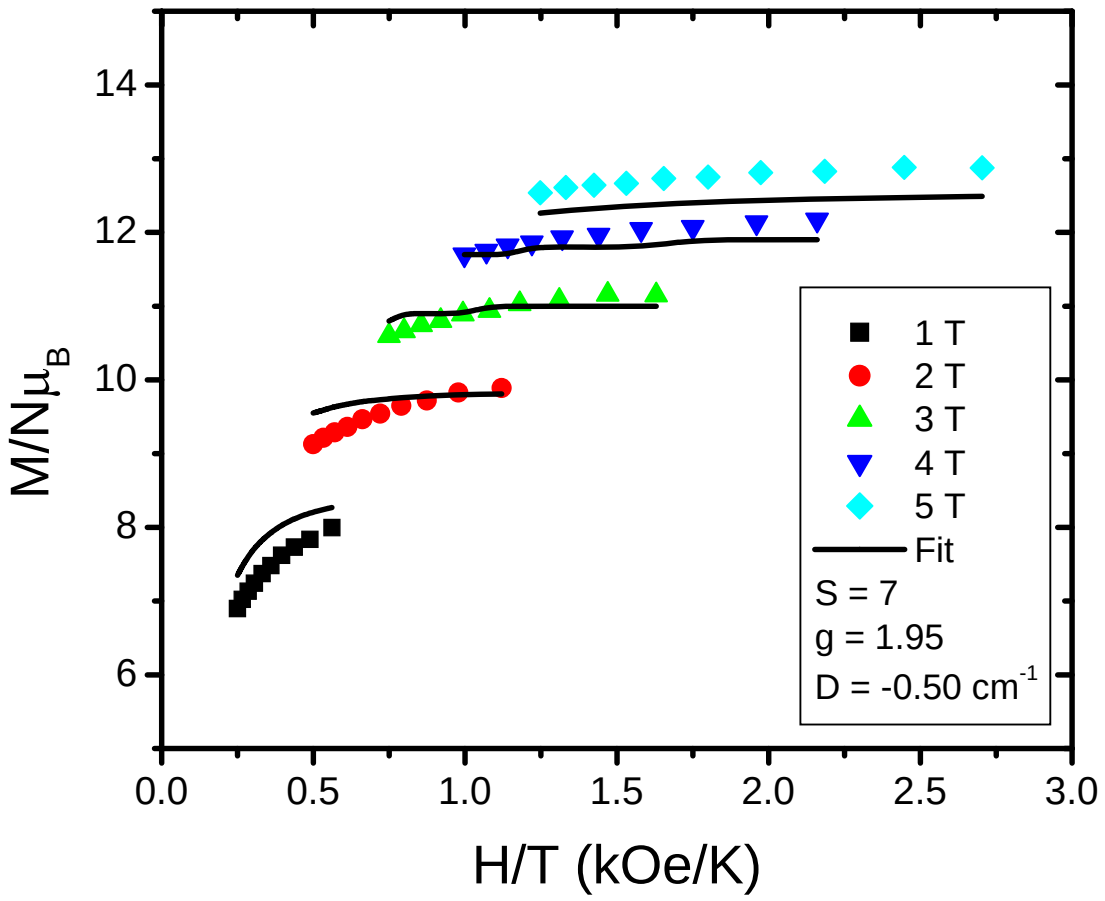

Figure 12. Plot of reduced magnetization for $[NEt_4]_3[Mn_5(Et\text{-}salox)_3O(N_3)_6Cl_2]$ (**3**).

cm^{-1}. These values imply that exchange between Mn^{III}-Mn^{II} ions is substantially weaker than exchange within the Mn_3 triangle. This explains why seemingly small geometric changes in the metal-N_{azide} bond angles and bond distances in complexes **2** and **3** had such a large impact on the exchange between Mn^{III} and Mn^{II} ions.

To summarize, trends in $\chi_M T$ data suggested an S = 11 spin ground state in **1** and S = 6 or 7 spin ground states in complexes **2** and **3**. Although no fits of $\chi_M T$ data were obtained, magneto-structural trends in analogous complexes were used to justify the observed magnetic behavior. This was confirmed by fits of reduced magnetization data. However, complexes with weak exchange are typically complicated by the presence of low lying excited states. As the model assumes a well isolated spin ground state and an analogous complex has a first excited state very close in energy to its ground state, it explains in part why good fits of magnetization data were not obtained.

2.3.4 AC Magnetic Susceptibility

The barrier to reversal of magnetization can be measured through the alternating current magnetic susceptibility measurement. The energy barrier (U_{eff}) can be measured by applying the Arrhenius equation to ac susceptibility data.

$$\ln(1/\tau) = \ln(1/\tau_o) - U_{eff}/kT \qquad (2.1)$$

An Arrhenius plot is constructed in which the natural log of the reciprocal of the oscillating frequency is plotted against the inverse of the temperature at which a peak maximum occurs for each frequency. U_{eff} is obtained by calculating the slope of the Arrhenius plot. Ac magnetic susceptibility measurements were made on polycrystalline samples of complexes **1**-**3** in the 1.8-7.0 K range in zero applied dc field with 3.0 G ac field oscillating at frequencies of 10, 25, 50, 100, 250, 500, 750, and 997 Hz. The in-

phase (χ_M') and the out-of-phase (χ_M") components versus temperature for complexes **1-3** are presented in the top and bottom portion of Figures 13-16.

The frequency dependent amplitude of the in-phase for complex **1** increased with decreasing temperature until it reached a maximum at 3.14 K at 50 Hz and then decreases to a minimum at 1.8 K. The out-of-phase component is almost one half of the in-phase component at approximately 2.5 K. The out-of-phase component shows a clear frequency and temperature dependence. As the frequency was lowered from 997 to 10 Hz, the peak centers shifted from 3.48 to 2.64 K. The peak shape changes from Lorentzian at higher frequencies to Gaussian below 100 Hz. The change from Lorentzian to Gaussian behavior can be due to the presence of more than one relaxation process. Although the exact origin of the additional relaxation processes remains unknown, complex **2** has better crystal quality than the Yang complex. This means relaxation mechanisms arising from microenvironments and crystallographic distortions are very small. Fitting of χ_M" to the Arrhenius equation yielded a U_{eff} = 36.6 K. Extrapolation of the in-phase susceptibility, plotted as χ_M'T versus T, to 0 K yielded a value of 65.1 cm^3 mol^{-1} K which is close to the spin only χT of 66.0 cm^3 mol^{-1} K for S = 11. This result is suggests a larger spin ground state than that which was obtained from reduced magnetization.

Complex **2** exhibited similar behavior to complex **1**. The in-phase component displays the expected frequency dependence. The out-of-phase component is only one third of the in-phase component at 3.5 K. The peak centers of the out-of-phase signal shifted from 4.34 K at 997 Hz to 3.47 K at 100 Hz. The peak shape displayed well-fit Gaussian behavior at all frequencies. Fitting of 100-997 Hz χ_M" data to the Arrhenius

equation resulted in values of U_{eff} = 39.8 K. Complexes **1** and **2** have roughly the same formula and crystallize in the same hexagonal R3c space group with little variation in crystal packing. Yet complex **2** has a barrier 3.4 K larger than complex **1** while having a smaller over all spin. A higher spin ground state does not necessarily lead to slower relaxation. Mixing of excited states into the spin ground state has been shown to lead to faster relaxation processes. Complexes with weak exchange typically have low lying excited states.[21] The larger torsion angle of **2** results in stronger exchange within the Mn_3^{III} core which can lead to a more isolated spin ground state than complex **1**, resulting in a larger U_{eff}. The in-phase component was plotted as $\chi_M T$' versus temperature and extrapolated to 0 K (Figure 21). A value of 17.9 cm^3 mol^{-1} K was obtained, which is in between spin only values of 15.0 cm^3 mol^{-1} K for a S = 5 and 21.01 cm^3 mol^{-1} K for a S = 6 ground state.

The frequency dependent in-phase component of complex **3** increased with decreasing temperature from 3.64 $\chi_m T$' at 7.0 K to a maximum of 7.25 χ_m' at 3.98 K for 10 Hz. The 997 Hz $\chi_m T$" exhibited a peak center at 4.09 K and shifted to lower temperature with decreasing frequency to 2.81 K at 10 Hz. The out-of-phase component followed Lorentizian behavior at all frequencies. This suggests the presence of more than relaxation pathway. The lower crystallographic symmetry, poorer crystal quality, and disordered counter-ions could result in environmental relaxation pathways. A fit of 10-997 Hz data to the Arrhenius equation gave parameters of U_{eff} = 39.6 K. The in-phase

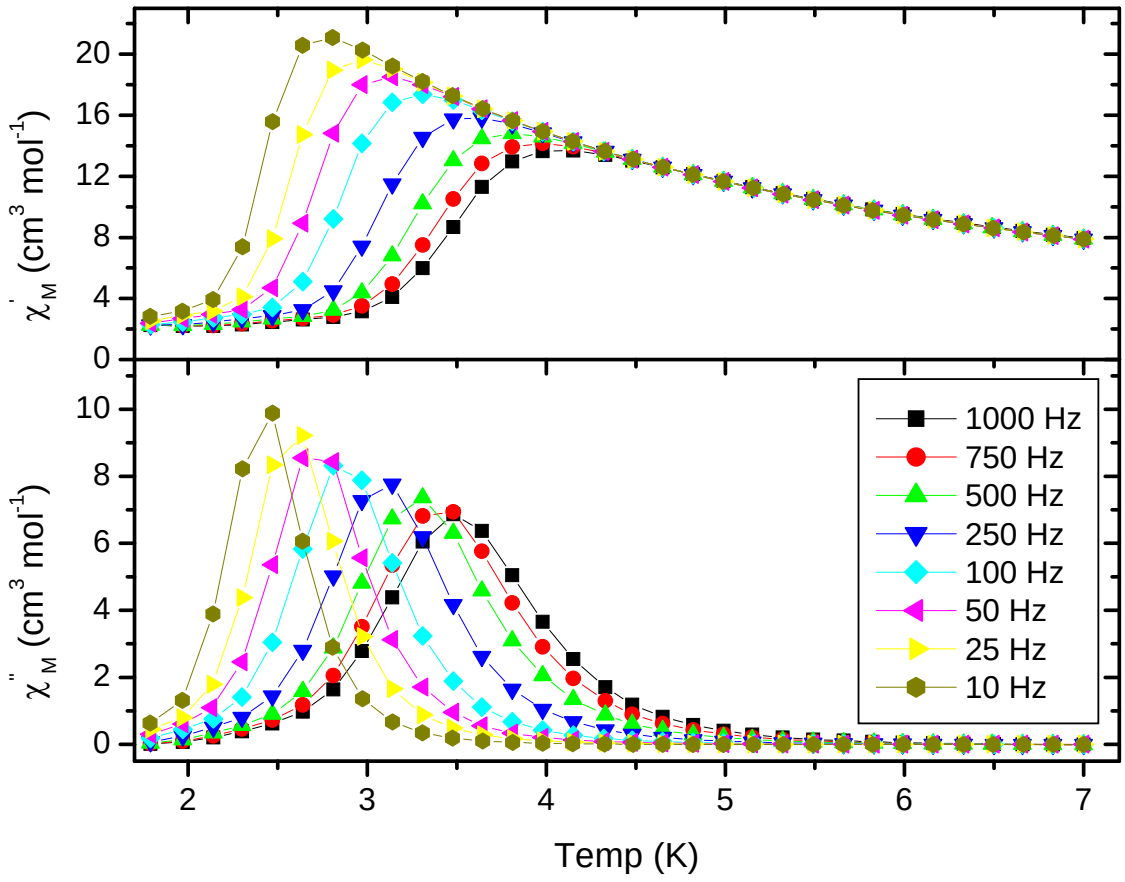

Figure 13. AC susceptibility plot of complex **1** $[NEt_4]_3[Mn_5(salox)_3O(N_3)_6Br_2]$. Lines serve to guide the eye.

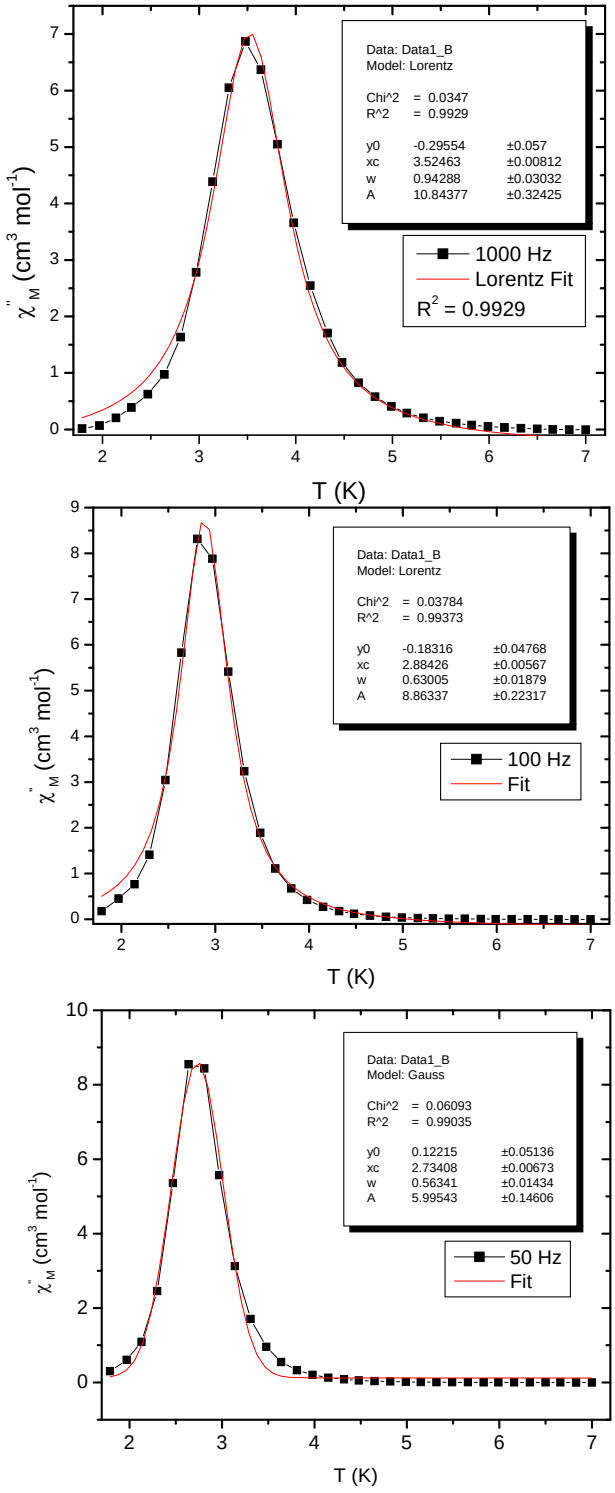

Figure 14. Fits of AC susceptibility data of complex **1** $[NEt_4]_3[Mn_5(salox)_3O(N_3)_6Br_2]$ to Lorentzian from 1000-100 Hz and Gaussian from 50-10 Hz .

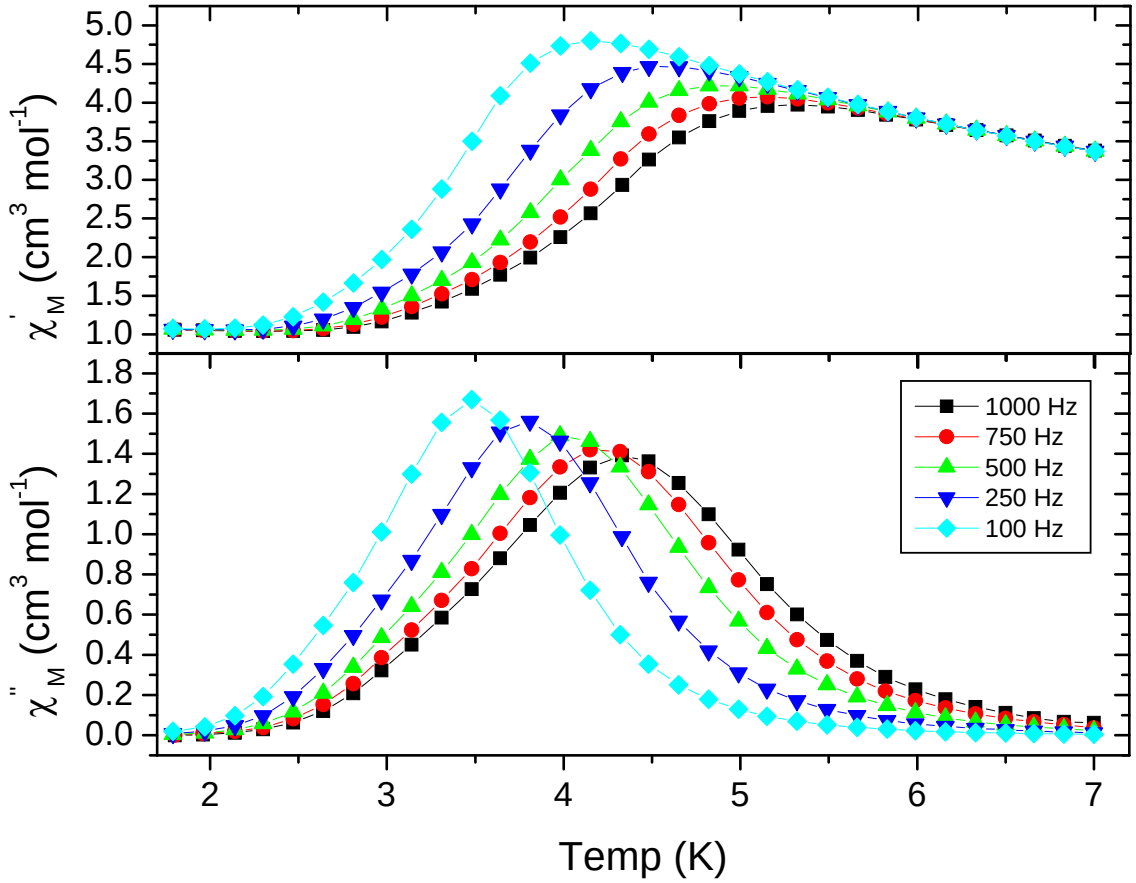

Figure 15. AC susceptibility plot of complex **2** $[NEt_4]_3[Mn_5(Me\text{-}salox)_3O(N_3)_6Cl_2]$. Lines serve to guide the eye.

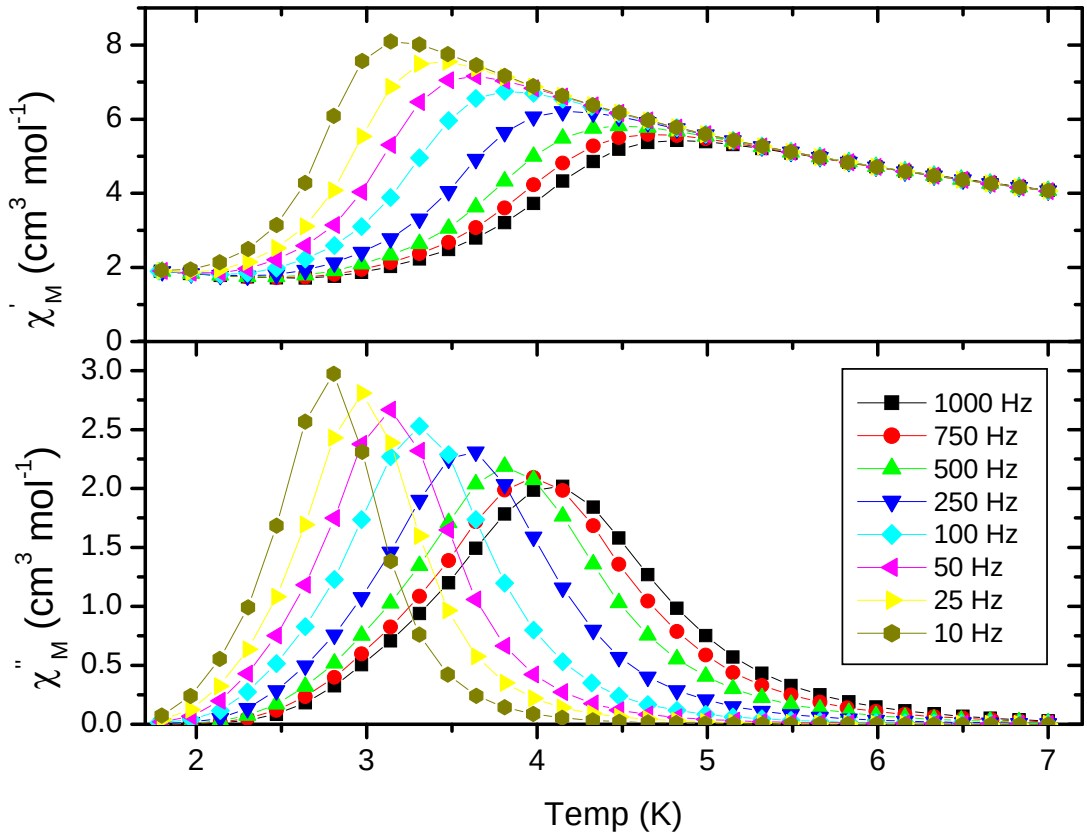

Figure 16. AC susceptibility plot of complex **3** $[NEt_4]_3[Mn_5(Et\text{-}salox)_3O(N_3)_6Cl_2]$. Lines serve to guide the eye.

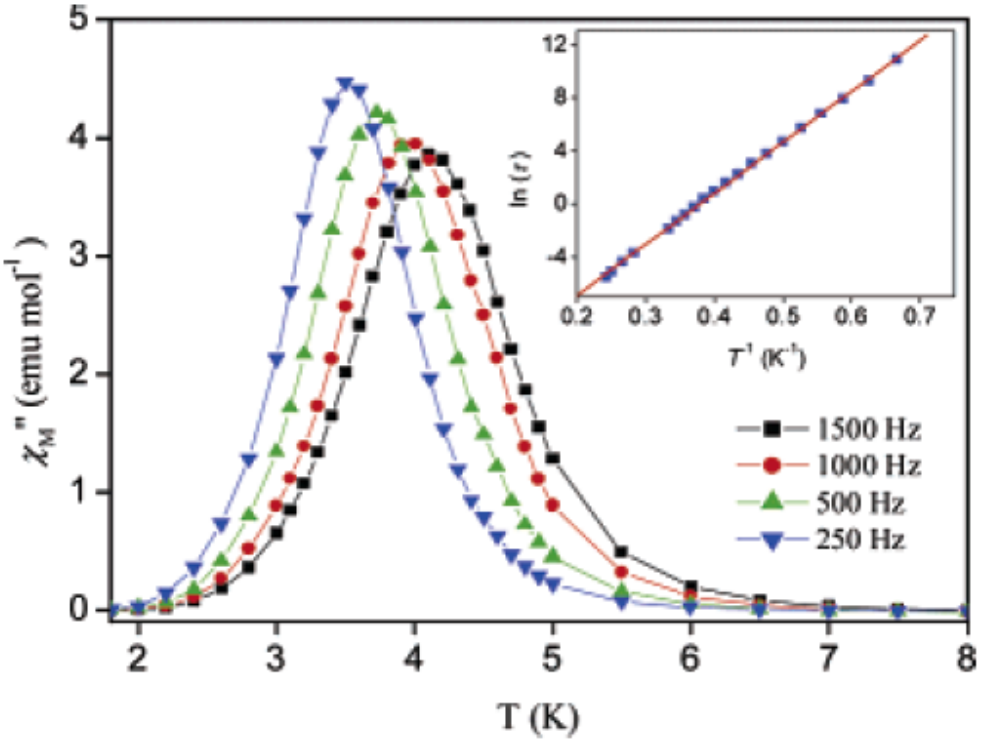

Figure 17. Out-of-phase AC susceptibility plot of **[**$NEt_4]_3[Mn_5(salox)_3O(N_3)_6Cl_2]$. Lines serve to guide the eye.[16]

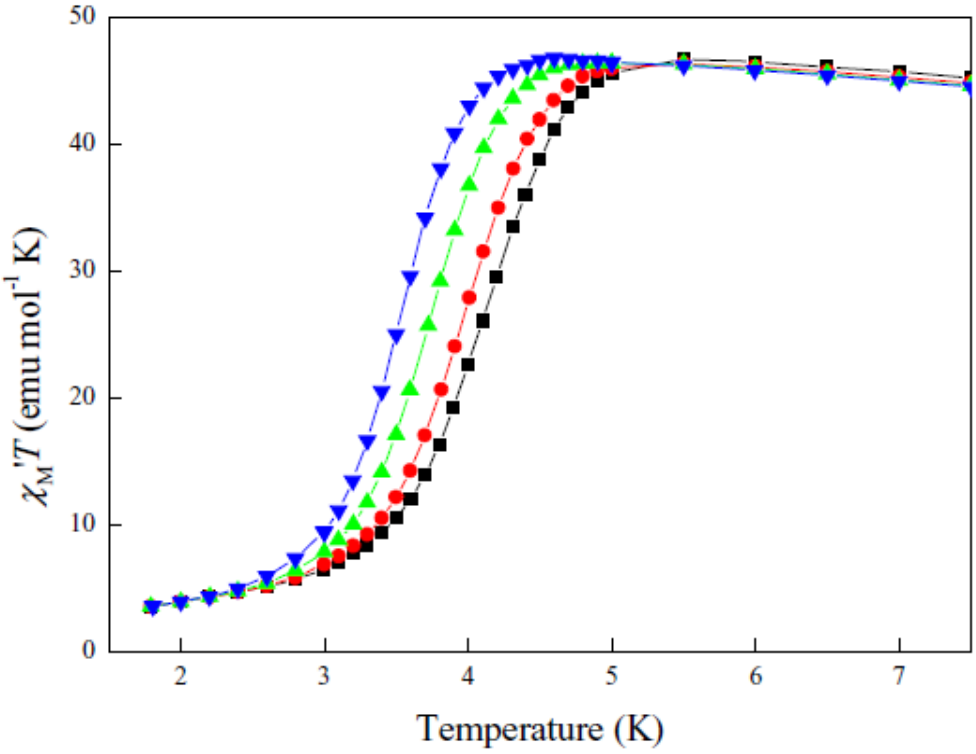

Figure 18. In-phase AC susceptibility plotted as χ_M'T vs T of $[NEt_4]_3[Mn_5(salox)_3O(N_3)_6Cl_2]$. Lines serve to guide the eye.[16]

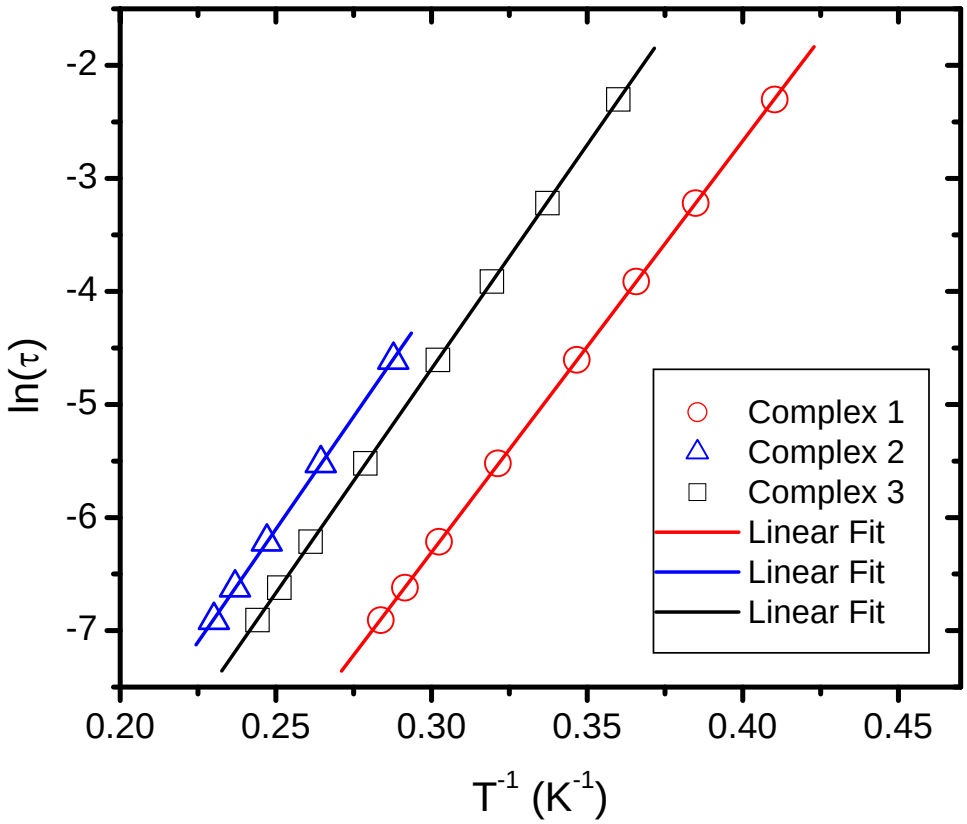

Figure 19. Plots of ln(τ) versus 1/T obtained from ac susceptibility data for complexes **1-3**.

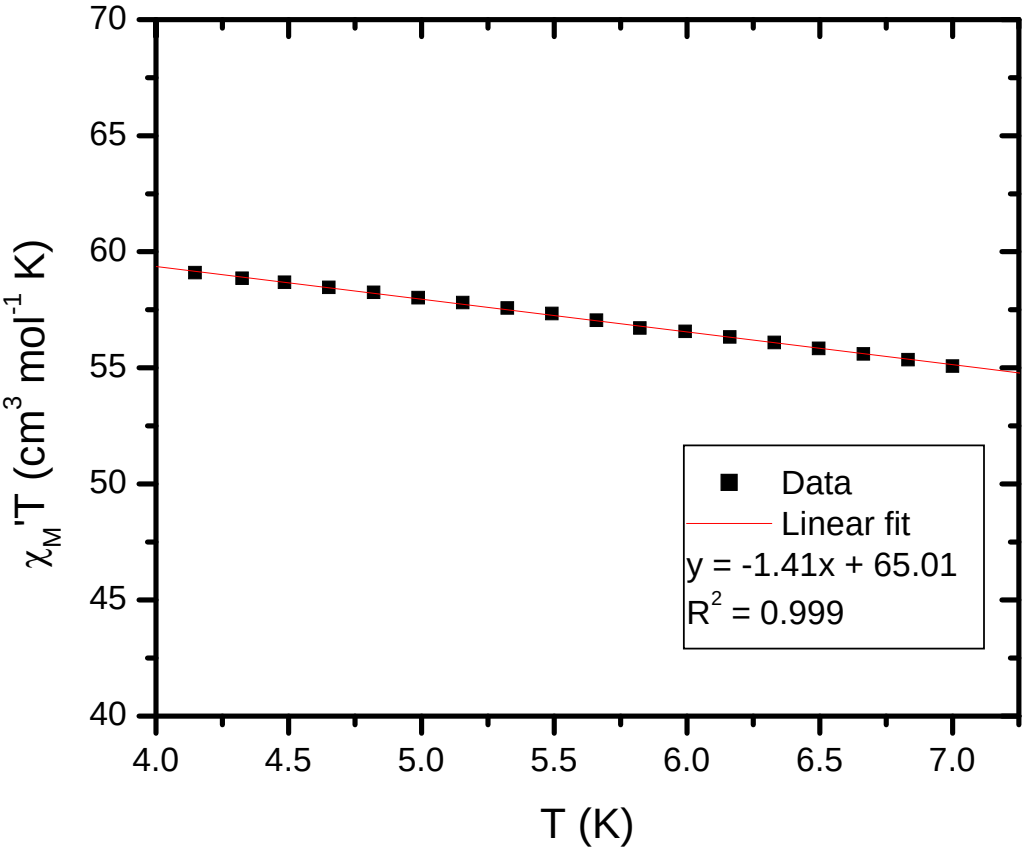

Figure 20. Plot of χ_M'T versus T extrapolated to 0 K for complex **1**.

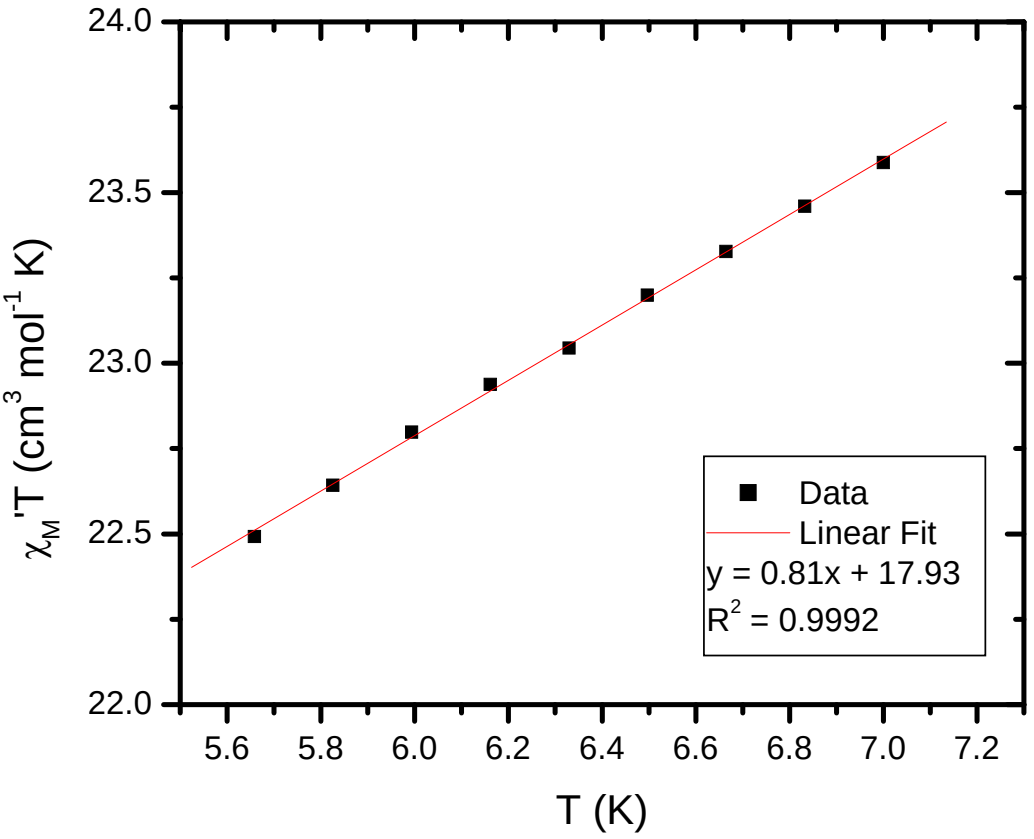

Figure 21. Plot of χ_M'T versus T extrapolated to 0 K for complex **2**.

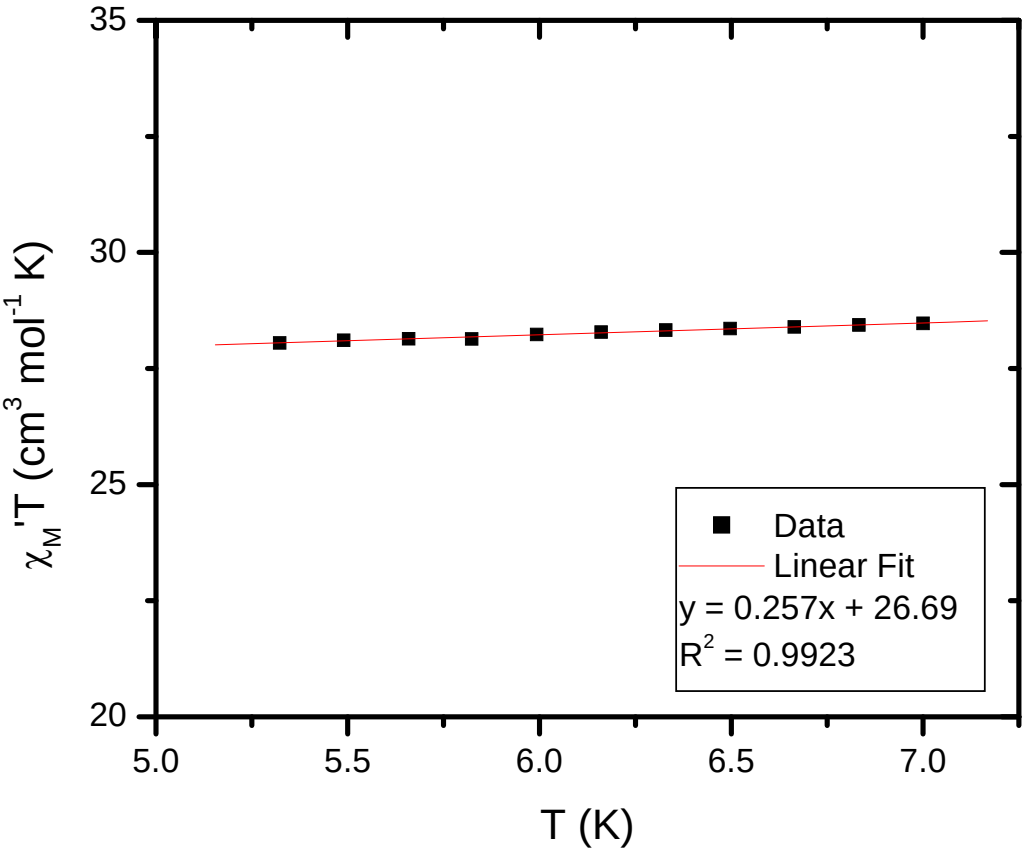

Figure 22. Plot of χ_M'T versus T extrapolated to 0 K for complex **3**.

Table 3. Summarized Magnetic Data for Mn_5 Complexes.

Compound	Formula	S	D (cm^{-1})	g	U_{eff} (K)
Yang	$(NEt_4)_3[Mn_5O(salox)_3(N_3)_6Cl_2]$	11	-0.22	1.89	40.3
1	$(NEt_4)_3[Mn_5O(salox)_3(N_3)_6Br_2]$	10	-0.20	1.99	36.6
2	$(NEt_4)_3[Mn_5O(Me\text{-}salox)_3(N_3)_6Cl_2]$	7	-0.71	2.01	39.8
3	$(NEt4)_3[Mn_5O(Et\text{-}salox)_3(N_3)_6Cl_2]$	7	-0.50	1.95	39.6

component was plotted as $\chi_M T$' versus temperature and extrapolated to 0 K (Figure 22). A value of 26.7 cm^3 mol^{-1} K was obtained, which is close to the spin only value of 28.0 cm^3 mol^{-1} K for S = 7 ground state, confirming the fit of the reduced magnetization.

Ac susceptibility data for the Yang[16] complex is shown in Figures 17 and 18. The data reported by Yang were collected in a temperature range of 1.8-8.0 K in zero applied field and with a 3.5 G ac field at frequencies of 1500, 1000, 500, 250 Hz. The complex exhibited Gaussian behavior at all frequencies. However, lower frequency data were not reported making comparisons in the trends of the peak shape difficult. The effective barrier obtained from fitting the ac susceptibility data is 40.3 K. The peak center at 1000 Hz is close to 4 K which is approximately 0.5 K higher in temperature than complex **1**. Mn-N-O-Mn torsion angles of this complex are almost identical to complex **1**. The larger U_{eff} is most likely the result of a more isolated ground state than complex **1**. The complex has shorter azide bond angles than **1**. This promotes stronger ferromagnetic exchange between Mn^{III} and Mn^{II} ions resulting in a more isolated ground state than **1**.

2.4 Conclusion

A series of three SMMs with the general formula of $[NEt_4]_3[Mn_5(R\text{-}salox)_3O(N_3)_6X_2]$ where R = H, Me, or Et; and X = Cl^- or Br^- have been synthesized. Their properties were characterized by X-ray crystallography and bulk susceptibility measurements. Data from these measurements suggest spin ground states of S = 10, 7, and 7 for complexes **1**-**3**, respectively. The kinetic barrier to reversal of magnetization (U_{eff}) was obtained through ac susceptibility studies are 36.6 K, 39.8 K, and 39.6 K for complexes **1**-**3**, respectively.

Structural changes were induced by changing the functional group of the carbon pendent to the oxime carbon with increasingly larger alkyl groups or by replacing the terminal halide. The larger alkyl groups cause structural distortions which increased the Mn-N-O-Mn torsion angles of the complexes and resulted in significant changes in the bond geometries of the bridging azides. Asymmetric packing of the ethyl arm of the oximate ligand in complex **3** lead to lower molecular symmetry (C_1). This result changes the selection rules for the spin Hamiltonian and QTM resonances. The spin Hamiltonian for a C_3 symmetric molecule includes the second order axial term DS_z^2 and third order terms such as B^3_4, neither of which are transverse terms. In a C_1 symmetric molecule, terms such as E and B_4^0 and B_4^4 are allowed. The rhombic term E and B_4^4 term are transverse terms which allow quantum tunneling to occur. Instead of tunneling resonances occurring at $|m_s| = 3n$ as in a molecule with C_3 symmetry, QTM resonances in C_1 symmetry occur at all integer values for the system. Although no magnetization hysteresis measurements were performed on complex **3**, it is expected that **3** will have faster tunneling processes than **1** and **2** as a result of the introduction of these operators.

The increase in the torsion angle had the effect of compressing the Mn^{III}-N_{azide}-Mn^{II} bonds on the "top" half of complexes **2** and **3**. Mn^{III}-N_{azide}-Mn^{II} bond angles and bond distances increased in the "bottom" half of the complex. This elongation resulted in an antiferromagnetic contribution from the "lower" Mn^{II} ion in complexes **2** and **3**. As a result of low-lying excited states, good fits of least-squares of reduced magnetization data for complexes **1**-**3** were not obtained. However, the spin ground state obtained by extrapolation to zero K of χ_M'T versus T data is in agreement with those obtained from fits of reduced magnetization.

The effective barrier, U_{eff}, for the three complexes does not change very much even though the spin ground states switch from S = 10 in **1** to S = 7 in **2** and **3**. Although the barrier scales with DS^2, a larger spin ground state does not necessarily lead to slower relaxation. Excited state mixing has been shown to result in faster relaxation behavior in a number of Mn_6 complexes.[21] The larger torsion angles in **2** and **3** should lead to stronger exchange within the central triangle than **1**. The stronger exchange of the triangle might result in a more isolated spin ground state compensating for the smaller spin ground states.

In conclusion, a series of three molecules were synthesized in which the Mn-N-O-Mn torsion angle was systematically increased by varying the oximate ligand. This had the effect of distorting the bond geometry of the bridging azides such that with the increase in torsion angle, there was a resulting antiferromagnetic contribution from one of the Mn^{II} ions. This resulted in a lower spin ground state in complexes **2** and **3** than in complex **1**. The increased torsion angles in **2** and **3** resulted in stronger ferromagnetic exchange within the central triangle, leading to more isolated spin ground states. This resulted in a U_{eff} for complexes **2** and **3** that were comparable to **1** even though they had smaller spin ground states.

References

1. Sessoli, R.; Gatteschi, D.; Caneschi, A.; Novak, M. A., Magnetic Bistability in a Metal-Ion Cluster. *Nature* **1993,** 365, (6442), 141-143.

2. Christou, G.; Gatteschi, D.; Hendrickson, D. N.; Sessoli, R., Single-molecule magnets. *Mrs Bulletin* **2000,** 25, (11), 66-71

3. del Barco, E.; Kent, A. D.; Hill, S.; North, J. M.; Dalal, N. S.; Rumberger, E. M.; Hendrickson, D. N.; Chakov, N.; Christou, G., Magnetic quantum tunneling in the single-

molecule magnet Mn-12-acetate. *Journal of Low Temperature Physics* **2005,** 140, (1-2), 119-174.

4 del Barco, E.; Kent, A. D.; Rumberger, E. M.; Hendrickson, D. N.; Christou, G., Symmetry of magnetic quantum tunneling in single molecule magnet Mn-12-acetate. *Physical Review Letters* **2003,** 91, (4).

5. Chudnovsky, E. M., Quantum hysteresis in molecular magnets. *Science* **1996,** 274, (5289), 938-939.

6. Miyasaka, M.; Clèrac, R.; Wernsdorfer, W.; Lecren, L.; Bonhomme, C.; Sugiura, K.; A., A Dimeric Manganese(III) Tetradentate Schiff Base Complex as a Single-Molecule Magnet, *Angewandte Chemie International Edition,* **2004**, *43*, 2801.

7. Tasiopoulos, T. J.; Vinslava, A.; Wernsdorfer, W.; Abboud, K. A.; Christou, G. Giant single-molecule magnets: A {Mn-84} torus and its supramolecular nanotubes, *Angewandte Chemie International Edition.* **2004**, *43*, 2117.

8. Aubin, S. M.; Sun, Z. M.; Pardi, L.; krzystek, J.; Folting, K.; Brunel, L. C.; Rheingold, A. L.; Christou, G.; Hendrickson, D. N., Reduced anionic Mn-12 molecules with half-integer ground states as single-molecule magnets. *Inorganic Chemistry,* **1999**, 23, 5329-5340.

9. Yang, E. C.; Wernsdorfer, W.; Hill, S.; Edwards, R. S.; Nakano, M.; Maccagnano, S.; Zakharov, L. N.; Rheingold, A. L.; Christou, G.; Hendrickson, D. N., Exchange bias in Ni4 single-molecule magnets, *Polyhedron*, **2003**, 22, 1727-1733.

10. Christou, G., Single-molecule magnets: a molecular approach to nanoscale magnetic materials, *Polyhedron,* **2005**, 24, 2065-2075.

11. Stamatatos, T. C.; Foguet-Albiol, D.; Stoumpos, C. C.; Raptopoulou, C. P.; Terzis, A.; Wernsdorfer, W.; Perlepes, S. P.; Christou, G.; Initial Example of a Triangular Single-Molecule Magnet from Ligand Induced Structural Distortion of a [MnIII3O]7+ Complex, *Journal of the American Chemical Society*, **2005**, 127, 15380-15381.

12. Stamatatos, T. C.; Foguet-Albiol, D.; Lee, S. C.; Stoumpos, C. C.; Raptopoulou, C. P.; Terzis, A.; Wernsdorfer, W.; Hill, S. O.; Perlepes, S. P.; Christou, G. "Switching on" the Properties of Single-Molecule Magnetism in Triangular Manganese(III) Complexes, *Journal of the American Chemical Society,* **2007**, *129*, 9484–9499.

13. Cano, J.; Cauchy, T.; Ruiz, E.; Constantinos, J M; Constantinos, C.; Stoumpos, C.; Stamatatos, C.; Spyros, P. P.; Christou, G.; Brechin, B. K. On the origin of ferromagnetism in oximato-based [Mn3O]7+ triangles. *Dalton* **2008** 234-240.

14. Milios, C. J.; Piligkos, S.; Brechin, E. K. Ground state spin-switching via targeted structural distorsion: twisted single-molecule magnets from derivatised salicyaldoximes *Dalton* **2008**, 1809-1817.

15. C. J. Milios, A. Vinslava, Wernsdorfer, W.; Moggach, S.; Parsons, S.; Perlepes, S. P.; Ghristou, G.; Brechin, E. K. A record anisotropy barrier for a single-molecule magnet *Journal of the American Chemical Society* **2007** 129, 10, 2754-2755.

16. Yang, C. I.; Wernsdorfer, W.; Lee, G. H.; Tsai, H. L. A pentanuclear manganese single-molecule magnet with large anisotropy. *Journal of the American Chemical Society*, **2007**, 129, 455-457.

17. Stokker, G. PREPARATION OF 1,2-BENZISOXAZOLES FROM SALICYLALDOXIMES VIA TRICHLOROACETYL ISOCYANATE, *Journal of Organic Chemistry* **1983**, *48*, 2613–2615.

18. Carlin, R. L., *Magnetochemistry*. Springer-Verlag: New York, 1986.

19. Zeng, Y. F.; Hu, X.; Liu, F. C.; Bu, X. H. Azido-mediated systems showing different magnetic behaviors. *Chemical Society Reviews*, **2009**, 38, 469-480.

20. Stamatatos, T. C.; Christou, G. Azide Groups in Higher Oxidation State Manganese Chemistry: From Structural Aesthetics to Single-Molecule Magnets. *Inorganic Chemistry*, **2009**, 48, 8, 3308-3322.

21. Carretta, S.; Guidi, T.; Santini,P.; Ameretti, G.; Pieper, O.; Lake, B.; van Slageren, J.; El Hallak, F.; Wernsdorfer, W.; Mutka, H.; Russian, M.; Milios, C. J.; Brechin, E. K., Breakdown of the Giant Spin Model in the Magnetic Relaxation of Mn6 Nanomagnets, *Physical Review Letters*, **2008**, 100, 157203.

Chapter Three

"Double-Decker" $[NX_4]_2[Mn_8(salox)_6O_2(N_3)_6(MeOH)_2]$ Single-Molecule Magnets

3.1 Introduction

Single-molecule mangets (SMM) represent the confluence between quantum and classical behavior. Since the discovery of quantum behavior in the first single-molecule magnet (SMM), $[Mn_{12}O_{12}(CH_3COOH)_{16}(H_2O)_4]\bullet 2CH_3COOH\bullet 4H_2O$, "$Mn_{12}Ac$" in 1993, they have been the center of intense study.[1-4] SMMs have an energy barrier to the reversal of magnetization between spin up and spin down states which is given by $|D|S_z^2$ in integer systems and $|D|(S_z^2 - 1/4)$ in half-integer systems. This barrier gives rise to relaxation responses in ac susceptibility measurements and hysteresis loops in magnetization versus applied field sweeps. SMMs are monodisperse, meaning they are uniform in size, shape, and magnetic properties. This uniformity enables the study of unique quantum effects such as quantum tunneling of magnetization, thermally assisted tunneling, quantum phase interference, and spin parity effects.[5-9]

The assembly of zero dimensional materials into multidimensional materials, especially those that behave as single-chain magnets (SCM), has led to the observance of new physics and has provided an exciting challenge for the synthetic chemist.[10, 11] A SCM is an assembly of building blocks that are either SMMs or simple paramagnetic units that function as individual magnetic units.[10] There is an exchange interaction between the building blocks which gives rise to the collective nature of the chain. Ideally the spins of each building block would be aligned along the entire length of the chain. However, relaxation pathways, crystallographic defects, and intermolecular interactions can all result in antiparallel spins in neighboring units. This results in a finite segment of

aligned spins which is referred to as the correlation length.[10] The length depends on crystallographic defects and intermoleculear interactions unique to each system.

Relaxation dynamics are also different in SCMs. Because the building blocks are magnetically coupled, it takes additional energy for spin reversal to take place that is dependent on the strength of the coupling between building blocks.[10] This leads to the longer relaxation times observed in SCMs compared to those observed for SMMs. Therefore, is imperative to construct SCMs with the strongest possible exchange between building blocks in order to maximize the barrier to reversal of magnetization. If the coupling between units is weak, the chain will behave as a coordination polymer built of SMMs.

The first SCMs were assembled from simple, sterically isolated mononuclear or dinuclear systems that were interconnected through short bridging ligands. The first reported SCM consists of ferromagnetically coupled S = 3 $Mn_2(saltman)_2$ $Ni(pao)_2(pyr)_2$ units where saltman is N,N'-(1,1,2,2-tetramethylethylene) bis-(salicylideneiminate); pao is pyridine-2-aldoximate; and pyr is pyridine.[12] The chains were magnetically isolated with bulk counter-ions and had a correlation length of 110 units (~140 nm). Another strategy in the synthesis of chain magnets is to assemble chains of known SMMs using bridging ligands. Chain magnets have been formed in this manner include a Mn_4 cubane with bridging chlorides[13] and an azide bridged Mn_4 chain magnet.[14]

Oxime stabilized Mn_3^{III} triangles are ideal building blocks for larger topologies and extended systems as they possess reasonable spin and have the potential for large axial anisotropy. The factors governing magnetic exchange interactions within μ_3-O^{2-} centered Mn_3^{III} triangles stabilized by tridentate oximate ligands have been the focus of

much attention recently.[15-18] Through magneto-structural correlations in Mn_3^{III} triangles, it has been discovered that net ferromagnetic exchange interactions within the triangles increase with increasing Mn-N-O-Mn torsion angle involving the oximate bridging ligand.[17] A turnover angle in the Mn-N-O-Mn torsion angle has been correlated with the sign of magnetic exchange between Mn ions. Torsion angles less than 31^o lead to antiferromagnetic exchange while angles greater than approximately 32^o lead to ferromagnetic exchange.[17]

The record barrier (U_{eff}) to reversal of magnetization was recently reported in a complex composed of two off-set $[Mn_3^{III}–(\mu_3\text{-oxo})]^{+7}$ triangles related by an inversion center with the formula $[Mn_6O_2(Et\text{-salox})_6(O_2CPh(Me)_2)_2(EtOH)_6]$ where et-salox is 2-hydroxyphenylpropanone oxime. The large U_{eff} (86.4 K) is reflective of the large axial anisotropy and S = 12 ground state.[18] The $[Mn^{III}_6(\mu_3\text{-}O^{2-})_2(\mu_3\text{-OR})_2]^{+12}$ core provides an ideal building block in and of itself. In the above complex the axial coordination sites of the Mn^{III} ions were occupied by carboxylate ligands or solvent. It was realized that coupling high spin Mn^{II} ions to these sites, an even higher anisotropy barrier could be achieved.

Complexes with a $Mn_2^{II}Mn_6^{III}$ magnetic core was formed by bridging two Mn^{II} ions through end-on azides.[21] The complexes are of the formula $[Mn_8(X)_6O_2(N_3)_6(MeOH)_8]\bullet 10MeOH$, where X = nap-salox (2-hydroxynapthaldoxime) or Me-salox (2-hydroxyphenylethanone oxime). Three axially coordinated $\mu_2–\eta^1\text{:}\eta^1$ azides coordinated to the Mn^{III} Jahn-Teller axis of the Mn_3^{III} ions and bridged an octahedrally coordinated Mn^{II} ion with three methanols filling out its coordination sphere. The Mn-N-O-Mn torsion angle increases from an average of 30^o in the nap-salox

analogue to 40^{o} in the Me-salox analogue. The increase in the torsion angle switches the magnetic exchange within the central triangles from antiferromagnetic in the Nap-salox analogue to ferromagnetic in the Me-salox analogue. However, exchange through the end-on bridging azides was antiferromagnetic in both complexes resulting in spin ground states of S =1 in the nap-salox analogue and S = 7 in the Me-salox analgoue.[20] The antiferromagnetic exchange was the result of the large angles of the end-on azides, which averaged to ~120^{o}. The azide bridging angles have to be restrained if they are to mediate ferromagnetic exchange.

In chapter II of this thesis it was shown that complexes of the formula $[NEt_4]_3[Mn_5(R\text{-salox})_3O(N_3)_6X_2]$ demonstrate that Mn^{II} ions could be ferromagnetically coupled to a Mn_3^{III} triangle through end-on azides. The smaller angles of the end-on bridging azides were achieved by stabilizing a tetrahedral coordination environment in the Mn^{II} ions. The counter-ions provide some versatility as they could be changed with increasingly larger cations in order to induce structural distortions through crystal packing effects.

Two complexes of the formula $[X]_2[Mn_8(salox)_6O_2(N_3)_6(MeOH)_2Cl_2] \bullet 2slov$, where X^+ is either NPr_4^+ or NBu_4^+ and solv is either MeOH or $CHCl_3$, have been synthesized in the present research described in this chapter with identical $Mn_2^{II}Mn_6^{III}$ magnetic cores. Structural and geometric distortions were induced by varying the cocrystallizing counter-ion and solvent. Solvent was changed from methanol in **1** to chloroform in **2**. These structural changes induced by crystal packing lead to differences in magnetic behavior between the two complexes. The $Mn_2^{II}Mn_6^{III}$ magnetic core forms the building block for a one-dimensional azide bridged coordination polymer of the

formula $[NEt_4]_2[Mn_8(salox)_6O_2(N_3)_8(MeOH)_3]_\infty$• MeOH, **3**. Complex **3** did not exhibit any evidence of SCM behavior in the temperature range studied.

3.2 Experimental Section

3.2.1 Compound Synthesis

All procedures were carried out under aerobic conditions. Reagents were used as received. **Caution!** Azide salts are highly toxic and potentially explosive. Although no problems were encountered in this work, they should be prepared in small quantities and handled with care.

$[NBu_4]_2[Mn_8O_2(salox)_6(N_3)_6(MeOH)_2Cl_2]$•2MeOH (1). $MnCl_2{\cdot}4H_2O$ (197 mg, 1.00 mmol) was dissolved in a 1:2 solution of methanol and dichloromethane (20 mL). NaN_3 (68 mg, 1.0 mmol) and H_2salox (137 mg, 1.0 mmol) were added consecutively. The dark green solution was stirred for 15 minutes before 0.5 mL of a 40% aqueous solution of tetrabutylammonium hydroxide was added drop-wise. The dark green solution was stirred for one hour before being gravity filtered. A vapor diffusion on the filtrate with diethyl ether resulted in large dark brown blocks forming in three weeks in 14% yield (based on Mn). Select IR: 3427 cm^{-1} (b), 2960 cm^{-1} (m), 2076 cm^{-1} (s), 1597 cm^{-1} (m), 1283 cm^{-1} (m), 1030 cm^{-1} (m), 677 cm^{-1} (m). Elemental Analysis calculated: 34.84 %C 4.18 %H 17.72 %N. Experimental: 35.99 %C 4.18 %H 5.73 %N.

$[NPr_4]_2[Mn_8O_2(salox)_6(N_3)_6(MeOH)_2Cl_2]$•2$CHCl_3$ (2). $MnCl_2{\cdot}4H_2O$ (197 mg, 1.00 mmol) was dissolved in a 1:2 solution of methanol and dichloromethane (20 mL). NaN_3 (68 mg, 1.0 mmol) and H_2salox (137 mg, 1.0 mmol) were added consecutively. The dark green solution was stirred for 15 minutes before 1.0 mL of a 1.0 M aqueous

solution of tetrapropylammonium hydroxide was added drop-wise. The dark green solution was stirred for 90 minutes before being gravity filtered. A vapor diffusion on the filtrate with diethyl ether resulted in thin dark brown needles forming over 2 weeks in 30% yield (based on Mn). Select IR: 3423 cm^{-1} (b), 2971 cm^{-1} (w), 2075 cm^{-1} (s), 1596 cm^{-1} (s), 1438 cm^{-1} (m), 1283 cm^{-1} (m), 673 cm^{-1} (m). Elemental Analysis calculated: 36.86 %C 4.24 %H 15.96 %N. Experimental: 42.15 %C 6.22 %H 6.29 %N.

$[NEt_4]_2[Mn_8O_2(salox)_6(N_3)_8(MeOH)_2]_\infty$•2MeOH (3). $Mn(NO_3)_2{\cdot}4H_2O$ (257 mg, 1.00 mmol) was dissolved in methanol (40 mL). NaN_3 (68 mg, 1.0 mmol) and H_2salox (137 mg, 1.0 mmol) were added consecutively. The dark green solution was stirred for 15 minutes before 0.8 mL of a 20% aqueous solution of tetraethylammonium hydroxide was added drop-wise. The dark green solution was stirred for an additional one hour before being gravity filtered. A vapor diffusion on the filtrate with diethyl ether resulted in large dark brown blocks forming in 3 days. The crystals were washed with Et_2O and collected in 80% yield (based on Mn). Select IR: 3443 cm^{-1} (b), 2071 cm^{-1} (s), 1596 cm^{-1} (m), 1439 cm^{-1} (m), 1028 cm^{-1} (m), 678 cm^{-1} (m). Elemental Analysis calculated: 34.84%C 4.12 %H 24.53 %N. Experimental: 34.64 %C 4.12 %H 22.44 %N.

3.2.2 X-ray Crystallography

Diffraction data were collected using a Bruker Smart Apex CCD diffractometer at 100 K. The data were integrated using the Bruker SAINT software program and scaled using the SADABS software program. Complexes were solved by direct methods (SHELXL-97), developed by successive difference Fourier syntheses, and refined by full-matrix least-squares on all F^2 data. All non-hydrogen atoms were refined anisotropically by full-matrix least-squares (SHELXL-97). All hydrogen atoms were placed using a

riding model. Their positions were constrained relative to their parent atom using the appropriate HFIX command in SHELXL-97.

For complex **1**, solvate and two disordered n-$[NBu_4]^+$ groups were treated with the PLATON program SQUEEZE. The electron density accounted for the two disordered $[NBu_4]^+$ groups and two methanols.

3.2.3 Magnetic Studies

Variable temperature dc and ac magnetic susceptibility data were collected on well ground polycrystalline samples restrained in eicosane to prevent torquing of the sample in the magnetic field. Dc magnetic susceptibility measurements were performed on a Quantum Design MPMS-5 SQUID magnetometer equipped with a 5.5 T magnet in a temperature range of 300-1.8 K in magnetic fields ranging from 0.01 to 5.0 T. AC magnetic susceptibility data were collected in a 3 Oe ac field from 10-997 Hz in zero applied dc field in a temperature range of 1.8-7.0 K. The measurements were performed using a Quantum Design MPMS-2 SQUID magnetometer equipped with a 3 T magnet. Diamagnetic corrections were estimated from Pascal's constants[21] and subtracted from the experimental susceptibility data to obtain the molar paramagnetic susceptibility of the compounds.

3.2.4 Other Physical Measurements

Elemental analysis data were performed by Numega Resonance Laboratories (San Diego, CA). IR spectra were collected samples on powder samples in a KBr pellet on a Thermo-Nicolet Avatar 360 spectrophotometer in a range of 400-4000 cm^{-1}.

3.3 Results and Discussion

3.3.1 Discussion of Synthesis

Complexes **1** and **2** were synthesized from the addition of reagents to a 1:2 solution of methanol and chloroform. Complex **3** was synthesized by the sequential addition of reagents to a methanolic solution. Mixed solvents were used to inhibit the formation of side products and ensure slow crystal growth of the products. All complexes were crystallized by vapor diffusion of diethyl ether into the mother liquor. The solvent and counter-ions that co-crystallize with complexes **1** and **2** have been changed in an attempt to induce structural distortions through crystal packing effects and to reduce intermolecular interactions by weakening hydrogen bonding pathways.

A common synthetic strategy in SMM chemistry is to use a complex as starting material and perform methasis type reactions with other ligands to form new complexes. In the synthesis of **3**, the $Mn_2^{II}Mn_6^{III}$ core was formed in situ using manganese nitrate in place of manganese halide salts. The nitrate ion does not coordinate as well as azide so it was hoped that absence of a competing halide would ensure that azide would coordinate to the terminal Mn^{II} ions, forming a one dimensional chain.

The formation of the mixed valent $Mn_2^{II}Mn_6^{III}$ core from Mn^{II} salts involves the oxidation of Mn. Since no oxidizing agents were added to the solution, oxidation must have occurred by the action of atmospheric O_2. The oxidation was accessed by the rapid darkening of the solution following addition of the tetraalkylammonium salt to the solution.

3.3.2 Description of Structures

Crystallographic data and refinement parameters for complexes **1-3** can be found in Table 1. Summarized structural parameters for complexes **1-3** are found in Table 2. ORTEP representation of complex **1** and crystal packing diagrams can be found in Figures 2 and 3, respectively. Complex **1** crystallizes in the triclinic space group P-1. The unit cell contains two crystallographically independent molecules. The $[Mn^{III}_6(\mu_3\text{-}O^{2-})_2(\mu_3\text{-}OR)_2]^{+12}$ core of each molecule consists of two off-set $[Mn_3^{III}\text{–}(\mu_3\text{-oxo})]^{+7}$ triangles related by an inversion center. The triangles are capped by axial, azide bridged Mn^{II} ions. Four of the six Mn^{III} ions have a distorted octahedral coordination environment while two possess square pyramidal geometry with a weak linkage to the apical phenolate oxygen. Within each triangular subunit, the three Mn^{III} ions are bound by a $\mu_3\text{-}O^{2-}$ and three oximate ligands two of which are in a $\mu_2\text{–}\eta^1\text{:}\eta^1\text{:}\eta^1$ bridging mode, and the third in a $\mu_2\text{–}\eta^1\text{:}\eta^1\text{:}\eta^2$ bridging mode where the oximate oxygen is bridging a Mn^{III} ion of the second triangular subunit. Three axially coordinated $\mu_2\text{–}\eta^1\text{:}\eta^1$ azides are coordinated to the Mn^{III} Jahn-Teller axis and bridge a tetrahedrally coordinated Mn^{II} ion that is capped with a terminal chloride. Although there are two symmetry independent molecules per unit cell, the geometries of each molecule are relatively similar and vary by less than 5%. The $\mu_3\text{-}O^{2-}$ bridging atom sits 0.085 Å above the plane formed by the Mn^{III}_3 triangle. The bridging Mn-oximate and Mn-phenolate bond distances are 2.39 Å (Mn1-O3') and 2.701 Å (Mn2-O4'), respectively. The Mn-N-O-Mn torsion angles for each molecule are over $\theta = 25^o$ and range from $\theta = 27.32^o$ to 30.27^o. The $Mn^{III}\text{-}N_3\text{-}Mn^{II}$ angles vary from $\theta = 109.34^o$ to 113.05^o. Two $[NBu_4]^+$ cations maintain charge

Table 1. Crystallographic Data for Complexes **1-3.**

	1	2	3
Empirical formula	C76 H92 Cl2 Mn8 N26 O16	C140 H186 Cl16 Mn16 N52 O32	C62 H81 Mn8 N32 O19
Formula weight	2136.18	4555.65	2018.11
Temperature	100(2) K	100(2) K	100(2) K
Wavelength	0.71073 Å	0.71073 Å	0.71073 Å
Crystal system	Triclinic	Triclinic	Monoclinic
Space group	P-1	P-1	P2(1)/c
Unit cell dimensions	a = 15.2336(15) Å	a = 15.5865(16) Å	a = 13.5597(7) Å
	b = 28.204(3) Å	b = 18.1505(18) Å	b = 24.9220(12) Å
	c = 12.6977(13) Å	c = 18.7301(19) Å	c = 25.0413(12) Å
	α= 90°	α= 115.2310(10)°	α= 90°
	β= 112.946(2)°	β= 93.456(2)°	β= 99.6380(10)°
	γ = 90°	γ = 95.388(2)°	γ = 90°
Volume	5023.9(9) Å^3	4742.4(8) Å^3	7034(7) Å^3
Z	2	1	4
Density (calculated)	1.412 Mg/m^3	1.595 Mg/m^3	1.607 Mg/m^3
Absorption coefficient	1.094 mm^{-1}	1.090 mm^{-1}	1.255 mm^{-1}
F(000)	2184	2318	3104
Crystal color/habit	brown parallelogram	brown needle	brown plate
Theta range for data collection	1.44 to 28.12°	1.31 to 25.42°	1.16 to 28.25°
Reflections collected	50430	67099	138378
Independent reflections	21919 [R(int) = 0.1031]	4153 [R(int) = 0.0401]	19417 [R(int) = 0.0655]
Completeness to theta = 25.00°	98.5 %	99.7 %	100.0 %
Data / restraints / parameters	21919 / 0 / 847	17378 / 0 / 1118	19417 / 0 / 1092
Goodness-of-fit on F^2	0.759	1.094	0.946
Final R indices [I>2sigma(I)]	R1 = 0.0599, wR2 = 0.1160	R1 = 0.0467, wR2 = 0.1187	R1 = 0.0583, wR2 = 0.1332
R indices (all data)	R1 = 0.1501, wR2 = 0.1320	R1 = 0.0585, wR2 = 0.1252	R1 = 0.0763, wR2 = 0.1430
Largest diff. peak and hole	0.606 and -0.531 e.Å^{-3}	3.332 and -1.278 e.Å^{-3}	1.827 and -1.170 e.Å^{-3}

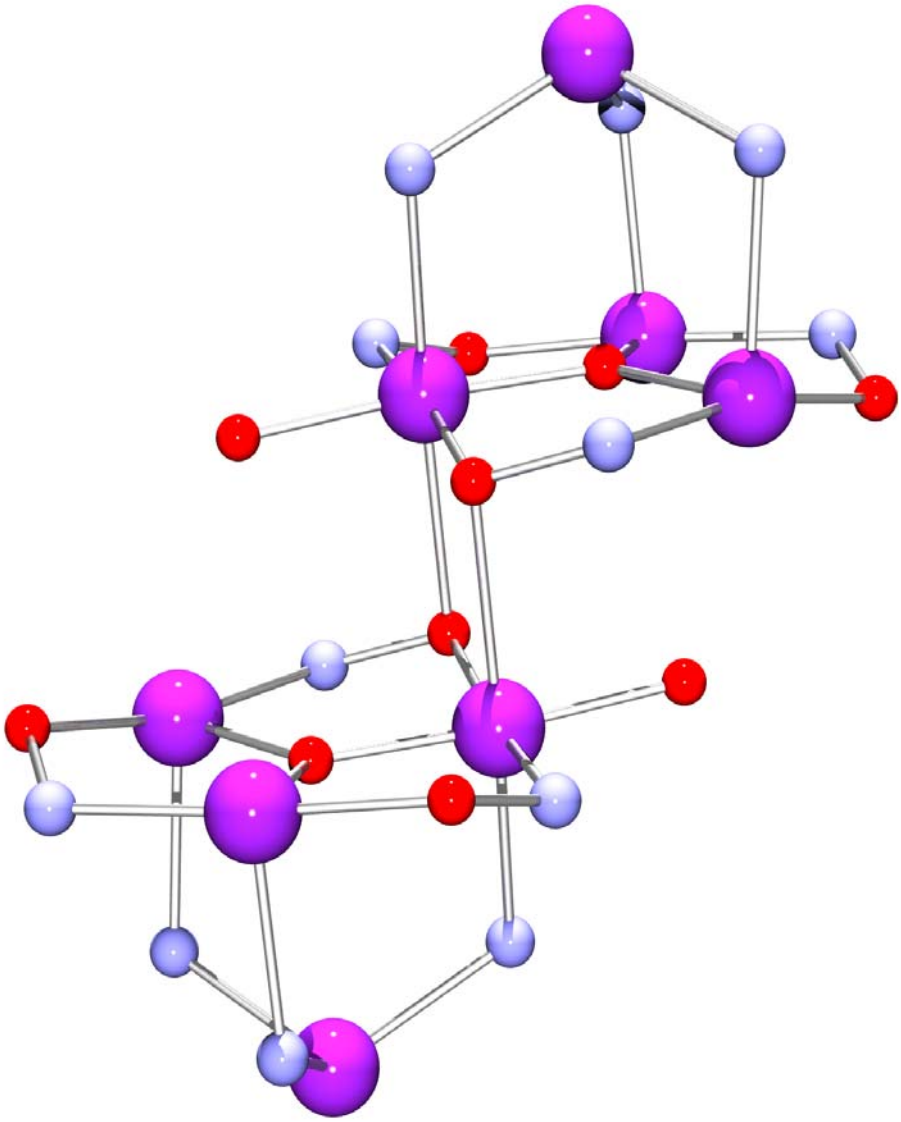

Figure 1. ORTEP of the magnetic core of complexes **1-3** rendered in POV-RAY format. Purple spheres represent manganese atoms, blue spheres represent nitrogen atoms, and red spheres represent oxygen atoms.

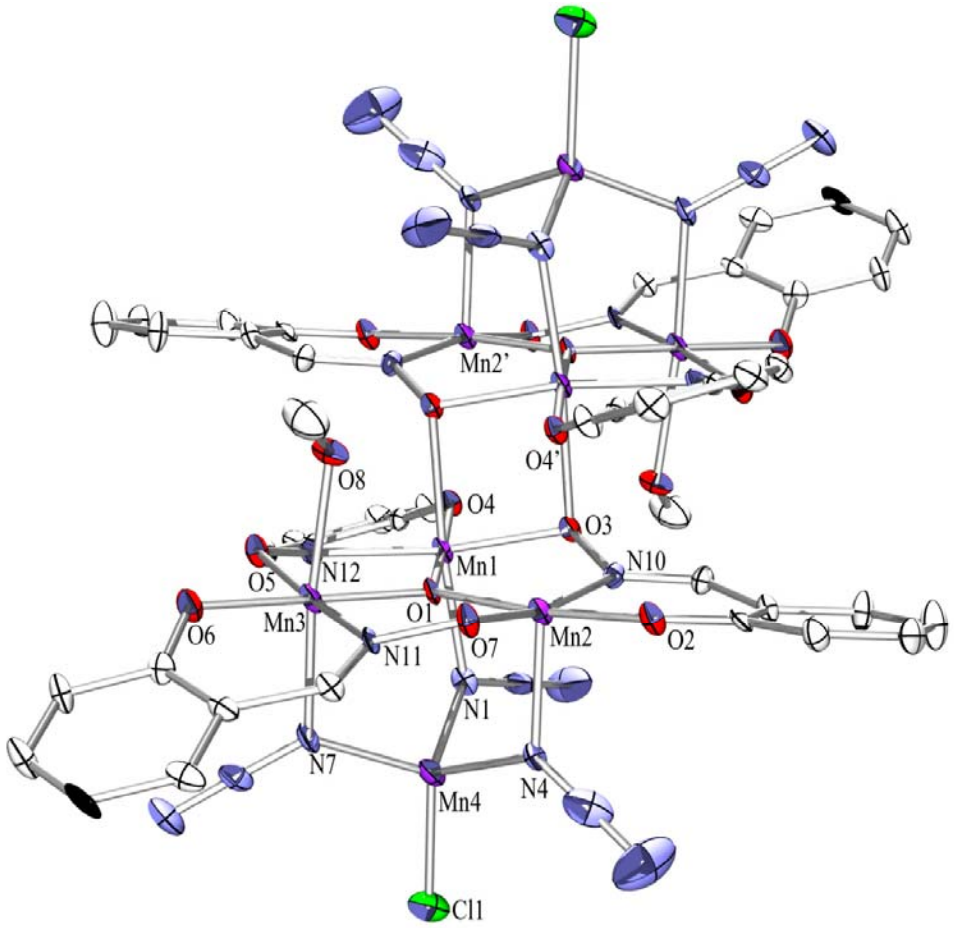

Figure 2. ORTEP of $[NBu_4]_2[Mn_8(salox)_6O_2(N_3)_6(MeOH)_2Cl_2]$ • 2MeOH (**1**) in POV-RAY format with thermal ellipsoids at the 50% probability level. Hydrogen and counter-ion atoms omitted for clarity.

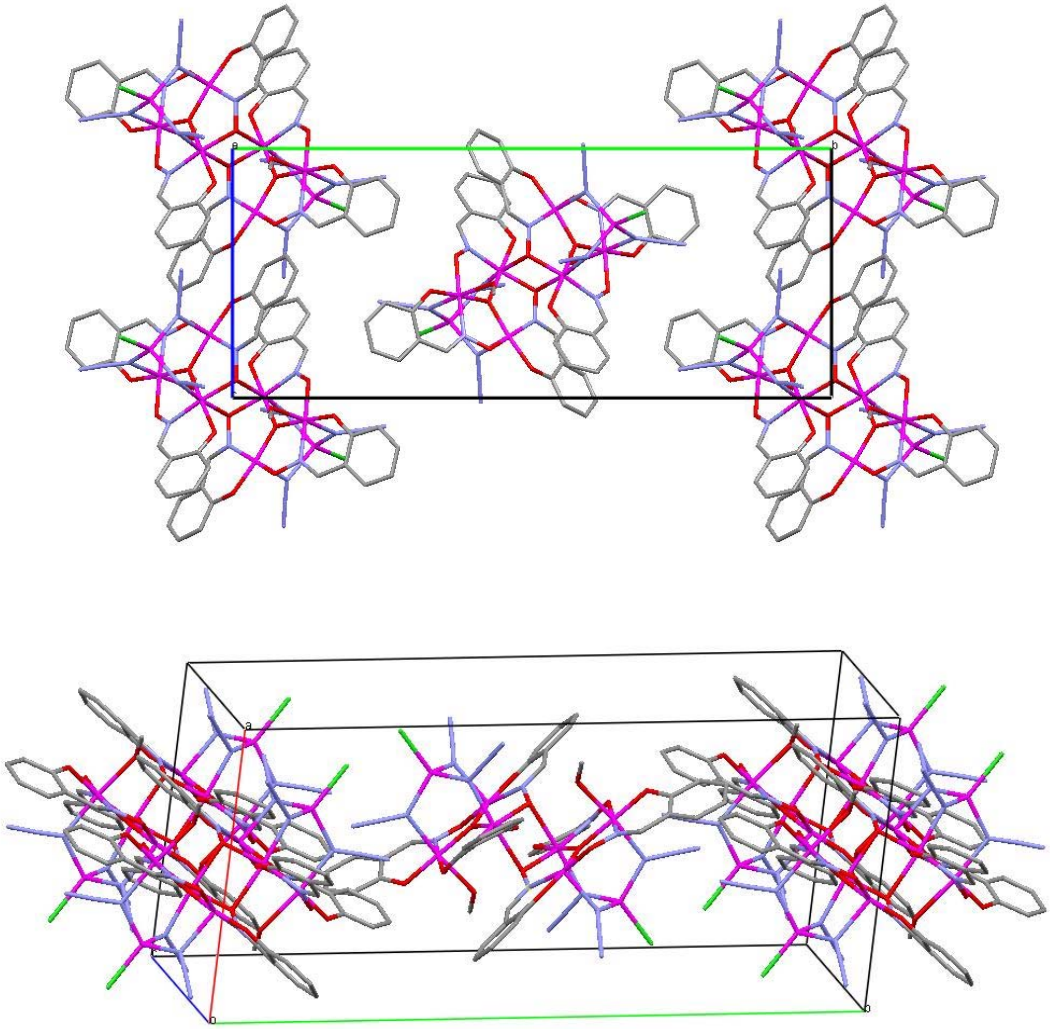

Figure 3. Crystal packing in the bc plane (top) and crystal packing (bottom) of **1**.

balance but are disordered and subsequently needed to be removed with Platon SQUEEZE along with two disordered methanol solvate molecules. The closest intermolecular Mn-Mn contact is 9 Å. Intermolecular hydrogen bonding occurs between the terminal nitrogen of the azides and phenyl protons, with H•••N distances ranging from 2.6 Å to 2.7 Å and is of intermediate strength. H-bonding also occurs between the oximate oxygen and phenyl hydrogens with H•••O distances of approximately 2.7 Å. Crystal packing of complex **1** consists of one symmetry independent molecule located in the center of the unit cell on an inversion center. ¼ of the second molecule is located at each corner of the unit cell.

Complex **2** also crystallizes in the triclinic space group P-1 and is essentially isostructural with complex **1**. An ORTEP representation and crystal packing diagrams of complex **2** can be found in Figures 4 and 5. The two complexes differ only in their co-crystallized solvent and cations. The unit cell contains two crystallographically independent molecules with two $[NPr_4]^+$ cations and two chloroform molecules per complex. The μ_3-O^{2-} sits 0.05 Å out of the Mn^{III}_3 plane. The bridging oximate bond distances are 2.33 Å (O14-Mn5) and 2.66 Å (O9-Mn3), respectively. The Mn-N-O-Mn torsion angles are relatively similar to complex **2** at $\theta = 23.46^o$-32.42^o. Mn^{III}-N_3-Mn^{II} bond angles range from $\theta = 102.6^o$ to 112.7^o. Extensive hydrogen bonding occurs between the terminal nitrogen of the azides and phenyl protons, with H•••N distances ranging from 2.5 Å to 2.7 Å. The chloroform solvate molecules provide another possible pathway for intermolecular interactions. The chloroform chlorides interact with the proton pendant to the oximate carbon with Cl•••H distances of 2.8 Å and 2.9 Å. The

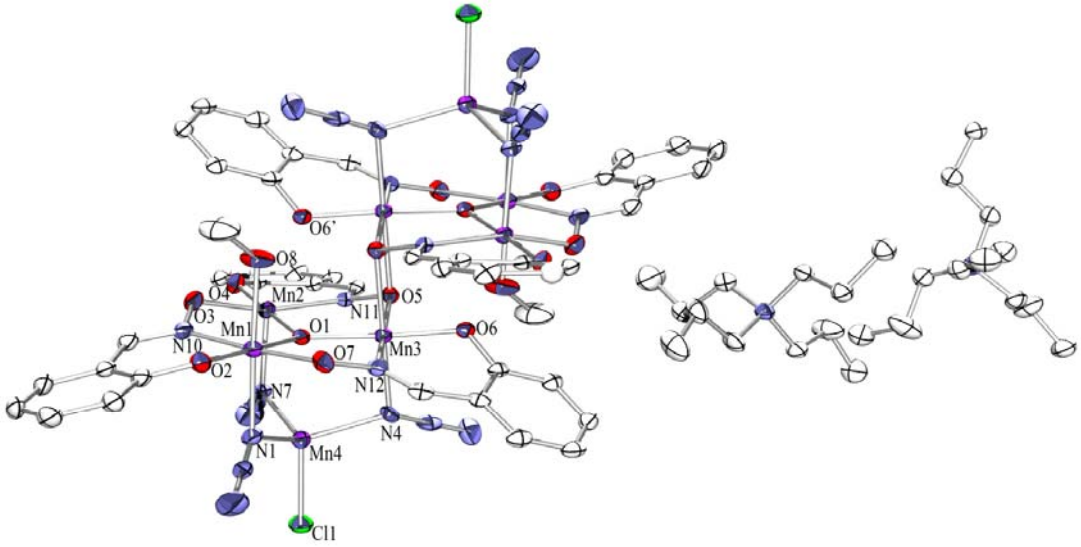

Figure 4. ORTEP of $[NPr_4]_2[Mn_8(salox)_6O_2(N_3)_6(MeOH)_2Cl_2]$ •2$CHCl_3$ (**2**) in POV-RAY format with thermal ellipsoids at the 50% probability level. Hydrogen atoms omitted for clarity.

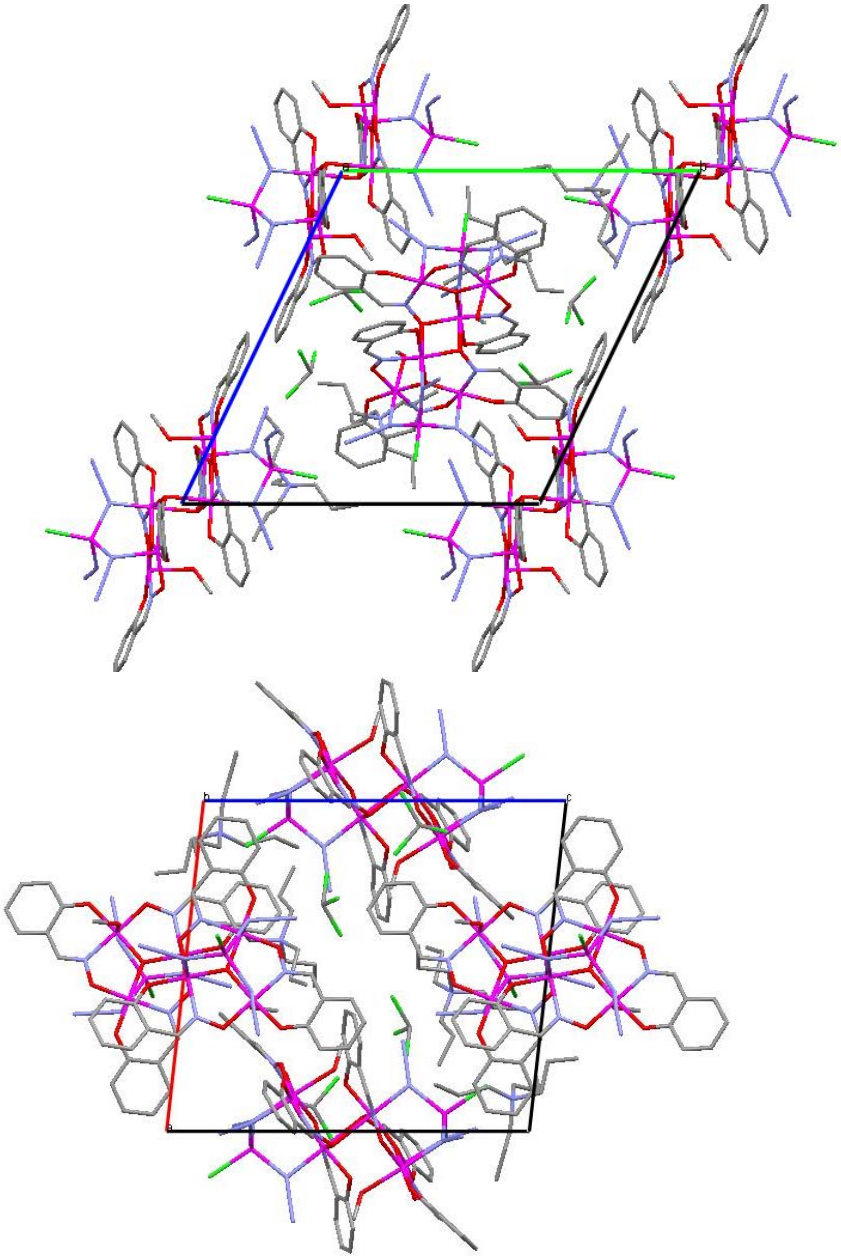

Figure 5. Crystal packing in the ac plane (top) and ab plane (bottom) of **2**.

chloroform protons and the phenolate oxygen also form H-bonds with H•••O distances ranging from 2.7 Å to 2.4 Å. Crystal packing in **2** consists of ½ of a molecule located in the center of the (100) Miller plane. ¼ of the second independent molecule is located at the intersection of the (010) and (001) Miller planes.

An ORTEP representation and crystal packing of complex **3** can be found in Figures 6 and 7. Complex **3** crystallizes in the monoclinic $P2_1/c$ space group and is structurally similar to complexes **1** and **2** in that the core consists of two off-set $[Mn^{III}_3–(\mu_3\text{-oxo})]^{+7}$ triangles capped by axial azide-bridged Mn^{II} ions. However, the complex forms a one-dimensional extended structure by bridging between Mn^{II} ions of adjacent units through two $\mu_2–\eta^1:\eta^1$ azide ligands. The apical Mn^{II} ions have different coordination geometries: Mn(8) possesses a distorted square pyramidal geometry consisting five $\mu–\eta^1:\eta^1$ azides while Mn(4) has a distorted octahedral coordination sphere which is made up of five $\mu_2–\eta^1:\eta^1$ azides and one coordinated methanol. The asymmetric coordination environment results in the loss of the local inversion center, thus are unique bond geometries within each Mn_3 moiety. The bridging Mn-oximate distances, Mn(5)-O(3) and Mn(3)-O(16), are 2.40 Å and 2.51Å, respectively. The Mn-phenolate bond distance, Mn(7)-O(4), is 3.19Å and the two $\mu_3\text{-}O^{2-}$ ions are slightly out of plane by 0.03 Å and 0.04 Å. The $Mn^{III}\text{-}N_3\text{-}Mn^{II}$ bond angles to the five-coordinate Mn^{II} ion are Mn(5)-N(13)-Mn(8), Mn(6)-N(19)- Mn(8), and Mn(7)-N(16)-Mn(8) are (θ = 121.1°, 116.7°, 116.4°), respectively. $Mn^{III}\text{-}N_3\text{-}Mn^{II}$ bridging angles to the six-coordinate Mn^{II} ion, Mn(3)-N(1)-Mn(4), Mn(13)-N(4)-Mn(4), and Mn(2)-N(7)-Mn(4) are close to 120° (θ = 120.58°, 121.74°, 118.05°) whereas the end-on bridging $Mn^{II}\text{-}N_3\text{-}Mn^{II}$ angles,

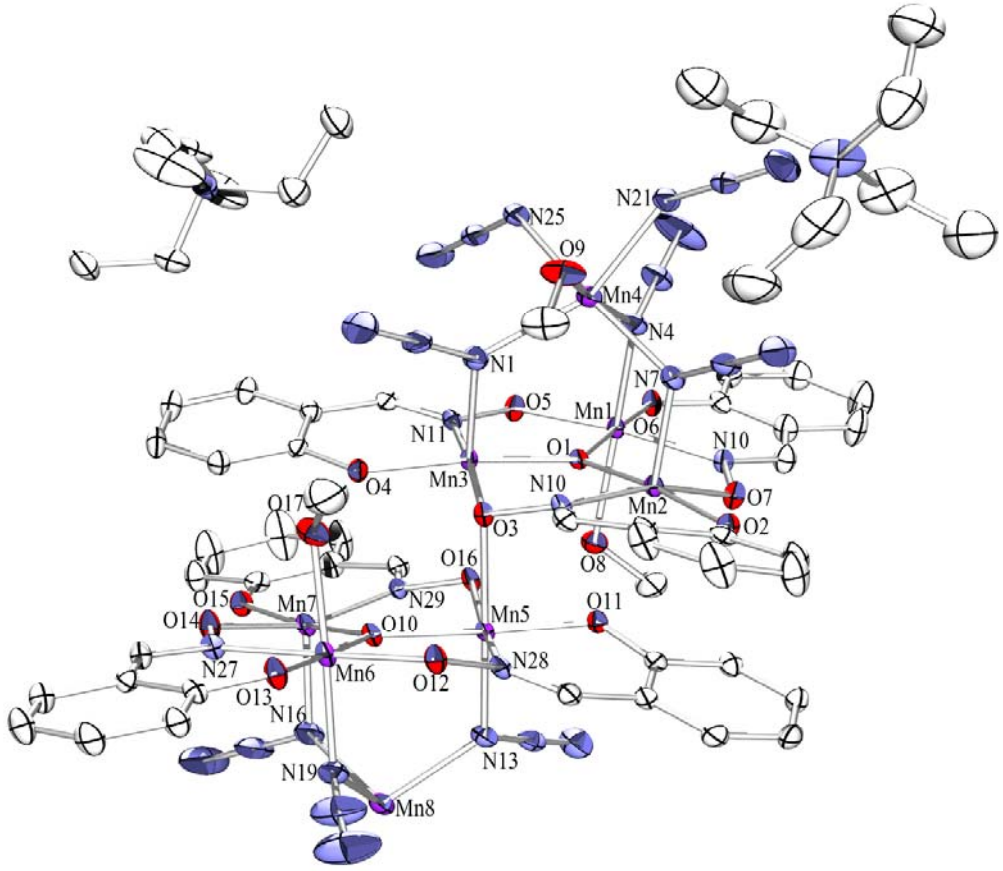

Figure 6. ORTEP of the core of $[NEt_4]_2[Mn_8(salox)_6O_2(N_3)_8(MeOH)_3]_\infty$ •2MeOH (**3**) in POV-RAY format with thermal ellipsoids at the 50% probability level. Hydrogen atoms omitted for clarity.

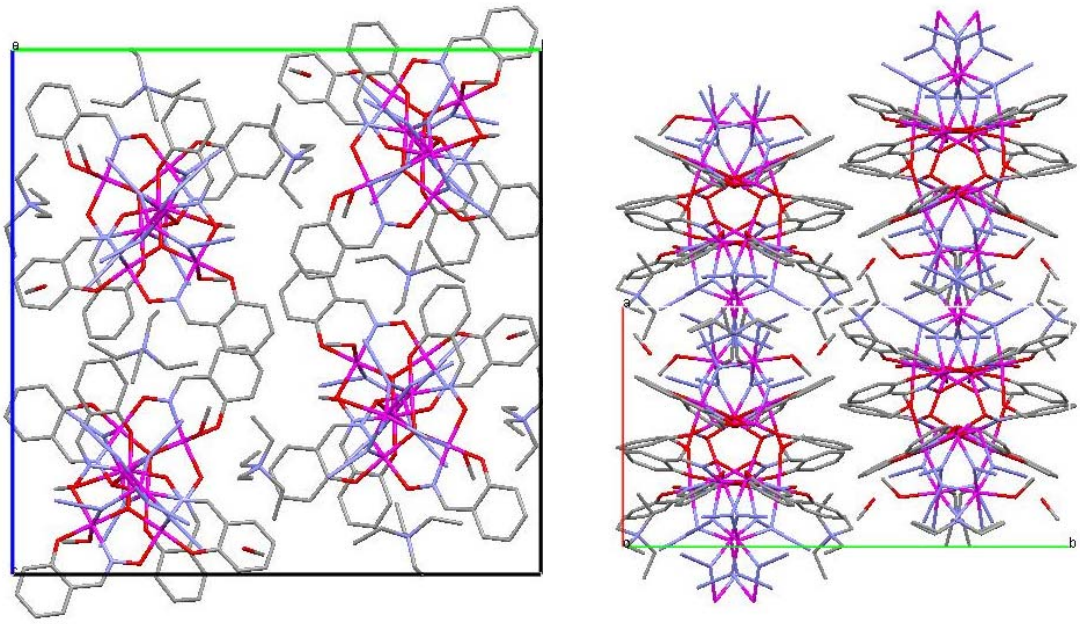

Figure 7. Crystal packing in the bc plane (left) and ab plane (right) of **3**.

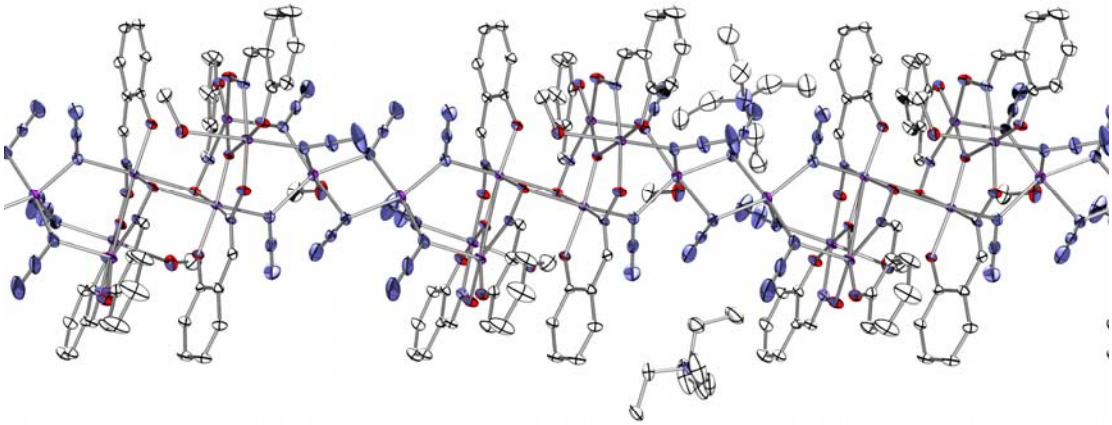

Figure 8. ORTEP of bridging in $[NEt_4]_2[Mn_8(salox)_6O_2(N_3)_8(MeOH)_3]_\infty$•2 MeOH (**3**) in POV-RAY format with thermal ellipsoids at the 50% probability level. Hydrogen atoms omitted for clarity.

Table 2. Select Structural Parameters for Mn_8 Complexes.

Compound	Formula	out of plane μ_3-O^2	Mn-N-O-Mn torsion angle (deg.)	Mn^{III}-N_3-Mn^{II} angle (deg.)	Mn-$O_{phenoxo}$(Å)	Mn-$O_{oximato}$(Å)
1a	$[NBu_4]_2[Mn_8O_2(salox)_6(N_3)_6(MeOH)_2Cl_2]$•2MeOH	0.088	28.8, 25.8, 30.4	108.8, 111.4, 109	2.7	2.38
1b	$[NBu_4]_2[Mn_8O_2(salox)_6(N_3)_6(MeOH)_2Cl_2]$•2MeOH	0.085	30.3 28.7 27.3	113.05, 109.5, 109.3	3.2	2.39
2a	$[NPr_4]_2[Mn_8O_2(salox)_6(N_3)_6(MeOH)_2Cl_2]$•2$CHCl_3$	0.05	30.9, 32.5, 23.2	112.6, 101, 105.5	2.8	2.36
2b	$[NPr_4]_2[Mn_8O_2(salox)_6(N_3)_6(MeOH)_2Cl_2]$•2$CHCl_3$	0.155	23.5, 31.3, 32.2	102.6, 107.3, 106.3	2.6	2.33
3	$[NEt_4]_2[Mn_8O_2(salox)_6(N_3)_8(MeOH)_2]_\infty$•2MeOH	0.04 0.034	17.0, 0.2, 31.5 19.8, 13.8, 26.6	120	2.8 3.2	2.4 2.5

Mn(4)-N(22)-Mn(8) and Mn(4)-N(25)-Mn(8), are 103.0° and 103.7°, respectively. The Mn-N-O-Mn torsion angles vary widely ranging from a minimum of -0.23° to a maximum of 31.46°. The chains pack parallel to the a-axis and are separated by two $[NEt_4]^+$ cations per complex. The cations provide little isolation as the closest interchain contact is 3.17 Å.

3.3.3 DC Magnetic Susceptibility

Bulk dc magnetic susceptibility measurements were made on polycrystalline samples of complexes **1**-**3** in magnetic field strengths of 0.01, 0.1, and 1.0 T in the temperature range of 300-1.8 K. The samples were restrained in eicosane to prevent torqing in the applied field. Plots of the product of molar susceptibility and the temperature ($\chi_m T$) versus temperature for complexes **1**-**3** are shown in Figures 9-11

There are two structurally independent molecules in the unit cell of complex **1**. Bulk susceptibility measurements give the average of the magnetic properties of the two structures. For complex **1**, $\chi_m T$ vs. T in a 0.01 T field is 25.65 cm^3 mol^{-1} K at 300 K. This value is close to the spin only formula of 26.75 cm^3 mol^{-1} K for a non-interacting high spin Mn^{II}_2 Mn^{III}_6 complex with g = 2.0. Magnetization was fairly constant, decreasing only slightly with decreasing temperature until about 50 K, at which point it begins to decrease rapidly to a minimum value of 9.4 cm^3 mol^{-1} K at 1.8 K. Complex **1** exhibits similar behavior at fields of 0.1 and 1.0 T. At 300 K $\chi_M T$ is 26.20 cm^3 mol^{-1} K and 26.14 cm^3 mol^{-1} K for fields of 0.1 and 1.0 T, respectively. $\chi_M T$ then decreases very

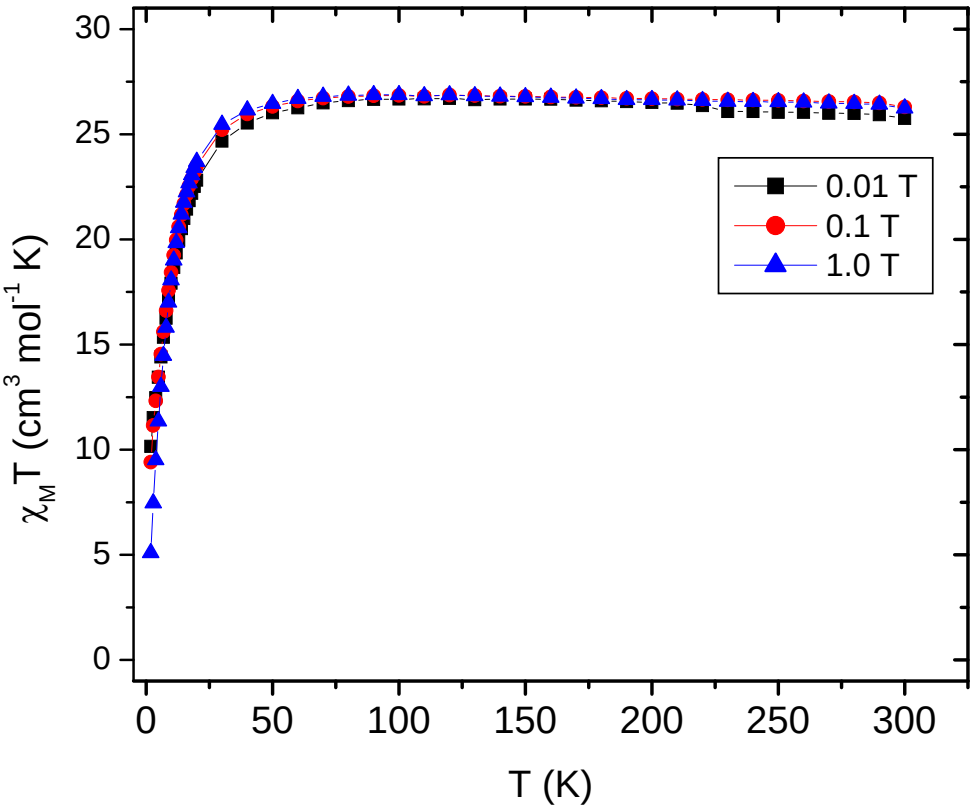

Figure 9. Plot of DC magnetic susceptibility of $[NBu_4]_2[Mn_8(salox)_6O_2(N_3)_6(MeOH)_2Cl_2] \bullet 2MeOH$ (**1**).

slightly with decreasing temperature to 50 K. Below 50 K, $\chi_M T$ decreases more rapidly to values of 9.38 cm^3 mol^{-1} K and 5.08 cm^3 mol^{-1} K for fields of 0.1 and 1.0 T, respectively. The low temperature magnetic behavior is consistent with competing ferromagnetic and antiferromagnetic interactions. The torsion angles of the two structurally independent molecules in complex **1** range from 27.32° to 30.27°. Torsion angles within that range might result in weak antiferromagnetic exchange between Mn^{III} ions. Exchange interactions between Mn^{III} and Mn^{II} ions are mediated by three μ_2:η^1,η^1-azides. The Mn-N_{azide}-Mn bond angle and the Mn-N_{azide} bonds distances determine the nature of the magnetic exchange through bridging azides.[23] The Mn^{III}-N_{azide}-Mn^{II} bond angles of the two different complexes in **1** range from 108.9° to 113.4°. If the exchange through the azides is similar to the Mn_5 "single-decker" complexes reported earlier in this work, the range of bond angles is on the borderline of ferromagnetic/antiferromagnetic exchange interactions. The Mn^{III}-N_{azide} bond distances are all reasonably short, less than 2.24 Å. These bond distances are shorter than those of the "single-decker" complexes which would suggest stronger exchange due to greater overlap between orbitals.

Complex **2** also crystallizes with two structurally independent molecules. Bulk susceptibility measurements represent the average of the two complexes magnetic behavior. The plot of $\chi_m T$ vs. T for complex **2** indicates weak ferromagnetic behavior. $\chi_m T$ for complex **2** in a 0.01 T field begins at 23.59 cm^3 mol^{-1} K at 300 K. The $\chi_m T$ at 300 K is slightly less than the spin only value of 26.75 cm^3 mol^{-1} K for high-spin Mn^{II}_2

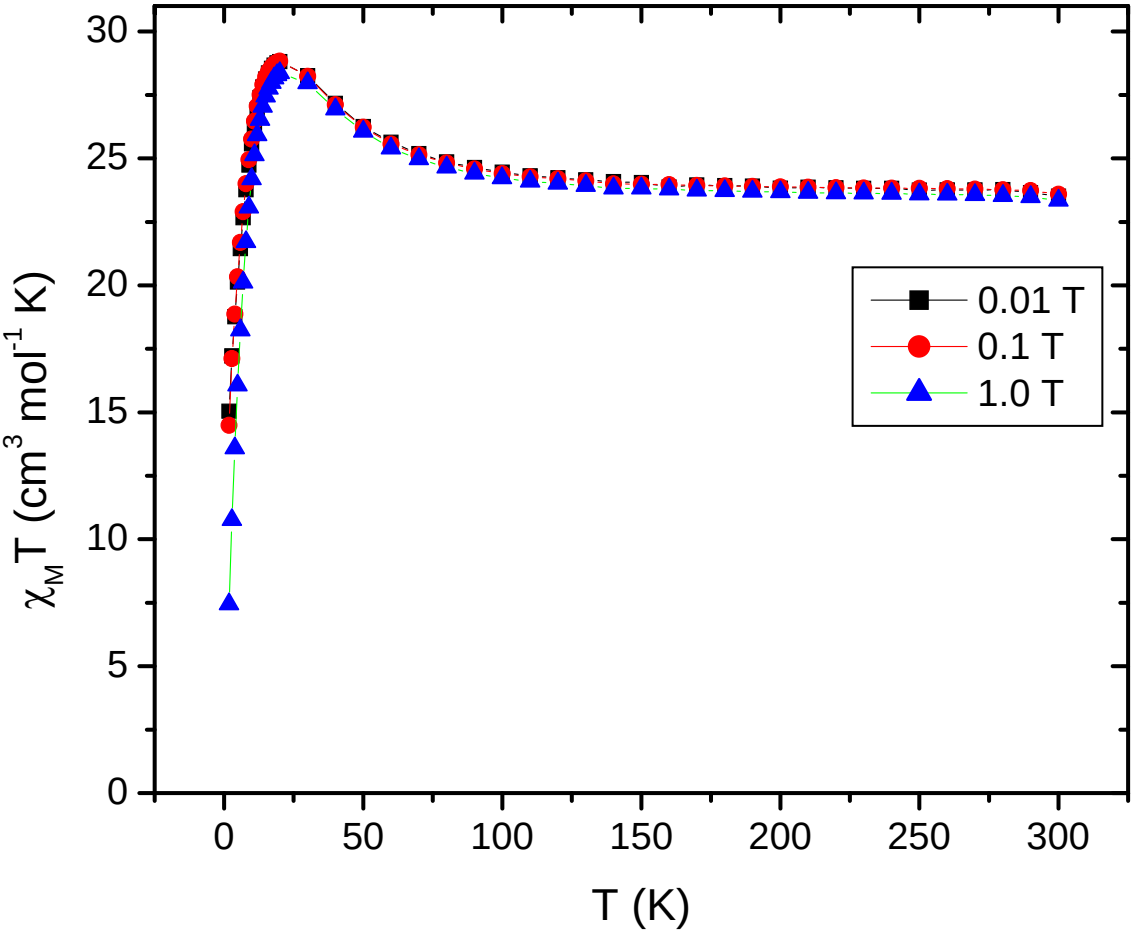

Figure 10. Plot of DC magnetic susceptibility of $[NPr_4]_2[Mn_8(salox)_6O_2(N_3)_6(MeOH)_2Cl_2] \bullet 2CHCl_3$ (**2**).

Mn^{III}_6 ions. χ_mT remains almost constant, slowly increasing until it reaches 100 K. Below 100 K, χ_mT increases more rapidly to a maximum value of 28.8 cm^3 mol^{-1} K at 20 K. χ_mT then decreases rapidly to at value of 15.04 cm^3 mol^{-1} K at 1.8 K. χ_mT vs. T behavior for complex **2** in fields of 1.0 and 0.01 T follows the same trend as a 0.01 T field. For complex **2** in a 0.1 T field, χ_mT vs. T begins at 23.59 cm^3 mol^{-1} K at 300 K and slowly increases until approximately 100 K. Below 100 K, χ_mT increases more rapidly to a maximum 28.37 cm^3 mol^{-1} K at 20 K before decreasing to a minimum of 14.49 cm^3 mol^{-1} K at 1.8 K. χ_mT for complex **2** in a 1.0 T begins at 23.34 cm^3 mol^{-1} K, increase to a maximum of 28.37 cm^3 mol^{-1} K at 20 K. χ_mT then rapidly decreases to a minimum of 7.44 cm^3 mol^{-1} K at 1.8 K. Two of the Mn-N-O-Mn torsion angles are close to 31^o and the third is approximately 25.5^o. The two larger torsion angles fall within the grey-area for exchange propagated through the oximate bridge. The third torsion angle clearly suggests strong antiferromagnetic exchange between the two Mn^{III} ions. The Mn^{III}-N_{azide}-Mn^{II} bond angles have compacted as a result of crystal packing distortions. The bond angles of the bridging azides range from 101.0^o to 112.6 ^{o}, with an average angle of 106.4 ^{o}. The average angle suggests ferromagnetic exchange, possibly weakened by the longer bond angles. The Mn-phenolate bond distance is shorter in complex **2** than in **1** by an average of ~0.06 Å. The shortening of the bond distance might result in stronger exchange between the two triangles.

For complex **3**, χ_MT vs. T in a 0.01 T field decreases steadily with decreasing temperature from a χ_mT of 20.55 cm^3 mol^{-1} K at 300 K until approximately 50 K. Thereafter, χ_MT vs. T decreases at a faster rate until it reaches a minimum value of 4.83

$cm^3\ mol^{-1}$ K at 1.8 K.. $\chi_M T$ at 300 K is almost 6.2 $cm^3\ mol^{-1}$ K smaller than expected for a non-interacting high spin $Mn^{II}_2Mn^{III}_3$ complex which suggests dominant antiferromagnetic interactions within the complex. For complex **3**, $\chi_m T$ vs. T at fields of 1.0 and 0.01 T exhibits similar behavior as the 0.01 T field, but have smaller $\chi_m T$ minima at 1.8 K of 4.28 $cm^3\ mol^{-1}$ K and 2.34 $cm^3\ mol^{-1}$ K, respectively. The Mn-N-O-Mn torsion angles with in the Mn^{III}_3 triangles are all less than 32^o and averaged 18.2^o. Thus, it is not surprising that antiferromagnetic exchange interactions dominate. The bond angles of the end-on μ_2-η^1,η^1 azides all close to 125^o. Bridging azides with such large bond angles have been known to mediate strong antiferromagnetic exchange between metal centers.[23] Exchange between $Mn_2^{II}Mn_6^{III}$ building blocks is determined by the geometry of the bridging end-on azides. The angles formed by the bridging azides are close to 103^o. DFT studies on octahedrally coordinated Mn^{II} dimers bridged by end-on azides suggested that the optimal Mn-N_{azide}-Mn angle for ferromagnetic exchange is approximately 106^o, which would indicate that the Mn^{II} ions in complex **3** are ferromagnetically coupled.[23] There is no indication of SCM behavior from the magnetic susceptibility data. Further analysis at much lower temperatures is necessary to be certain that **3** does not exhibit ordering indicative of SCM behavior.

In an attempt to determine the nature of the spin ground state, the reduced magnetization experiment was performed on complexes **1**-**3** using fields of 1-5 T in a temperature range of 1.8-4.0 K. A plot of reduced magnetization ($M/N\mu_B$) versus field (H/T) is obtained, where M is the magnetization, N is Avogadro's number, μ_B is the Bohr magneton, and H/T is the magnetic field divided by the absolute temperature.

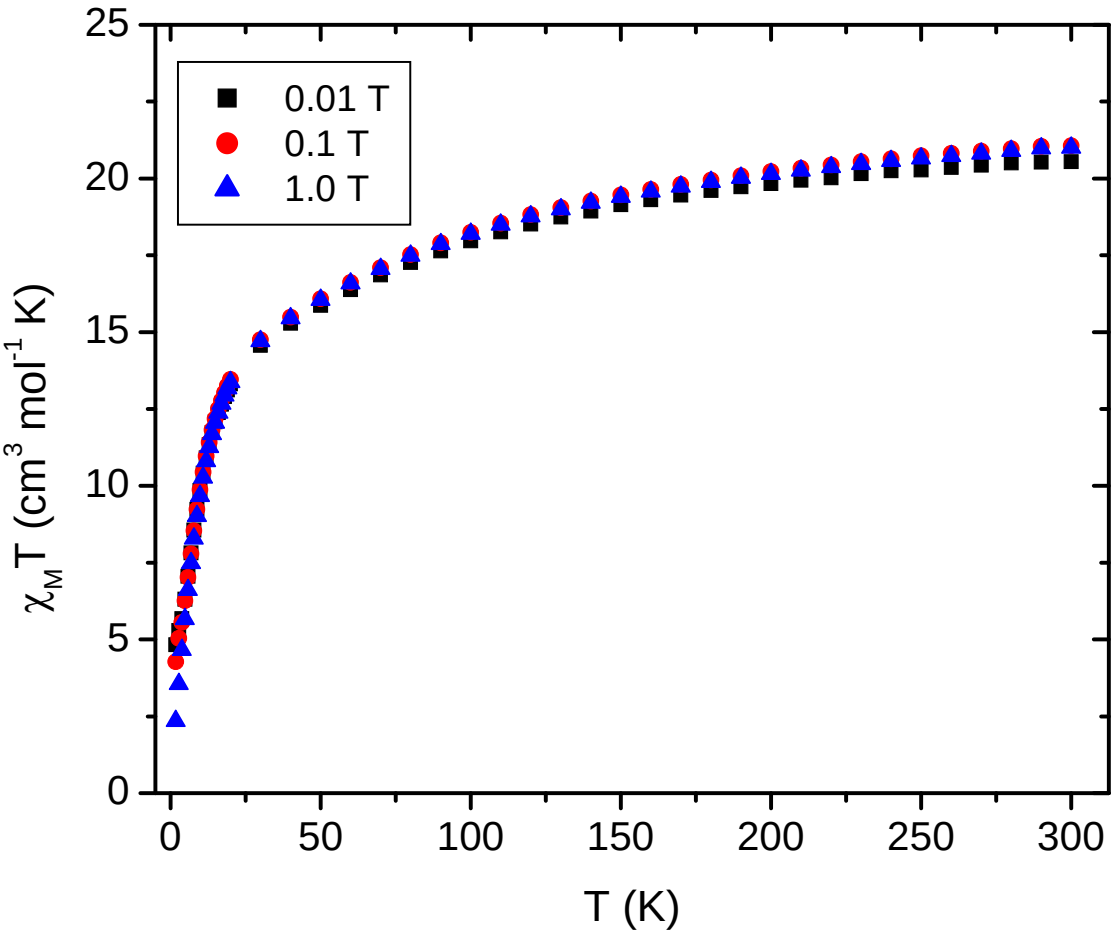

Figure 11. Plot of DC magnetic susceptibility of $[NEt_4]_2[Mn_8(salox)_6O_2(N_3)_8(MeOH)_3]_\infty \bullet 2MeOH$ (**3**).

Susceptibility data were fit using the program AXFIT which assumes a well isolated spin ground state and incorporates a full powder average. Plots of magnetization versus field for complexes **1-3** are shown in Figures 12-14.

For complex **1**, magnetization reaches a saturation value close to 13 $M/N\mu_B$ at the highest field which is close to gS = 14 for a S = 7 ground state and g = 2.00. Least-squares fitting of reduced magnetization data for fields of 3-5 T yielded parameters of S = 7, g = 2.09, and D = -0.73 cm^{-1}. Reduced magnetization for complex **2** saturated at $M/N\mu_B$ = 15.9 which is close to gS = 16 for S = 8 ground state. A poor least-squares fit of 3-5 T data gave parameters of S = 9, g = 2.00, and D = -0.51 cm^{-1}. Magnetization data for complex **3** saturated at approximately 12 $M/N\mu_B$ which is close to S = 6 for g = 2.00. A good least-squares fit of magnetization data for complex **3** was not obtained.

The presence of two structurally independent molecules in the unit cells of complexes **1** and **2** renders fits of their magnetic behavior using a model that assumes a well isolated spin ground state meaningless. Fits of magnetization for complex **3** gave either unrealistic results or failed to model experimental data.

3.3.4 AC Susceptibility

Ac susceptibility measurements were performed on polycrystalline samples of complexes **1-3** in a temperature range of 1.8-7.0 K with a 3.0 G ac field oscillating at frequencies of 10, 25, 50, 100, 250, 500, 750, and 997 Hz in zero applied dc field. The in-phase (χ_M') and out-of-phase (χ_M") molar susceptibilities for complexes **1-3** are plotted in Figures 15-16. Frequency dependent out-of-phase signals were observed for all three complexes.

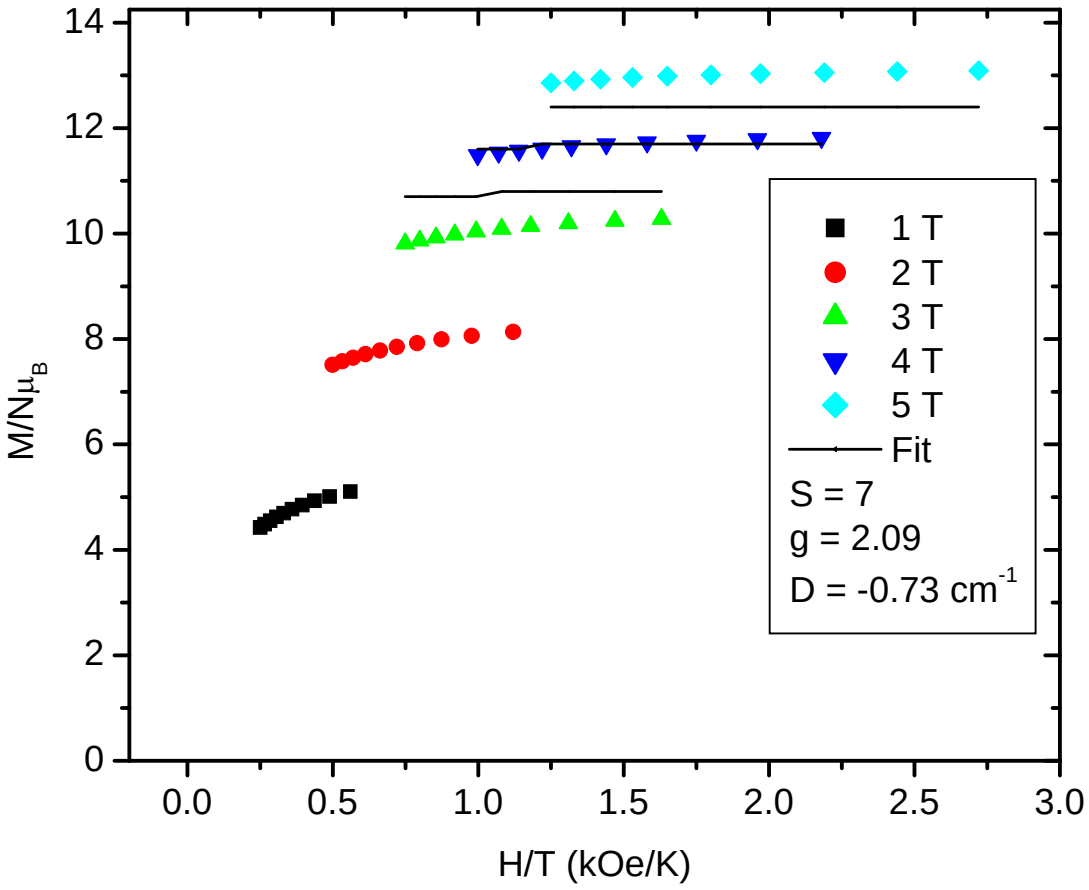

Figure 12. Plot of reduced magnetization of $[NBu_4]_2[Mn_8(salox)_6O_2(N_3)_6(MeOH)_2Cl_2] \bullet 2MeOH$ (**1**).

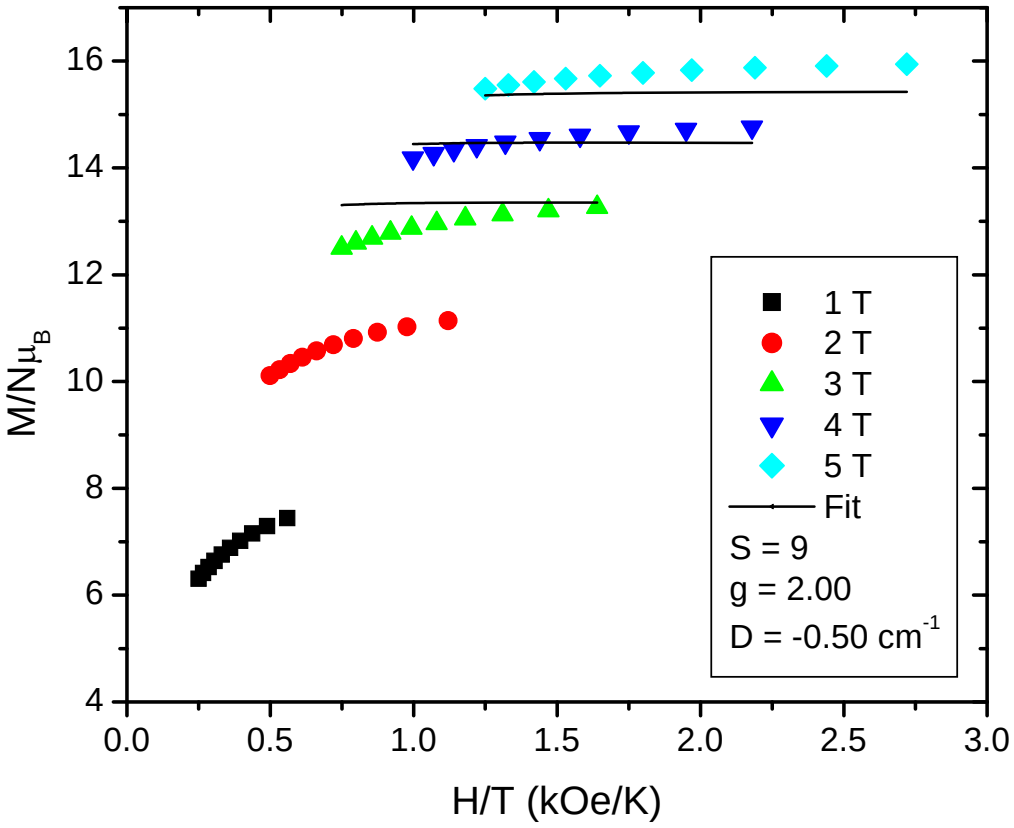

Figure 13. Plot of reduced magnetization of $[NPr_4]_2[Mn_8(salox)_6O_2(N_3)_6(MeOH)_2Cl_2] \bullet 2CHCl_3$ (**2**).

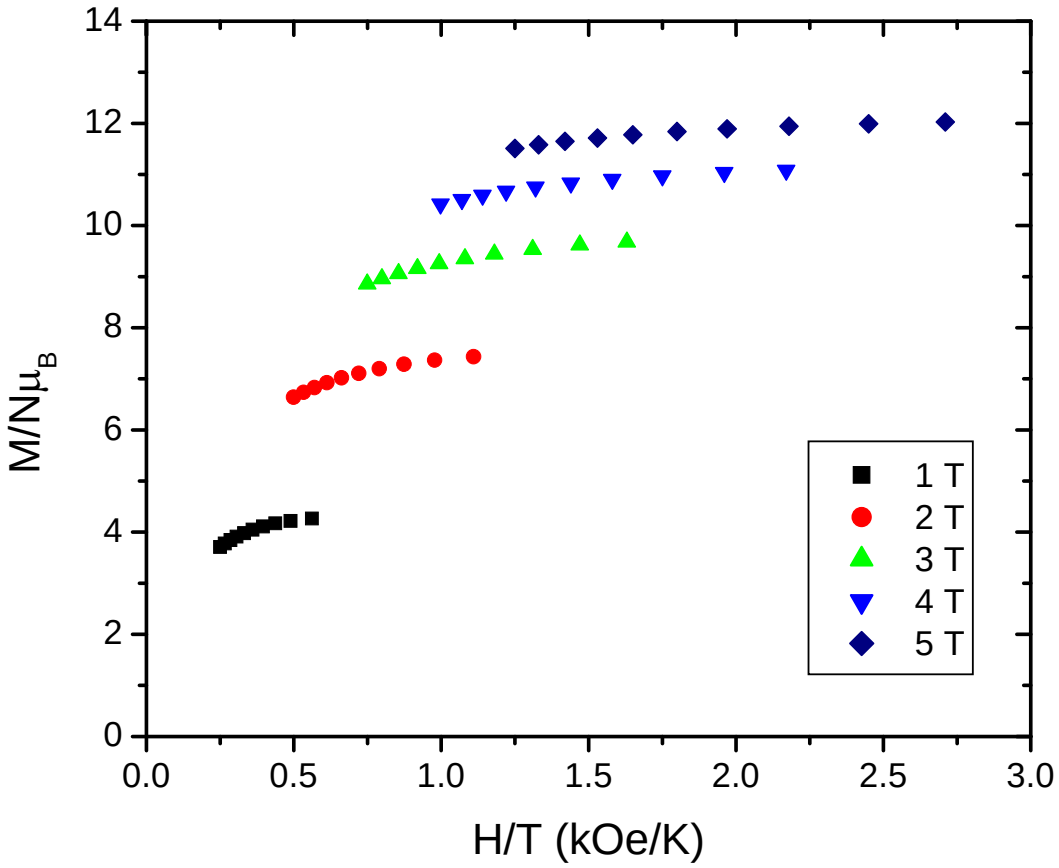

Figure 14. Plot of reduced magnetization of $[NEt_4]_2[Mn_8(salox)_6O_2(N_3)_8(MeOH)_3]_\infty$ • 2MeOH (**3**).

For complex **1**, the in-phase susceptibility increases with decreasing temperature. The signal displays a frequency dependence below approximately 4.5 K. The out-of-phase peak at 997 Hz shows a maximum at 3.8 K. The peak maximum of χ_M" decreases with decreasing frequency from 4.6 K at 750 Hz to 2.6 K at 10 Hz. The peaks of the out-of-phase component are not symmetric, and have a shoulder on the lower temperature side of the peak. The peaks were fit using Gaussian functions at all frequencies. The out-of-phase susceptibility data in the range of 10-997 Hz was fit to the Arrhenius equation (Figure 18).

$$\ln(1/\tau) = \ln(1/\tau_o) - U_{eff}/kT \qquad (3.1)$$

The fit yielded U_{eff} = 46.1 K. Extrapolation of the in-phase component as χ_M'T versus T to 0 K (Figure 19) yielded χ_M'T = 7.8 cm^3 mol^{-1} K, which is close to the spin-only χT for S = 4.

For complex **2**, in-phase susceptibility increases with decreasing temperature from 2.8 χ_M' at 7.0 K to 4.4 χ_M' at 3.8 K for a 10 Hz field. The out-of-phase peak at 997 Hz has its peak center at 3.8 K. The peaks shift from a temperate of 3.48 K at 750 Hz to 2.75 K at 10 Hz. The peaks followed Gaussian behavior at all frequencies. Out-of-phase susceptibility data in the range of 10-997 Hz were fit to the Arrhenius equation. From the fit, the barrier was determined to be 51.4 K. Extrapolation of in-phase data plotted as χ_M'T versus T to 0 K (Figure 20) yielded χ_M'T = 11.3 cm^3 mol^{-1} K, which is close to the spin-only value for S = 5.

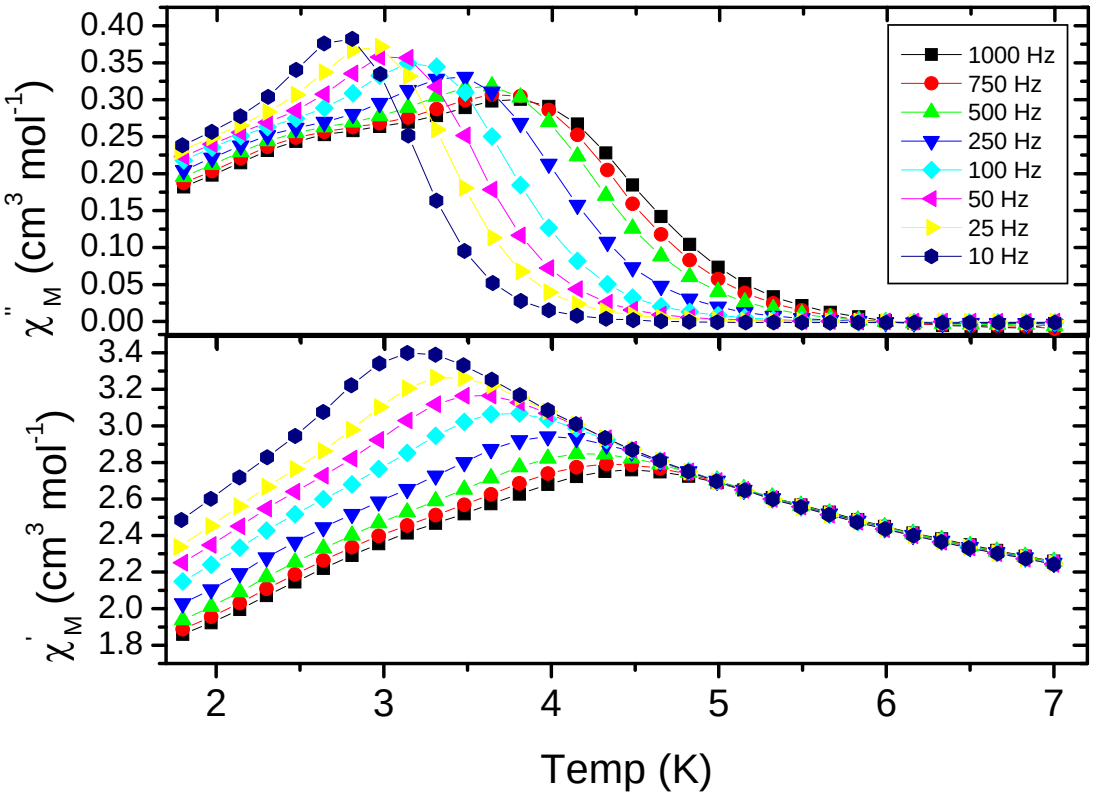

Figure 15. Plot of ac susceptibility of complex $[NBu_4]_2[Mn_8(salox)_6O_2(N_3)_6(MeOH)_2Cl_2]$ • 2MeOH (**1**). Lines serve to guide the eye.

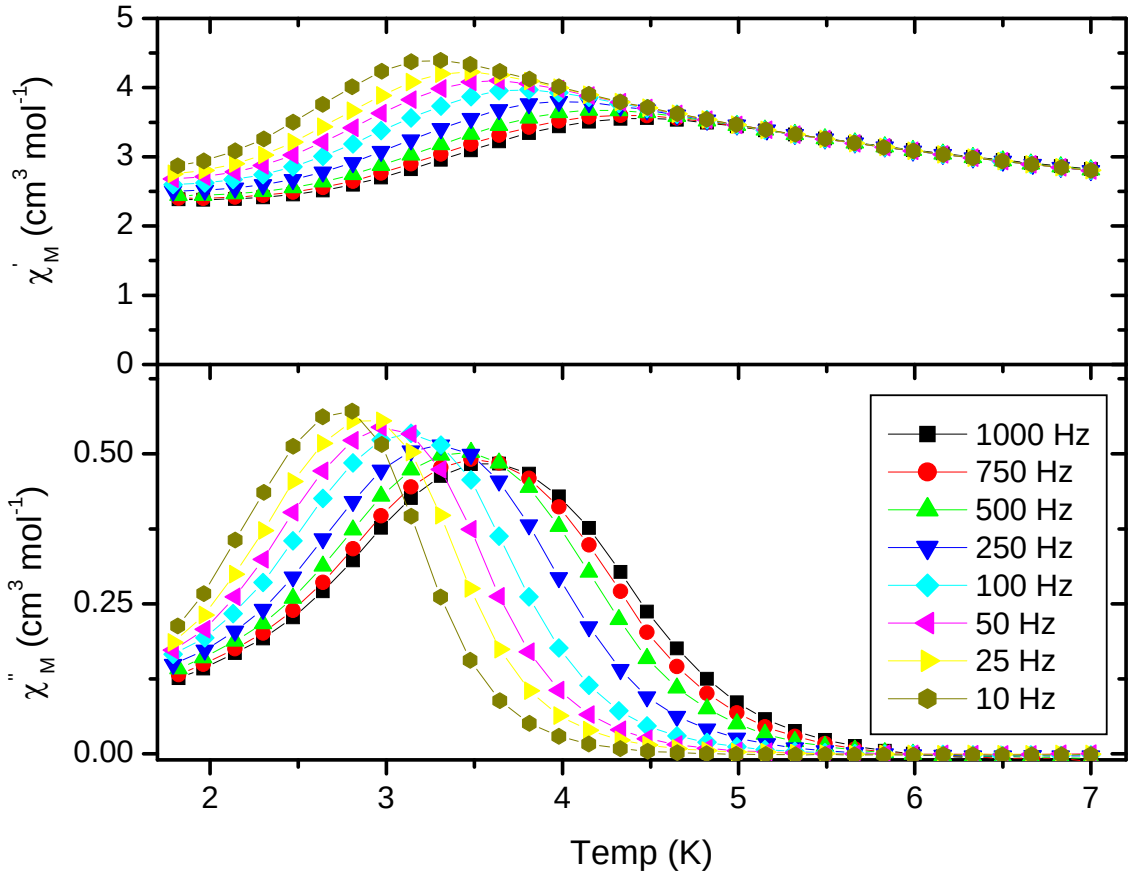

Figure 16. Plot of ac susceptibility of complex $[NPr_4]_2[Mn_8(salox)_6O_2(N_3)_6(MeOH)_2Cl_2]$ • $2CHCl_3$ (**2**). Lines serve to guide the eye.

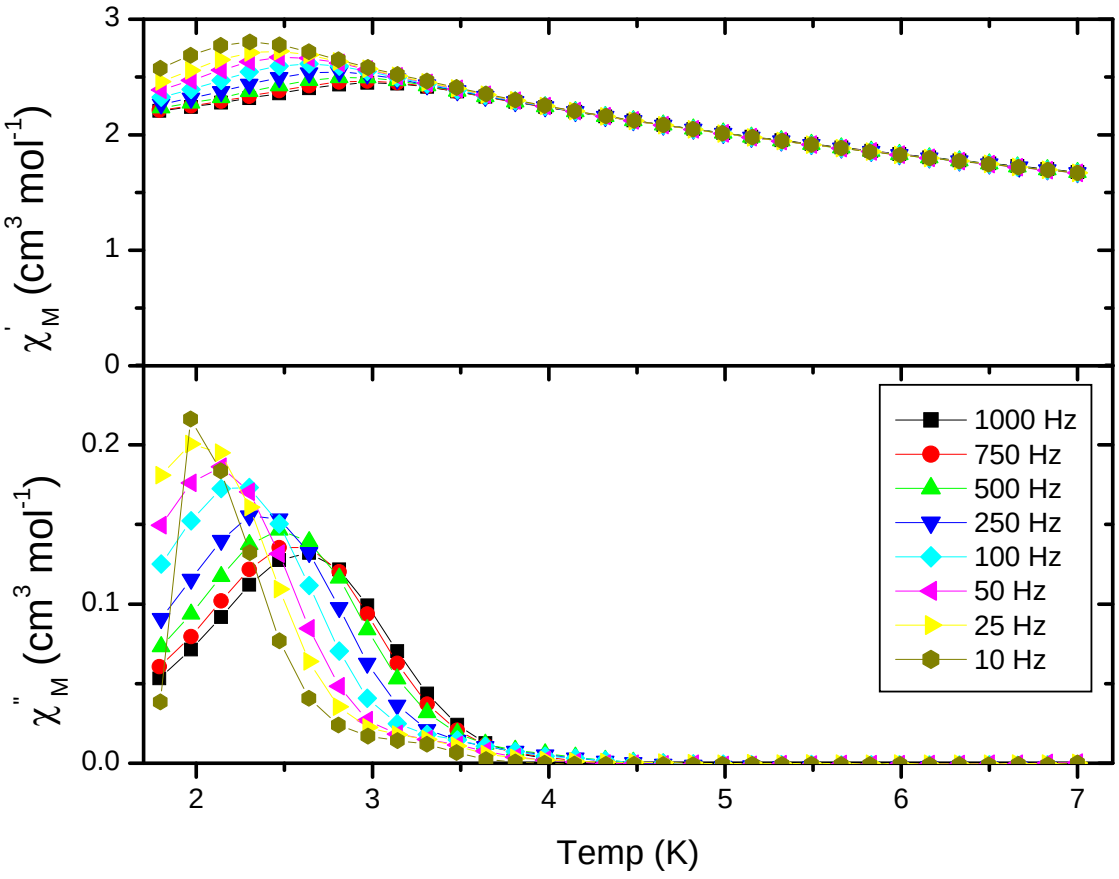

Figure 17. Plot of ac susceptibility of complex $[NEt_4]_2[Mn_8(salox)_6O_2(N_3)_8(MeOH)_2]_\infty \bullet 2MeOH$ (**3**). Lines serve to guide the eye.

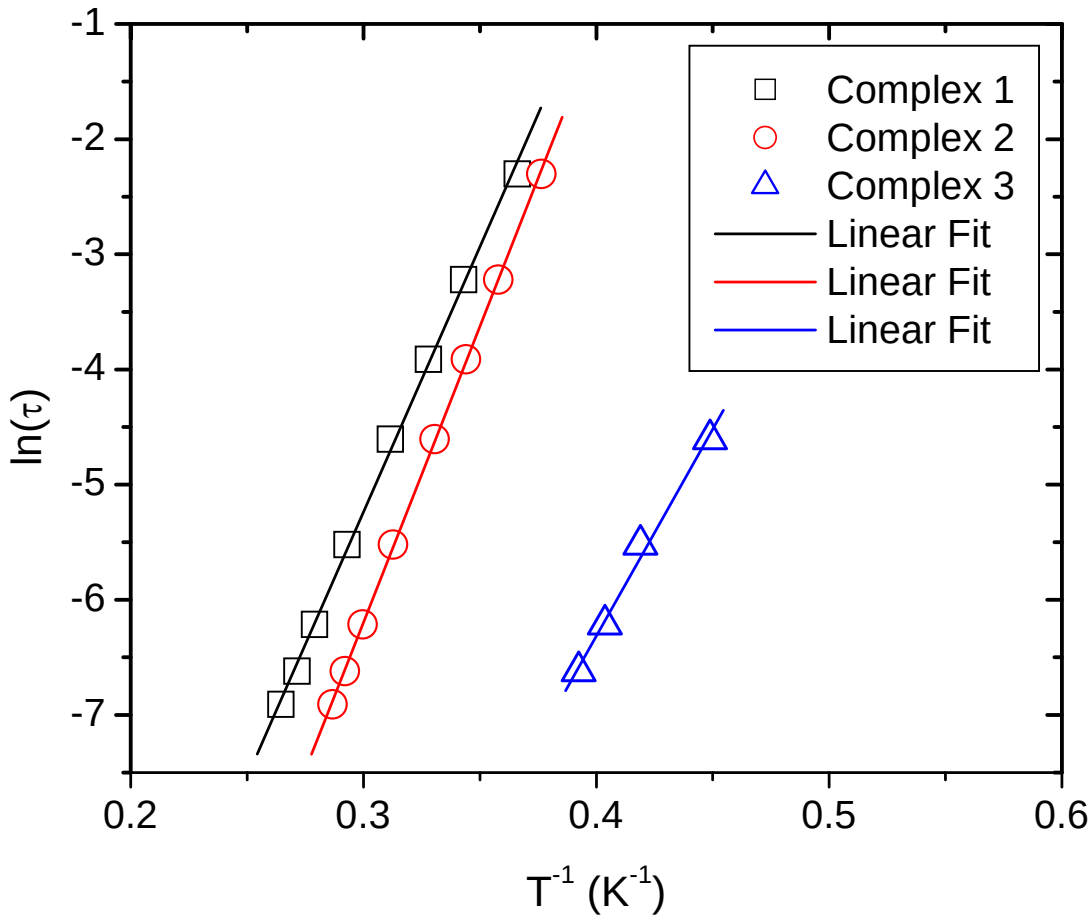

Figure 18. Plots of ln(t) versus 1/T obtained from ac susceptibility data for complexes **1-3**.

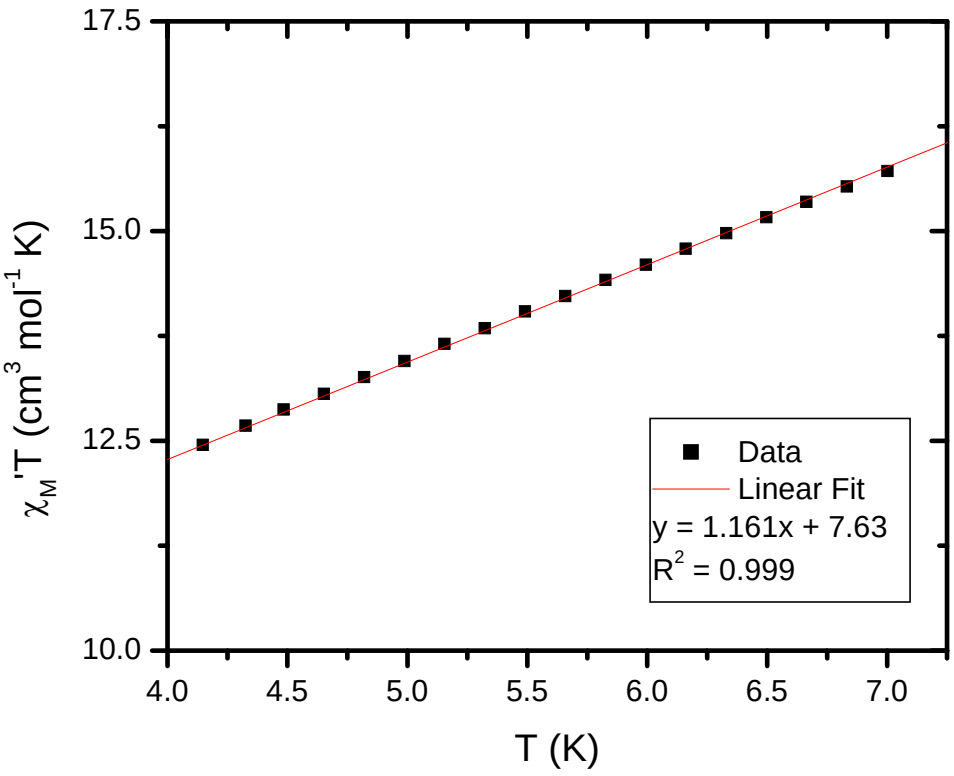

Figure 19. Plot of χ_M'T versus T extrapolated to 0 K for complex **1**.

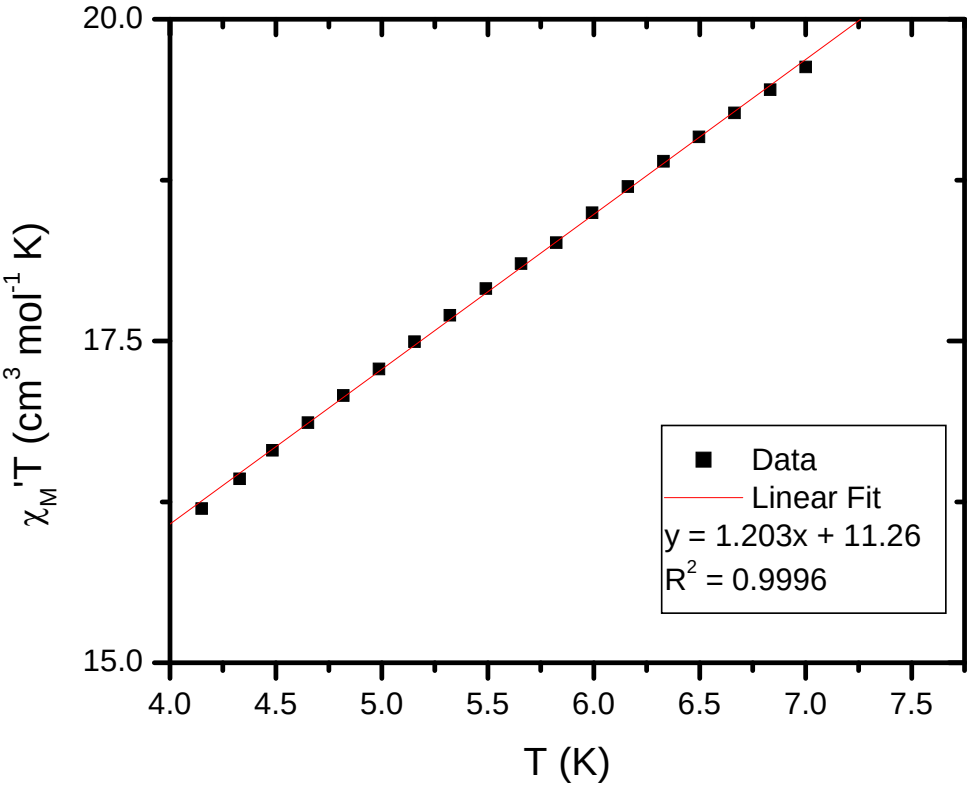

Figure 20. Plot of χ_M'T versus T extrapolated to 0 K for complex **2**.

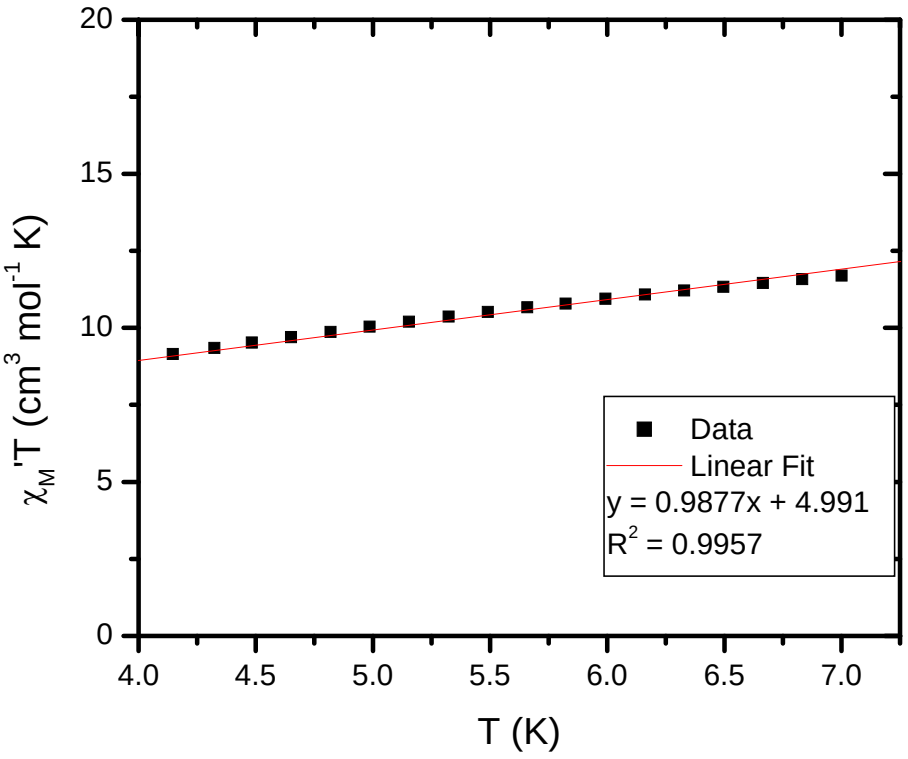

Figure 21. Plot of χ_M'T versus T extrapolated to 0 K for complex **3**.

Table 3. Summarized Magnetic Data for Mn_8 Complexes.

Compound	Formula	S	D (cm^{-1})	g	U_{eff} (K)
1	$[NBu_4]_2[Mn_8O_2(salox)_6(N_3)_6(MeOH)_2Cl_2]$	7	-0.73	2.09	46.1
2	$[NPr_4]_2[Mn_8O_2(salox)_6(N_3)_6(MeOH)_2Cl_2]$	9	-0.71	2.01	51.4
3	$[NEt_4]_2[Mn_8O_2(salox)_6(N_3)_8(MeOH)_2]_\infty$	6	-	-	31.3

For complex **3**, in-phase susceptibility increases with decreasing temperature from 1.7 χ_M' at 7.0 K to 2.8 χ_M' at 2.3 K for a 10 Hz field. The out-of-phase peak at 997 Hz has its peak center at 2.65 K. The peaks shift from a temperature of 2.6 K at 750 Hz to 2.1 K at 50 Hz. The peaks followed Gaussian behavior at all frequencies. Out-of-phase susceptibility data in the range of 50-997 Hz was fit to the Arrhenius equation. From the fit, the barrier was determined to be 31.3 K. Extrapolation of in-phase data plotted as χ_M'T versus T to 0 K (Figure 21) yielded χ_M'T = 5.0 cm^3 mol^{-1} K, which is close to the spin-only value for S = 3.

3.4 Conclusion

Two SMMs of the general formula $[NX_4]_3[Mn_8(salox)_3O_2(N_3)_6(MeOH)_2Cl_2]$•2S where R is n-propyl or n-butyl; and S is MeOH or $CHCl_3$, have been synthesized. A third SMM of the formula $[NEt_4]_3[Mn_8(salox)_3O_2(N_3)_8(MeOH)_2]$•MeOH, exhibits magnetic behavior indicative of a one dimensional coordination polymer. Their properties were characterized by X-ray crystallography and bulk magnetic susceptibility measurements. Fits of reduced magnetization data for complexes **1** and **2** suggest spin ground states of S =7 and 8 with values of D -0.73 cm^{-1} and -0.51 cm^{-1}, respectively. A fit of reduced magnetization data for complex **3** was not obtained. Extrapolation of the in-phase component at a frequency of 10 Hz of ac susceptibility indicated spin ground states of 4, 5, and 3 for complexes **1-3**, respectively. The kinetic barrier to reversal of magnetization (U_{eff}) obtained through ac susceptibility studies, are 46.1 K, 51.4 K, and 31.3 K for complexes **1-3**, respectively.

Structural distortions were induced in complexes **1** and **2** by changing the cocrystallizing counter ion. The Mn-N-O-Mn torsion angles and the bond geometries of

the bridging azides were affected the most. Although the average torsion angles of **1** and **2** are approximately the same, there was an increase by approximately 3^{o} in two of the torsion angles of **2**: from 30.3 ^{o} and 28.8 ^{o} in **1** to 32.5 ^{o} and 31.3 ^{o} in **2**. Changes in torsion angles can lead to marked changes in magnetic behavior. Complex **1** has larger bridging azide bond angles that were close to the interface between mediating antiferromagnetic versus ferromagnetic exchange. The end-on azide bond angles shortened in complex **2**, so that bond angles range from 102.6^{o} to 107.3^{o}. These structural distortions resulted in a switch from antiferromagnetic exchange in **1** to weak ferromagnetic exchange in **2**. Exchange between triangles occurs through the Mn-$O_{oximate}$ bonds and to a lesser extent the Mn-$O_{phenolate}$ contacts. Mn-$O_{oximate}$ bond distances are close to 2.39 Å in complex **1** and 2.35 Å in complex **2**. The structural distortion resulted in a shortening of the bond by ~0.04 Å in **2**, which is not significant enough to induce a major change in exchange between triangles. The presence of two structurally independent molecules in **1** and **2** complicated studies of magnetic behavior. There were subtle structural differences in each symmetry independent molecule that had the potential to have drastic effects on magnetic behavior.

The previously reported $[Mn_8(X)_6O_2(N_3)_6(MeOH)_8]$•10MeOH, where X is nap-salox or Me-salox have identical exchange pathways as complexes **1** and **2**.[21] The Mn-N-O-Mn torsion angle increases from an average of 30^{o} in the nap-salox analogue to 40^{o} in the Me-salox analogue. This results in antiferromagnetic exchange within the central triangles of the Nap-salox analogue and ferromagnetic exchange in the central triangles Me-salox analogue. However, exchange through the end-on bridging azides was antiferromagnetic in both complexes as a result of the large azide bond angles. $\chi_M T$ data

of the ferromagnetic Me-salox complex was modeled to a two-J value Kambe model where one J value accounted for magnetic exchange within each triangle and magnetic exchange between triangles through the Mn-O_{omiate} bonds (J_1) and the second J value accounted for exchange between the azide bridged Mn^{III} and Mn^{II} ions (J_2). The fit yielded parameters of J_1 = 0.6 cm^{-1} and J_2 = -1.4 cm^{-1} which confirmed the assumptions based on $\chi_M T$ behavior and molecular structure and bond geometries. Fits of reduced magnetization data in these complexes were not obtained due to the presence of low lying excited states.

Cocrystallizing solvent was changed from methanol in **1** to chloroform in **2**. Due to crystallographic disorder in **1**, methanol solvate molecules and $[NBu_4]^+$ groups were treated with PLATON program SQUEEZE and removed. This prevented a detailed study of the crystal packing features in **1** and most importantly, the location of the counter-ions and any hydrogen bonding interactions through the solvent.

Complex **3** was synthesized starting from $Mn(NO_3)_2$ in place of the manganese chloride salts used in the synthesis of **1** and **2**. The coordination environment of the apical Mn^{II} ions changed from the four coordinate tetrahedral geometry found in complexes **1** and **2** to five coordinate distorted square planar and six coordinate octahedral. The complex forms a one dimensional chain magnet by bridging of the Mn^{II} ions through two end-on bridging azides. Complex **3** is relatively well isolated as it crystallizes with two diamagnetic cations per complex unit and the closest interchain Mn-Mn contact is 9 Å. Hydrogen bonding between adjacent chains through, approximately 3.2 Å. Magnetic behavior in complex **3** was characterized by dominant antiferromagnetic interactions. Mn-N-O-Mn torsion angles were all below 32^o and had an average angle of

18.2°. Exchange between Mn^{III} and Mn^{II} ions through end-on azides was antiferromagnetic due to the large Mn^{III}-N_{azide}-Mn^{II} bond angles which averaged 120°. Exchange between the bridging Mn^{II} ions is most likely ferromagnetic due to the small bond angles of ~103°. The trend of the $\chi_M T$ vs T data for complex **3** did not indicate SCM behavior. Studies at lower temperatures are necessary in order to conclusively rule out SCM behavior.

References

1. Caneschi, A.; Gatteschi, D.; Sessoli, R.; Barra, A. L.; Brunel, L. C.; Guillot, M., Alternating-current susceptibiliy, high-field magnetization, and millimeter band EPR evidence for a ground S=10 state in $[Mn_{12}O_{12}(CH_3COO)_{16}(H_2O)_4]\cdot 2CH_3COOH\cdot 4H_2O$. *Journal of the American Chemical Society* **1991,** 113, (15), 5873-5874.

2. Sessoli, R.; Tsai, H. L.; Schake, A. R.; Wang, S. Y.; Vincent, J. B.; Folting, K.; Gatteschi, D.; Christou, G.; Hendrickson, D. N., High-Spin Molecules - [Mn12o12(O2cr)16(H2O)4]. *Journal of the American Chemical Society* **1993,** 115, (5), 1804-1816.

3. Sessoli, R.; Gatteschi, D.; Caneschi, A.; Novak, M. A., Magnetic Bistability in a Metal-Ion Cluster. *Nature* **1993,** 365, (6442), 141-143.

4. Miyasaka, M.; Clèrac, R.; Wernsdorfer, W.; Lecren, L.; Bonhomme, C.; Sugiura, K.; A. *Angew. Chem. Int. Ed.* **2004**, *43*, 2801.

5. del Barco, E.; Kent, A. D.; Hill, S.; North, J. M.; Dalal, N. S.; Rumberger, E. M.; Hendrickson, D. N.; Chakov, N.; Christou, G., Magnetic quantum tunneling in the single-molecule magnet Mn-12-acetate. *Journal of Low Temperature Physics* **2005,** 140, (1-2), 119-174.

6. del Barco, E.; Kent, A. D.; Rumberger, E. M.; Hendrickson, D. N.; Christou, G., Symmetry of magnetic quantum tunneling in single molecule magnet Mn-12-acetate. *Physical Review Letters* **2003,** 91, (4).

7. Gonzalez, G.; Leuenberger, M. N., Berry-phase blockade in single-molecule magnets. *Physical Review Letters* **2007,** 98, (25).

8. Leuenberger, M. N.; Mucciolo, E. R., Berry-phase oscillations of the kondo effect in single-molecule magnets. *Physical Review Letters* **2006,** 97, (12).

9. Wegewijs, M. R.; Romeike, C.; Schoeller, H.; Hofstetter, W., Magneto-transport through single-molecule magnets: Kondo-peaks, zero-bias dips, molecular symmetry and Berry's phase. *New Journal of Physics* **2007,** 9.

10. Coulon, C.; Miyasaka, Hitoshi; Clerac, R., Single-Chain Magnets: Theoretical Approach and Experimental Systems, *Structure and Bonding*, **2006**, 122, 163-206.

11. Miyasaka, H.; Clerac, R., Synthetic strategy for rational design of Single-Chain Magnets, *Bulletin of the Chemical Society of Japan*, **2005**, 78, 10, 1725-1748.

12. Miyasaka, H.; Clerac, R.; Mizushima, K.; Sugiura, K.; Yamashita, M.; Wernsdorfer, W.; Coulon, C., [Mn2saltmen]2Ni(pao)2L2'(A)2 with L = Pyridine, 4-Picoline, 4-tert-Butylpyridine, N-Methylimidazole and A = ClO4-, BF4-, PF6-, ReO4-: A Family of Single-Chain Magnets, *Inorganic Chemistry*, **2003**, 42, 8203-8213.

13. Yoo, J.; Wernsdorfer, W.; Yang, E. C.; Nakano, M.; Rheingold, A.; Hendrickson, D. N., One-Dimensional Chain of Tetranuclear Manganese Single-Molecule Magnets, *Inorganic Chemistry*, **2005**, 44, 3377-3379.

14. Lecren L, Roubeau O; Coulon C; Li Y.G.; Le Goff XF; Wernsdorfer W; Miyasaka H; Clerac R, Slow relaxation in a one-dimensional rational assembly of antiferromagnetically coupled [Mn-4] single-molecule magnets, *Journal of the American Chemical Society*, **2005**, 127, 49, 17353-17363.

15. Stamatatos, T. C.; Foguet-Albiol, D.; Stoumpos, C. C.; Raptopoulou, C. P.; Terzis, A.; Wernsdorfer, W.; Perlepes S. P.; Christou, G., Initial Example of a Triangular Single-Molecule Magnet from Ligand Induced Structural Distortion of a [MnIII3O]7+ Complex, *Journal of the American Chemical Society*, **2005**, 127, 15380-15381.

16. Cano, J.; Cauchy, T.; Ruiz, E.; Constantinos, J M; Constantinos, C.; Stoumpos, C.; Stamatatos, C.; Spyros, P. P.; Christou, G.; Brechin, B. K. On the origin of ferromagnetism in oximato-based [Mn3O]7+ triangles. *Dalton* **2008** 234-240.

17. Stamatatos, T. C.; Foguet-Albiol, D.; Lee, S. C.; Stoumpos, C. C.; Raptopoulou, C. P.; Terzis, A.; Wernsdorfer, W.; Hill, S. O.; Perlepes, S. P.; Christou, G. "Switching on" the Properties of Single-Molecule Magnetism in Triangular Manganese(III) Complexes, *Journal of the American Chemical Society,* **2007**, *129*, 9484–9499.

18. C. J. Milios, A. Vinslava, Wernsdorfer, W.; Moggach, S.; Parsons, S.; Perlepes, S. P.; Ghristou, G.; Brechin, E. K. A record anisotropy barrier for a single-molecule magnet *Journal of the American Chemical Society* **2007** 129, 10, 2754-2755.

19. Milios, C. J.; Piligkos, S.; Brechin, E. K. Ground state spin-switching via targeted structural distorsion: twisted single-molecule magnets from derivatised salicyaldoximes *Dalton* **2008**, 1809-1817.

20. Milios, J. C.; Inglis, R.; Vinslava, A.; Prescimone, A.; Parsons, S.; Spyros, P P.; Christou, G.; Brechin, E. K. Turning up the spin, turning on single-molecule magnetism: from S = 1 to S = 7 in a [Mn8] cluster via ligand induced structural distortion, *Chemical Communications*, **2007**, 2738-2740.

21. Carlin, R. L., *Magnetochemistry*. Springer-Verlag: New York, 1986.

22. Zeng, Y. F.; Hu, X.; Liu, F. C.; Bu, X. H. Azido-mediated systems showing different magnetic behaviors. *Chemical Society Reviews*, **2009**, 38, 469-480.

23. Ruiz, E.; Cano, J.; Alvarez, S.; Alemany, P., Magnetic Coupling in End-On Azido Bridged Transition Metal Complexes: A Density Functional Study. *Journal of the American Chemical Society*, **1998**, 120, (43), 11122-11129.

Chapter Four

Large Assemblies of Oxime Stabilized μ_3-oxo-Mn_3^{III} Triangles

4.1 Introduction

Single-molecule magnets (SMMs) are polynuclear transition metal complexes that possess appreciable uniaxial anisotropy which is characterized by a negative zero-field-splitting term, DS_z^2, and a large spin ground state.[1-3] This results in a barrier to the reversal of magnetization which is given by $|D|S^2$ in integer systems and $|D|(S^2 - 1/4)$ in half-integer systems. When a field is applied, the moments of the individual molecules will align with the applied field. At a low enough temperature, the magnetization reversal will occur very slowly, in some cases with a relaxation time on the order of months.

Research involving oxime-stabilized Mn_3^{III} triangles has seen tremendous growth since the discovery of the first ferromagnetic example in 2005.[4] Since then, much work has been focused on determining the origin of ferromagnetic exchange within these triangles.[5-7] Magneto-structural correlations and DFT calculations have revealed that the degree of the planarity of the central μ_3-oxo, the alignment of the Mn^{III} Jahn-Teller axes, and the twist of the Mn-N-O-Mn moiety, as represented by the Mn-N-O-Mn torsion angle, all play an important roles in determining the nature of the magnetic exchange within the triangle.[6,7] By breaking the planarity of the central μ_3-oxo and the oxime moiety, it reduces the overlap of orbitals which contribute to antiferromagnetic exchange. Through magneto-structural correlations it was determined that torsion angles greater than approximately 32^o mediate ferromagnetic exchange.[8]

As demonstrated in chapter II and III of this work, oxime stabilized Mn_3^{III} triangles provide an ideal building block for larger topologies. In chapter III, a series of

$Mn_2^{II}Mn_6^{III}$ complexes that consist of two off-set $[Mn_3^{III}–(\mu_3\text{-oxo})]^{+7}$ triangles with the formula $[NX_4]_2[Mn_2^{II}Mn_6^{III}\ O_2(salox)_6(N_3)_6(MeOH)_2Cl_2]$ were characterized. Logically, a Mn_3^{III} triangle could also be attached to the faces of the Mn_3 triangles of the Mn_6^{III} core.

The oxime ligand provides a great deal of flexibility as it can be modified relatively easily and analogues with various functional groups are readily available from commercial sources. It is shown in this chapter that the modification of salicylaldoxime can result in the synthesis of a new three-dimensional porous material. This complex falls into the class of compounds known as metal-organic frameworks (MOFs).[9] MOFs are new class of porous materials composed of metal centers bridged by organic linkers. These compounds have demonstrated remarkable porosity given their size. Applications of MOFs range from gas separation, to catalysis, and sensing.[10-12]

The use of first row transition metals and lanthanides in the synthesis of MOFs can impart magnetic behavior in the material. Many of the reported three dimensional magnetic MOFs consist of cobalt or other anisotropic first row transition metals bound through short bridging ligands such as cyanide or oxalate.[13] Layered compounds of ferrimagnetic or ferromagnetic ordered cobalt ions bridged between layers with ligands such as 4,4'-bipyridine are the most prominent three dimensional magnetic MOFs.[13] This type of environment leads to long range magnetic ordering due to intermolecular magnetic exchange interactions which preclude SMM behavior. It is possible to assemble a MOF from building blocks which are known to exhibit SMM behavior. By isolating these units with diamagnetic ions such as Zn^{II} or Na^{I}, SMM behavior can be preserved.

In this chapter two very distinct new complexes are described. Complex **1** is a Mn_{12}^{III} complex which consists of four μ_3-oxo Mn_3^{III} triangles. A Mn^{III}_6 core is formed on which two azide bridged Mn_3^{III} triangles cap the "upper" and "lower" faces. The complex forms a one-dimensional network by hydrogen bonding through a water molecule which is axially coordinated to a Mn^{III} ion and the phenolate oxygen of neighboring units. Complex **1** is characterized by bulk susceptibility measurements and X-ray crystallography.

The second complex reported in this chapter is a three dimensional MOF composed of oxime stabilized Mn_3^{III} triangles. The use of 3-ethoxysalicylaldoxime (Scheme 1) in the synthesis of the Mn_3^{III} triangles formed a pocket in which a six coordinate sodium ion resides. The sodium ions bridge adjacent Mn_3^{III} triangles, which results in the propagation of a three dimensional helical array. The complex crystallizes in the cubic lattice Pa-3 with a cell volume of 35,291(5) $Å^3$, of which approximately 18% is void space. Its structural and thermal properties are characterized using single crystal X-Ray diffraction, powder X-ray diffraction (PXRD), and thermogravimetric analysis (TGA). The materials ability to adsorb gases was determined through gas adsorption measurements with H_2, N_2, Ar, and CO_2. Magnetic properties were characterized though bulk magnetic susceptibility measurements which suggest the presence of a nonzero zero-field-splitting term D. Although complex **2** has high crystal symmetry, the triangular building blocks have low site symmetry (C_3 and C_1) which can allow a negative D.

4.2 Experimental Section

4.2.1 Compound Synthesis

All procedures were carried out under aerobic conditions. Reagents were used as is unless otherwise noted. EtO-salox, (Scheme 1) was synthesized according to literature procedure from 3-ethoxysalicylaldehyde and hydroxylamine.[14] **Caution!** Azide salts are highly toxic and potentially explosive. Although no problems were encountered in this work, they should be prepared in small quantities and handled with care.

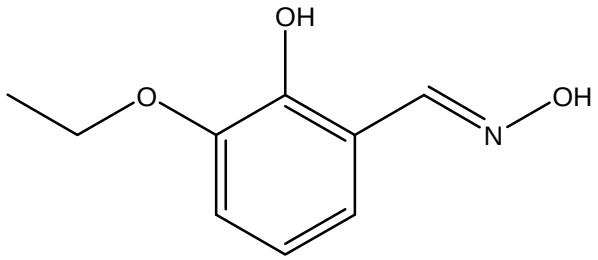

EtO-salox

Scheme 1. 3-ethoxysalicylaldoxime

$[Mn_{12}O_4(salox)_{12}(N_3)_4(MeOH)_8(H_2O)_2]\cdot 2MeOH\cdot H_2O$ (1). $Mn(NO_3)_2\cdot 4H_2O$ (197 mg, 1.00 mmol) was dissolved in a 1:2 ratio solution of methanol and chloroform (30 mL). NaN_3 (68 mg, 1.0 mmol) and H_2salox (137 mg, 1.0 mmol) were added consecutively. The dark green solution was stirred for 15 minutes before sodium hydroxide (100 mg) was added. The dark green solution was stirred for an additional hour before being gravity filtered. The solution was left standing for one month, after which time dark brown plates formed in 20% yield (based on Mn). Select IR: 3427 cm^{-1} (b), 3011 cm^{-1} (w), 2060 cm^{-1} (s), 1597 cm^{-1} (s), 1438 cm^{-1} (m), 1027 cm^{-1} (m) 915 cm^{-1}

(m), 680 cm^{-1} (m). Elemental Analysis calculated: 39.46 %C 3.12 %H 12.4 %N. Experimental: 35.59 %C 3.26 %H 8.96 %N.

$[Mn_{13}Na_9O_4(EtO\text{-}salox)_{12}(N_3)_6(MeOH)_9(H_2O)_7Cl_3]_\infty$ (2). $MnCl_2 \cdot 4H_2O$ (330 mg, 1.67 mmol) was dissolved in methanol (40 mL). NaN_3 (130 mg, 2.0 mmol) and EtO-salox (185 mg, 1.0 mmol) were added consecutively. The NaN_3 was predissolved in 1 mL of H_2O before addition. The dark green solution was stirred for 15 minutes before sodium hydroxide (120mg, 3.0 mmol) was added. The dark green solution was stirred for 45 minutes before being gravity filtered and layered with diethyl ether (2:1 v:v). Thin brown plates formed over three days in 45% yield (based on Mn). The crystals were washed with methanol to remove starting material. Select IR: 3390 cm^{-1} (b), 2979 cm^{-1} (w), 2067 cm^{-1} (s), 1590 cm^{-1} (m), 1452 cm^{-1} (m), 1217 cm^{-1} (m), 1041 cm^{-1} (m), 684 cm^{-1} (m). Elemental Analysis calculated: 37.84 %C 4.61 %H 11.32 %N. Experimental: %C %H %N.

4.2.2 Single-Crystal X-ray Crystallography

Diffraction data were collected using a Bruker Smart Apex CCD diffractometer at 100 K. The data were integrated using the Bruker SAINT software program and scaled using the SADABS software program. Complexes were solved by direct methods (SHELXL-97), developed by successive difference Fourier syntheses, and refined by full-matrix least-squares on all F^2 data. All non-hydrogen atoms were refined anisotropically by full-matrix least-squares (SHELXL-97). All hydrogen atoms were placed using a riding model. Their positions were constrained relative to their parent atom using the appropriate HFIX command in SHELXL-97.

4.2.3 Magnetic Studies

Variable temperature dc and ac magnetic susceptibility data were collected on well ground polycrystalline samples restrained in eicosane to prevent torquing of the sample in the magnetic field. Dc magnetic susceptibility measurements were performed on a Quantum Design MPMS-5 SQUID magnetometer equipped with a 5.5 T magnet in a temperature range of 300-1.8 K in magnetic fields ranging from 0.01 to 5.0 T. Ac magnetic susceptibility data were collected in a 3 Oe ac field from 10-997 Hz in zero applied dc field in a temperature range of 1.8-7.0 K. The measurements were performed using a Quantum Design MPMS-2 SQUID magnetometer equipped with a 3 T magnet. Diamagnetic corrections were estimated from Pascal's constants[18] and subtracted from the experimental susceptibility data to obtain the molar paramagnetic susceptibility of the compounds.

4.2.4 Powder X-Ray Diffraction

PXRD data were collected at ambient temperature on a Rigaku Miniflex II diffractometer at 30 kV, 15 mA for Cu Kα (λ = 1.5418 Å), with a scan speed of 1°/min or 5°/min, a step size of 0.05° in 2θ, and a 2θ range of 3−40°. The experimental backgrounds were corrected using the Jade 5.0 software package. The simulated PXRD pattern was calculated from the single crystal diffraction data using Mercury CSD 2.0.

4.2.5 Thermogravimetric Analysis

Approximately 10−20 mg of complex **2** was analyzed under a stream of dinitrogen using a TA Instrument Q600 SDT running from room temperature to 600 °C with a scan rate of 5 °C/min.

4.2.6 Other Physical Measurements

Elemental analysis data were performed by Numega Resonance Laboratories (San Diego, CA). IR spectra were collected samples on powder samples in a KBr pellet on a Thermo-Nicolet Avatar 360 spectrophotometer in a range of 400-4000 cm^{-1}.

4.3 Results and Discussion

4.3.1 Discussion of Synthesis

Complex **1** was synthesized by the addition of reagents to a 2:1 solution of chloroform and methanol. The solution was left to slowly evaporate over the course of three weeks after which time complex **1** crystallizes as small thin plates. The mixed solvents are crucial in that it prevents the formation of $Mn_2^{II}Mn_6^{III}$ side products.

Complex **2** was synthesized by the addition of reagents to a methanolic solution followed by crystallization from layering with diethyl ether. No other products formed from this reaction. Crystals were well formed and hand separated for magnetic and gas adsorption measurements.

A Mn^{III} complex and a mixed valence Mn^{II}/Mn^{III} complex were obtained from Mn^{II} salts. It is common in the synthesis of mixed valence manganese complexes that atmospheric O_2 oxidizes Mn^{II} ions. Solutions of Mn^{II} salts are colorless or slightly pink. Following the addition of azide and the oxime, the solution started to obtain a faint dark green tinge. After the addition of a deprotonating agent, the solution rapid darkens which indicates the formation of Mn^{III} salts.

The addition of the ethoxy group to salicylaldoxime forms a pocket in which a six coordinate sodium ion sits. The sodium ions form a diamagnetic bridge between neighboring units. The sodium ions impart variability into the structure, as they can be

replaced with larger alkali metals such as rubidium or cesium. These larger alkali metals could lead to greater thermal stability in the complex or change the pore diameters.

Attempts were made in synthesizing an analogue of this complex without sodium azide, by using sodium hydroxide as both a deprotonating agent and as a source of sodium ions. It was hoped that by removing the central azide bridged Mn^{II} ion, it would increase the void space within the crystal lattice. However, these efforts have been unsuccessful thus far.

4.3.2 Description of Structures

Crystallographic data and refinement parameters can be found in Table 1. ORTEP representation and crystal packing diagram of complex **1** can be found in Figures 1-3. Complex **1** crystallizes in the triclinic space group P-1. The complex has the same Mn_6 core as those of complexes reported in Chapter III, which consists of two off-set $[Mn_3^{III}–(\mu_3\text{-oxo})]^{+7}$ triangles related by an inversion center. Two axially coordinated $\mu_2–\eta^1:\eta^1$ azides are bound to the Mn^{III} ions (forming the Jahn-Teller axes) and bridge to a capping Mn_3^{III} triangular unit. Within the capping subunit, three Mn^{III} ions are bound by a $\mu_3\text{-}O^{2-}$ and three oximate ligands: two of which are in a $\mu_2–\eta^1:\eta^1:\eta^1$ bridging mode, and the third in a $\mu_2–\eta^1:\eta^1:\eta^2$ bridging mode where the oximate oxygen is bridging a Mn^{III} ion of the "lower" triangular subunit. An axial solvent molecule, either methanol or water, completes the octahedral coordination sphere of the Mn^{III} ions on the "outer face" of the triangle. The $Mn\text{-}O_{slovent}$ bond distances range from 2.3 Å to 2.9 Å. There are six unique Mn-N-O-Mn torsion angles ranging from $\theta = 38.8^o$ to 13.7^o. Mn-N-O-Mn torsion angles within the central triangle are $\theta = 13.8^o$, 17.6^o, and 32.2^o.

Table 1. Crystallographic Information for Complexes **1** and **2**.

	1	2
Empirical formula	C96 H86 Cl0 Mn12 N24 O44	C117 H138 Cl3 Mn13 N30 Na6 O56
Formula weight	2939.17	3819.08
Temperature	100(2) K	100(2) K
Wavelength	0.71073 Å	0.71073 Å
Crystal system	Triclinic	Cubic
Space group	P-1	Pa-3
Unit cell dimensions	a = 12.4399(18) Å	a = 32.801(3) Å
	b = 14.194(2) Å	b = 32.801(3) Å
	c = 19.066(3) Å	c = 32.801(3) Å
	α= 85.749(2)°	α= 90°
	β= 73.073(2)°	β= 90°
	γ = 66.341(2)°	γ = 90°
Volume	2946.5(7) $Å^3$	35291(5) $Å^3$
Z	1	8
Density (calculated)	1.656 Mg/m^3	1.438 Mg/m^3
Absorption coefficient	1.334 mm^{-1}	1.039 mm^{-1}
F(000)	1482	15520
Crystal color/habit	brown plate	brown prism
Theta range for data collection	1.12 to 25.63°	1.39 to 25.43°
Reflections collected	37342	221658
Independent reflections	11005 [R(int) = 0.0864]	10862 [R(int) = 0.1519]
Completeness to theta = 25.00°	99.8 %	100.0 %
Data / restraints / parameters	11005 / 0 / 775	10862 / 0 / 676
Goodness-of-fit on F^2	1.023	1.121
Final R indices [I>2sigma(I)]	R1 = 0.0706, wR2 = 0.1566	R1 = 0.0782, wR2 = 0.1974
R indices (all data)	R1 = 0.1082, wR2 = 0.1722	R1 = 0.1362, wR2 = 0.2252
Largest diff. peak and hole	0.783 and -0.735 $e.Å^{-3}$	1.298 and -0.517 $e.Å^{-3}$

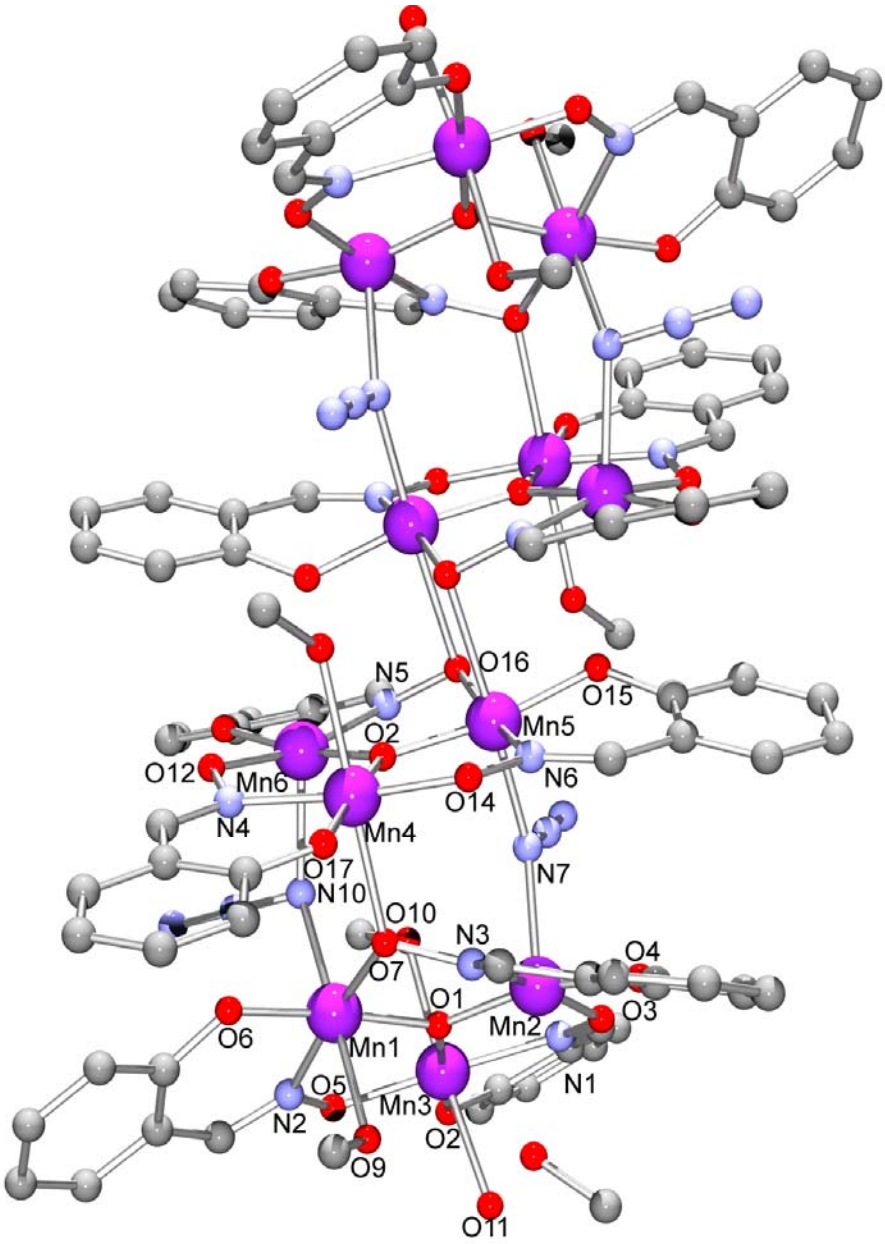

Figure 1. $[Mn_{12}{}^{III}O_4(salox)_{12}(N_3)_4(H_2O)_2(MeOH)_6]$ (**1**) rendered in POV-RAY format. Hydrogen atoms omitted for clarity.

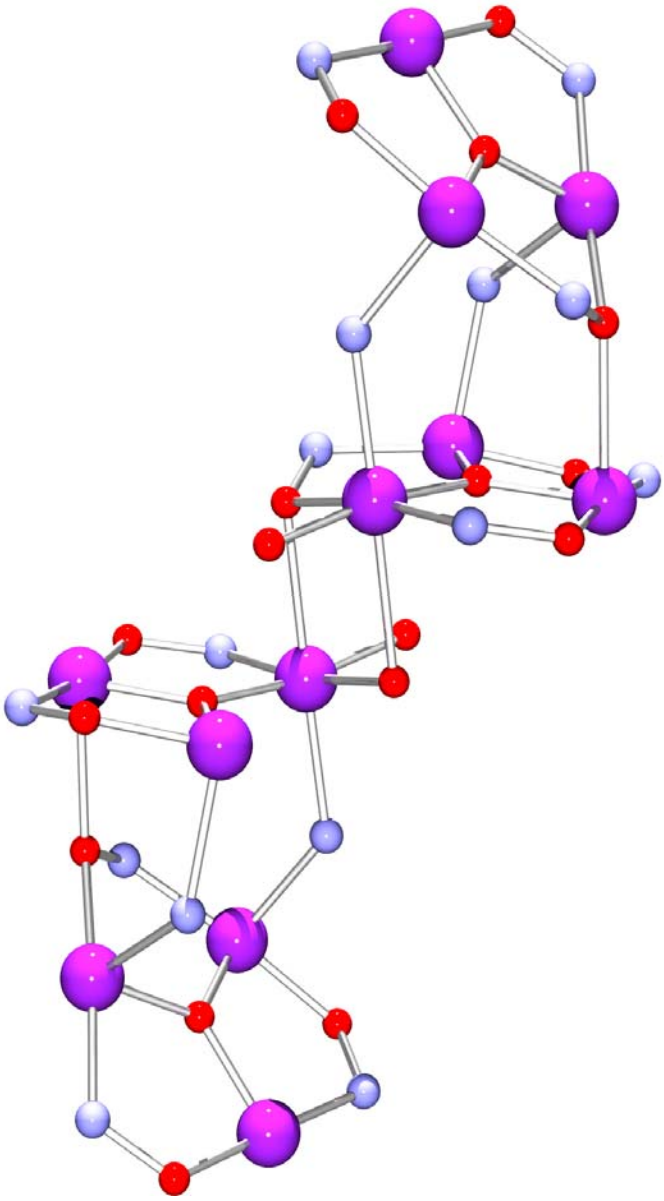

Figure 2. Core of $[Mn_{12}^{III}O_4(salox)_{12}(N_3)_4(H_2O)_2(MeOH)_6]$ (**1**) rendered in POV-Ray. Where purple spheres represent manganese, blue spheres represent nitrogen, red spheres represent oxygen.

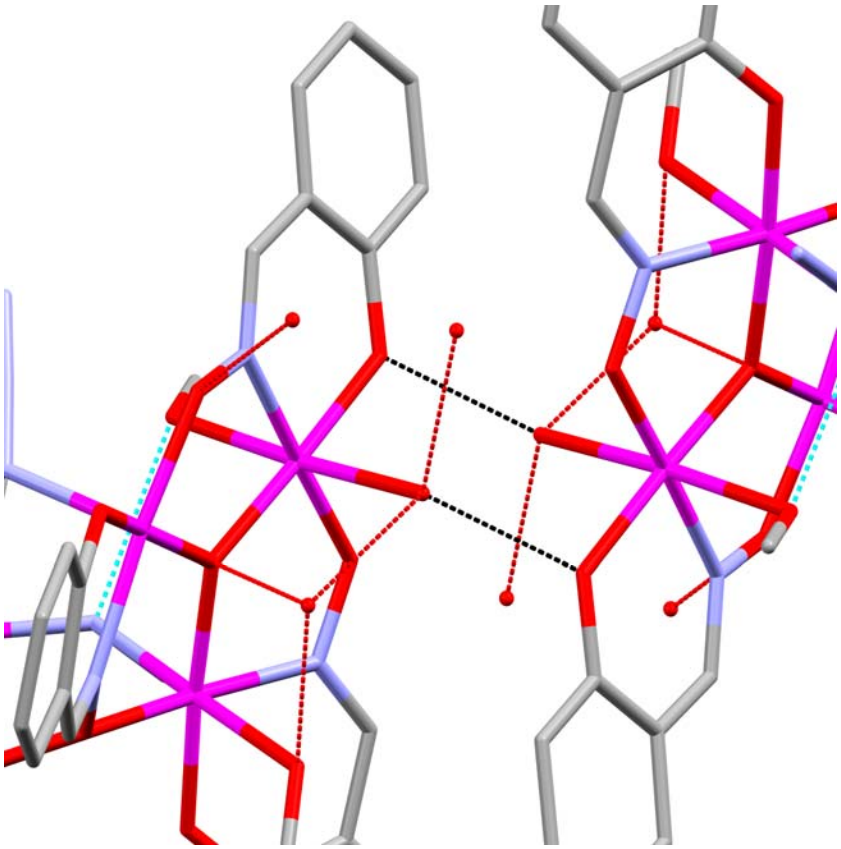

Figure 3. Illustration of intermolecular hydrogen bonding in (**1**) between an axially coordinated water molecule and the phenolate oxygen of an adjacent complex.

Mn-N-O-Mn torsion angles in the outer triangle are θ = -38.8°, 13.7°, and 22.8°. The negative torsion angle implies that the Mn-N-O-Mn moiety is twisted in a direction opposite to the adjacent Mn-N-O-Mn moieties. The two Mn^{III}-N_3-Mn^{III} bond angles, Mn(3)-N(10)-Mn(6) and Mn(1)-N(7)-Mn(6), are θ = 126 ° and 132.4°, respectively. The bridging Mn-oximate and Mn-phenolate bond distances between the central Mn^{III} triangles, Mn(5)-O(16) and Mn(6)-O(15'), are 2.5 Å and 2.7 Å respectively. The bridging Mn-oximate bond distance between the capping and central Mn^{III} triangles, Mn(4)-O(7), is 2.4 Å.

One fourth of the molecule packs at the intersection of the ac and ab planes. Intramolecular hydrogen bonding occurs between the coordinated methanols of the central triangles (O18) and the oximate oxygen (O16) at a distance of approximately 2.8 Å. Intramolecular H-bonding also occurs between the bridging nitrogen atom of an azide (N10) and a hydroxyl proton of a coordinated methanol of the upper face (O10) at a distance of approximately 2.8 Å. Additional intramolecular H-bonding occurs between the solvent molecules capping the outer triangles at distances of approximately 2.6-2.7 Å. Hydrogen bonding occurs between complexes via the capping water molecule of the outer Mn^{III} triangle (O11) and the phenolate oxygen (O3) at a distance of approximately 2.7 Å. This H-bonding propagates along the ac plane, forming a one-dimensional network.

Complex **2** crystallizes in the cubic space group Pa-3. ORTEP and crystal packing diagrams of complex **2** can be found in Figures 4-6. The complex is a three dimensional extended structure whose core building block is composed of three outer

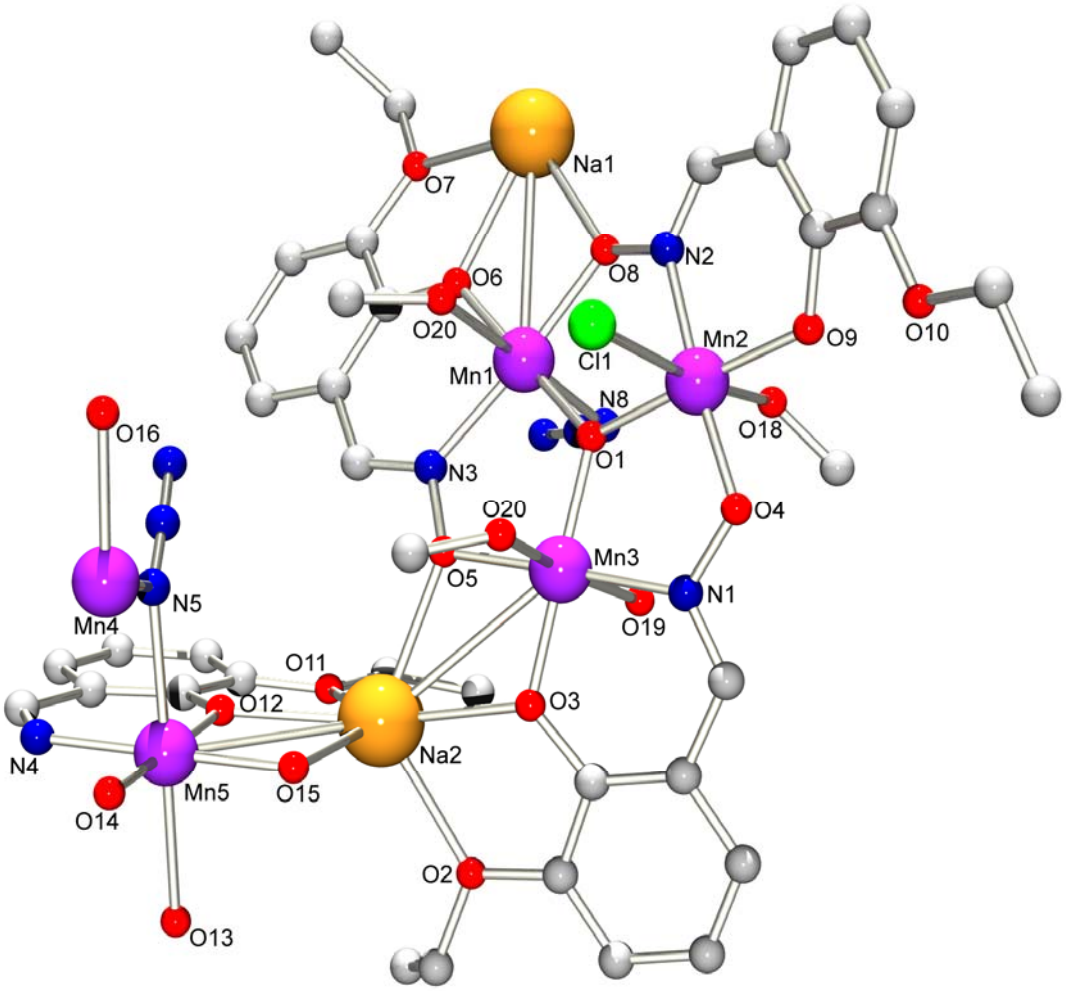

Figure 4. Asymmetric unit of $[Mn^{II}Mn_{12}{}^{III}Na_6O_4(EtO\text{-}salox)_{12}(N_3)_9Cl_3(H_2O)_7(MeOH)_6]_\infty$ (**2**) rendered in POV-Ray.

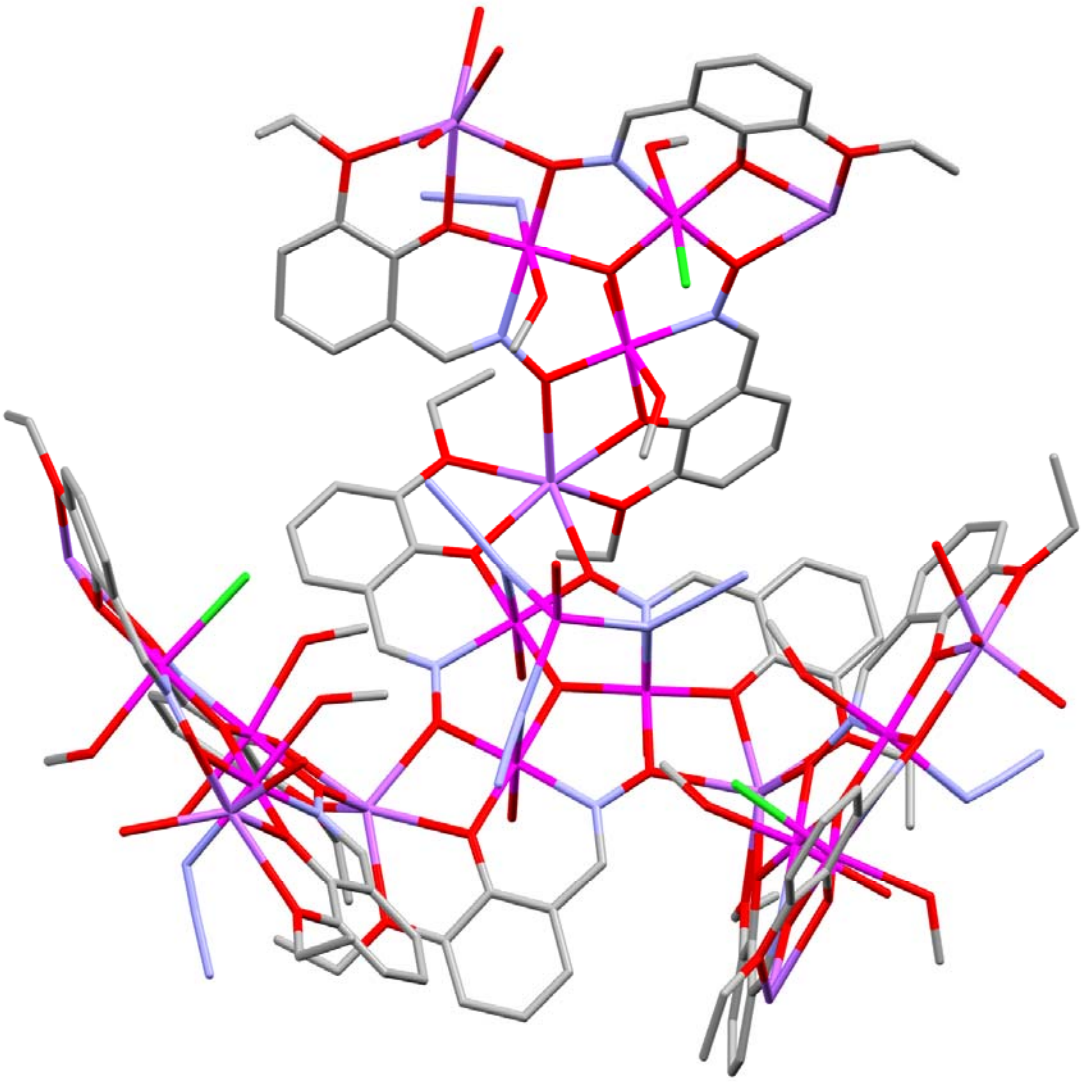

Figure 5. Core of $[Mn^{II}Mn_{12}{}^{III}Na_6O_4(EtO\text{-}salox)_{12}(N_3)_9Cl_3(H_2O)_7(MeOH)_6]_\infty$ (**2**). Pink caps represent manganese, purple caps represent sodium, blue caps represent nitrogen, red caps represent oxygen, grey caps represent carbon, and green caps represent chlorine.

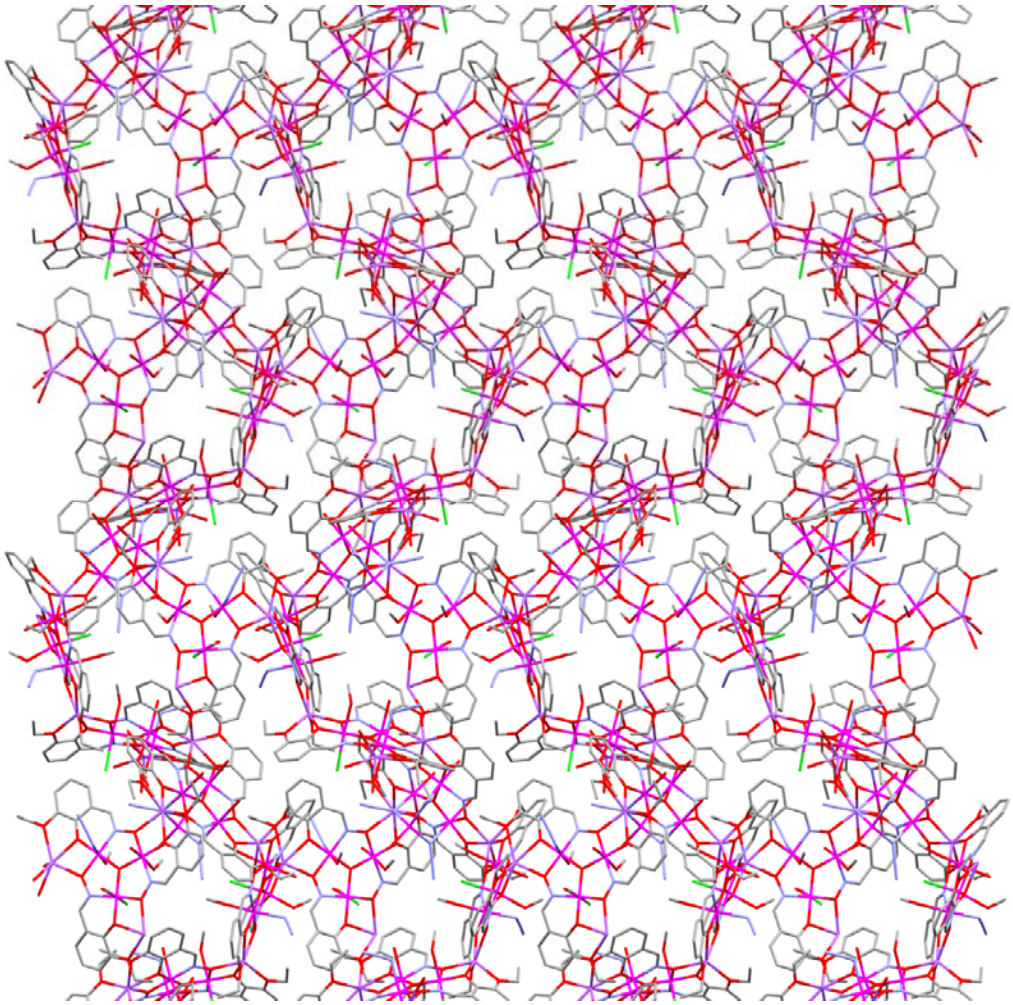

Figure 6. Packing of $[Mn^{II}Mn_{12}{}^{III}Na_6O_4(EtO\text{-}salox)_{12}(N_3)_9Cl_3(H_2O)_7(MeOH)_6]_\infty$ (**2**) in the ab plane.

Table 2. Select Structural Parameters for Complex **1**.

Compound	Formula	out of plane μ_3-O^{-2}	Mn-N-O-Mn torsion angle (deg.)	Mn^{III}-N_3-Mn^{II} angle (deg.)	Mn-$O_{phenolate}$ (Å)	Mn-$O_{oximate}$ (Å)
1	$[Mn_{12}O_4(salox)_{12}(N_3)_4(MeOH)_8(H_2O)_2]$	0.02	17.6 32.2 13.75	131	2.67	2.8
		0.02	39.8 13.7 22.84	126		3.2

Table 3. Select Structural Parameters for Complex **2**.

Compound	Formula	out of plane μ_3-O^{-2}	Mn-N-O-Mn torsion angle (deg.)	Mn^{III}-N_3-Mn^{II} angle (deg.)
2	$[Mn_{13}Na_9O_4(EtO\text{-}salox)_{12}(N_3)_6(MeOH)_9(H_2O)_7Cl_3]_\infty$	0.181	12.01	110
		0.02	16.6 8.53 21.67	

Mn_3^{III} triangles arranged around a central Mn_3^{III} which are related by a C_3 axis. The asymmetric unit of complex **2**, as depicted in Figure 4, consists of 1/3 of the molecule, the rest of the molecule being related by the C_3 axis. The C_3 symmetric central triangle is composed of three Mn^{III} ions bound by a μ_3-O^{2-}, three μ_3–η^1:η^1:η^2:η^2 oximate ligands, three axially coordinated water molecules, and three axially coordinated μ_2–η^1:η^1 azides. The azides are axially coordinated to the Mn^{III} ions (forming the Jahn-Teller axes) and bridge a tetrahedrally coordinated Mn^{II} ion with a terminal water molecule. A C_3 axis contains the Mn^{II} ion and the central μ_3-O^{2-}. The central μ_3-O^{2-} of complex **2** deviates from the plane of the Mn^{III} ions by 0.18 Å. The oximate ligands are only slightly out of plane, resulting in Mn(5)-N(4)-O(15)-Mn(5') torsions angles of $\theta = 12^o$. A water molecule is axially coordinated to each of the Mn^{III} ions on the "lower face" of the triangle. The Mn(5)-O(13) bond distance of 2.4 Å suggests that the water molecules are weakly associated with the Mn^{III} ions. The Mn^{III}-N_{azide}-Mn^{II} bond angle, Mn(5)-N(5)-Mn(4), is $\theta = 110^o$. The Mn^{III}-N_{azide} and N_{azide}-Mn^{II} bond distances, Mn(5)-N(5) and N(5)-Mn(4), are 2.3 Å and 2.1 Å, respectively. Six coordinate Na^I ions bridge adjacent triangles by coordinating to the ethoxy, phenolate, and oximate oxygens of ligands from two different triangles. The plane of the adjoining Mn^{III}_3 triangle forms an angle of 119^o relative to the plane of the central Mn^{III} triangle. The external Mn^{III}_3 triangles have the same μ_3-O^{2-} and three μ_3–η^1:η^1:η^2:η^2 oximate ligands. Two methanols and a chloride are axially coordinated to the "upper face" of the triangle. An azide, a water molecule, and a methanol fill out the axial coordination sites of the Mn^{III} ions of the "lower face" of the triangle. Intramolecular hydrogen bonding occurs between the chlorides and hydroxide

protons of two methanols of the upper faces at distances of 3.1 Å and 3.0 Å, respectively. H-bonding also occurs between the coordinating nitrogen of the bent azide on the lower face and the methanol and water molecule at distances of 3.0 Å and 2.8 Å, respectively. These building blocks form an extended structure by sodium bridging between two "outer" triangles. The bridging sodium ions have the same coordination environment as the sodium ions of the inner-unit. The planes formed by the two outer triangles intersect at an angle of approximately 117^{o}. The obtuse angle at which the triangles join results in a helical propagation of the structure along the a, b, and c axes. By the high crystal symmetry, the extended structure is equivalent in the direction of the a, b, and c axes.

4.3.3 DC Susceptibility

Dc susceptibility measurements were made on well ground polycrystalline samples of complexes **1** and **2** in applied fields of 0.01, 0.1, and 1.0 T in a temperature range of 1.8-300 K. The samples were restrained in eicosane to prevent torqing in the applied field. Magnetization data, plotted as $\chi_M T$ vs. T, for complexes **1** and **2** are shown in Figures 7 and 8.

For complex **1** in a field of 0.01 T, $\chi_M T$ begins at 26.2 cm^3 mol^{-1} K at 300 K. $\chi_M T$ decreases steadily with decreasing temperature until approximately 20 K where $\chi_M T$ begins to slowly rise to a local maximum of 12.14 cm^3 mol^{-1} K before rapidly decreasing to a value of 4.48 cm^3 mol^{-1} K at 1.79 K. $\chi_M T$ at 300 K is significantly smaller than the spin only value of 36.01 cm^3 mol^{-1} K for 12 non-interacting Mn^{III} ion. $\chi_M T$ vs. T behavior for complex **1** in fields of 0.1 and 1.0 T follows the same trend as a 0.01 T field.

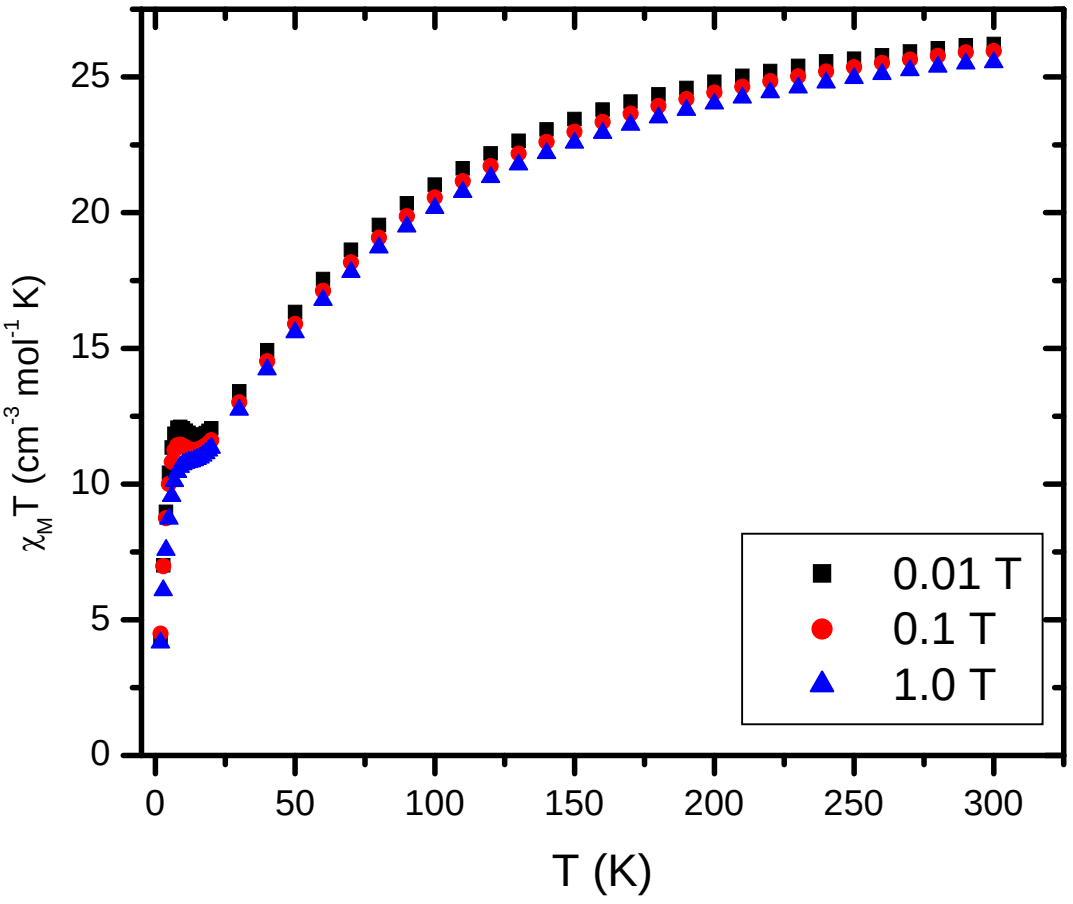

Figure 7. Plot of DC magnetic susceptibility of $[Mn_{12}{}^{III}O_4(salox)_{12}(N_3)_4(H_2O)_2(MeOH)_6]$ (**1**).

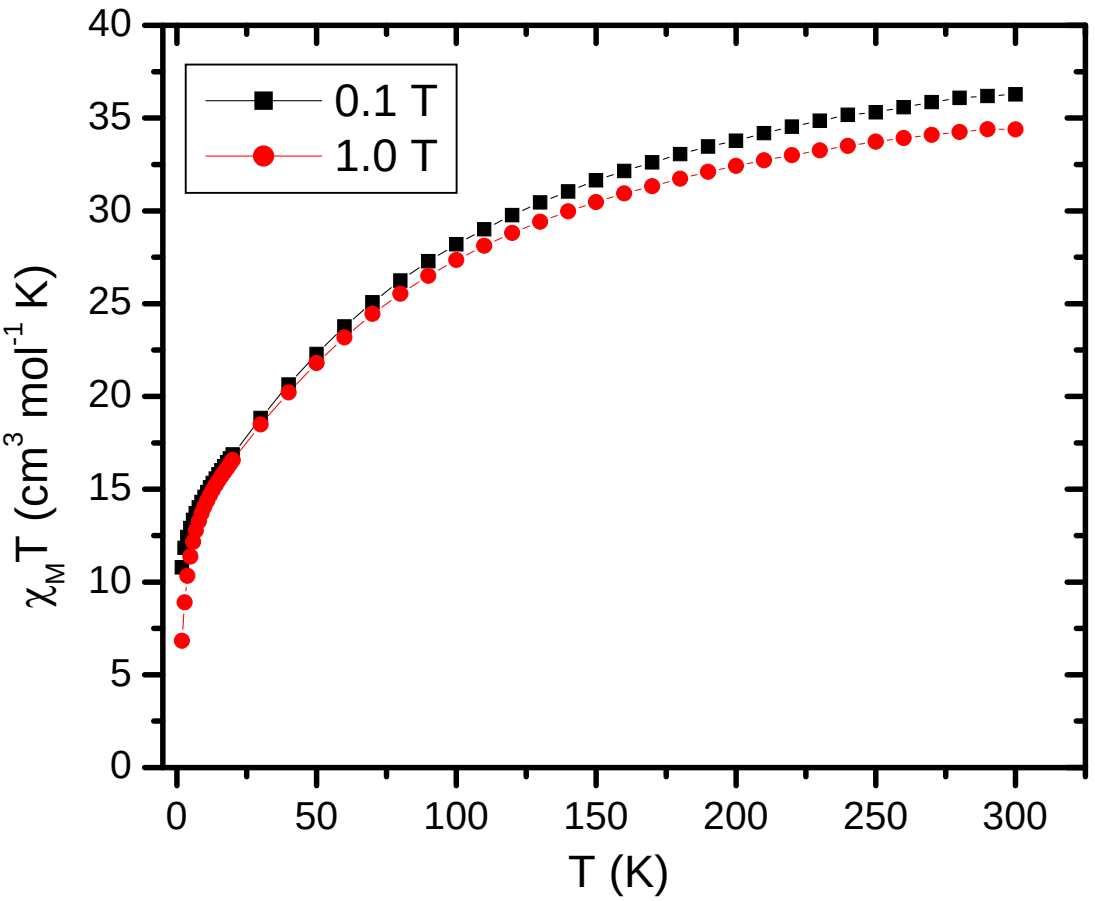

Figure 8. Plot of DC magnetic susceptibility of $[Mn^{II}Mn_{12}{}^{III}Na_6O_4(EtO\text{-}salox)_{12}(N_3)_9Cl_3(H_2O)_7(MeOH)_6]_\infty$ (**2**).

For complex **1** in a 0.1 T field, $\chi_M T$ begins at 25.96 cm^3 mol^{-1} K and decreases with decreasing temperature until 13.9 K where $\chi_M T$ begins to rise to a local maximum of 11.45 cm^3 mol^{-1} K at 8.8 K before decreasing rapidly to a minimum of 4.48 cm^3 mol^{-1} K at 1.8 K. In a field of 1.0 T, $\chi_M T$ begins at 25.55 cm^3 mol^{-1} Kat 300 K and decreases with decreasing temperature until it rises to a local maximum of 10.77 cm^3 mol^{-1} K at 9.0 K before decreasing rapidly to 4.16 cm^3 mol^{-1} K at 1.79 K. The small rise at approximately 9 K is indicative of very weak magnetic ordering. The complex forms one-dimensional network by hydrogen bonding between complexes via the capping water molecule of the outer Mn^{III} triangle (O11) and the phenolate oxygen (O3) of an adjacent complex. The bond distances involved in the H-bonding network are short enough to mediate very weak magnetic exchange interactions between metal centers of neighboring complexes. Mn-N-O-Mn torsion angles range from 32° to 13.8° within the central Mn_6 core, with an average torsion angle of 20.8°. The larger torsion angle is on the borderline for mediating ferromagnetic exchange. The two smaller torsion angles clearly suggest strong antiferromagnetic exchange between the Mn^{III} ions. Exchange between triangles is mediated by the Mn-$O_{oximate}$ bond. The Mn-$O_{oximate}$ bond distance of 2.48 Å is in between ferromagnetic and antiferromagnetic exchange. Torsion angles in the outer triangles range from 38.8° to 13.7°. The larger torsion angle indicates strong ferromagnetic exchange between the two Mn^{III} ions. Exchange between inner and outer triangles is mediated by the bridging azides and the bridging Mn-$O_{oximate}$ bond. The bond angles of the μ_2-η^1,η^1 azides are in excess of 120°. Bridging azides with such large bond angles are known to mediate strong antiferromagnetic exchange between metal centers.[16] The Mn-$O_{oximate}$ bond distance of 2.37 Å is in the range of mediating ferromagnetic exchange.

In complex **2**, magnetic exchange between triangles is mediated by the bridging sodium ions. Because exchange is propagated through four diamagnetic ions, the magnetic exchange will be very weak. Therefore, the central and outer Mn_3^{III} triangles can be treated as magnetically isolated units. Magnetic susceptibility measurements can be considered the average of the two building blocks. For complex **2** in a field of 0.1 T at 300 K, $\chi_M T$ begins at a value of 35.3 cm^3 mol^{-1} K and decreases steadily with decreasing temperature until it reaches a $\chi_M T$ value of 10.0 cm^3 mol^{-1} K at approximately 60 K. $\chi_M T$ then decreases more rapidly until it reaches a minimum of 10.5 cm^3 mol^{-1} K at 1.79 K. $\chi_M T$ at 300 K is less than the spin only value of 40.4 cm^3 mol^{-1} K for 12 noninteracting Mn^{III} ions and one Mn^{II} ion which indicates antiferromagnetic exchange within the complex. $\chi_M T$ for complex **2** in a 1.0 T field follows similar behavior; at 300 K $\chi_M T$ begins at a value of 34.3 cm^3 mol^{-1} K and steadily decreases until reaching a minimum value of 6.92 cm^3 mol^{-1} K at 1.79 K. The oximate moiety of the central triangle is almost planar, with Mn-N-O-Mn torsion angles of approximately 12^o. This would suggest strong antiferromangetic exchange between Mn^{III} ions of the triangle. The Mn^{III}-N_{azide}-Mn^{II} bond angle is close to 110^o, which is in the range of mediating weak ferromagnetic exchange. The "outer" triangles have three unique oximate torsion angles of 8.6^o, 21.7^o, and 16.6^o which also indicate antiferromagnetic exchange between Mn^{III} ions.

The nature of the spin ground state and the zero-field-splitting term D, were probed through the reduced magnetization experiment in which high magnetic fields of 1-

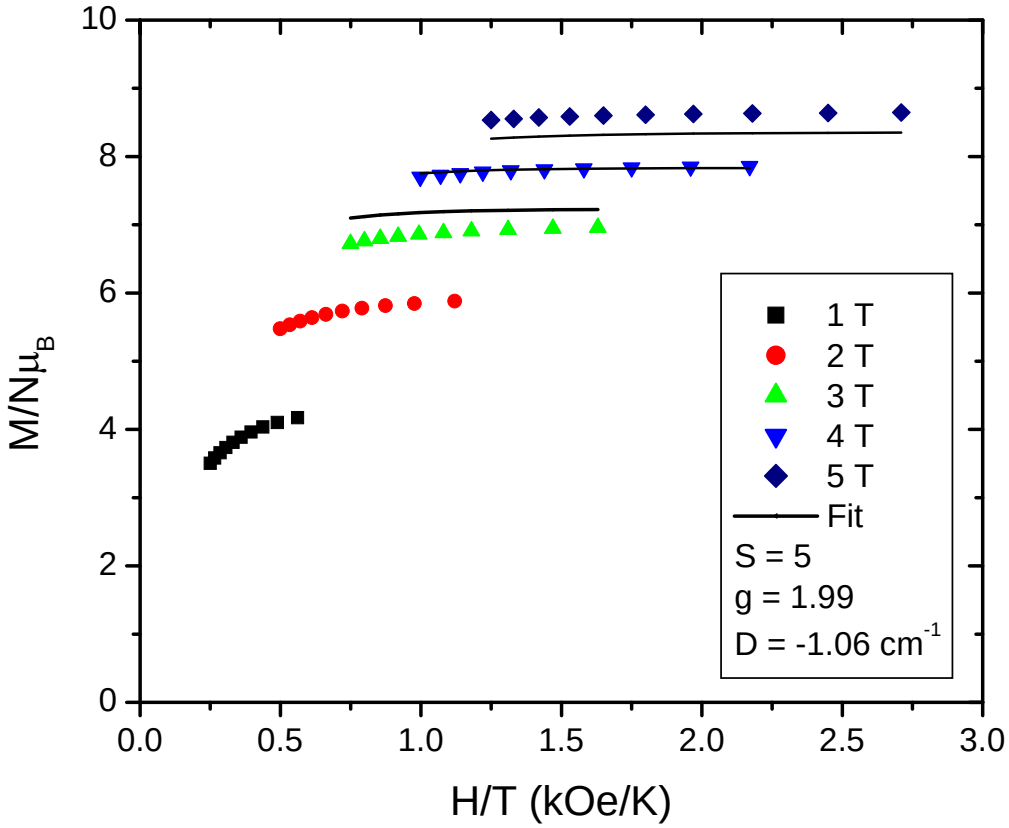

Figure 9. Plot of reduced magnetization of $[Mn_{12}{}^{III}O_4(salox)_{12}(N_3)_4(H_2O)_2(MeOH)_6]$ (**1**).

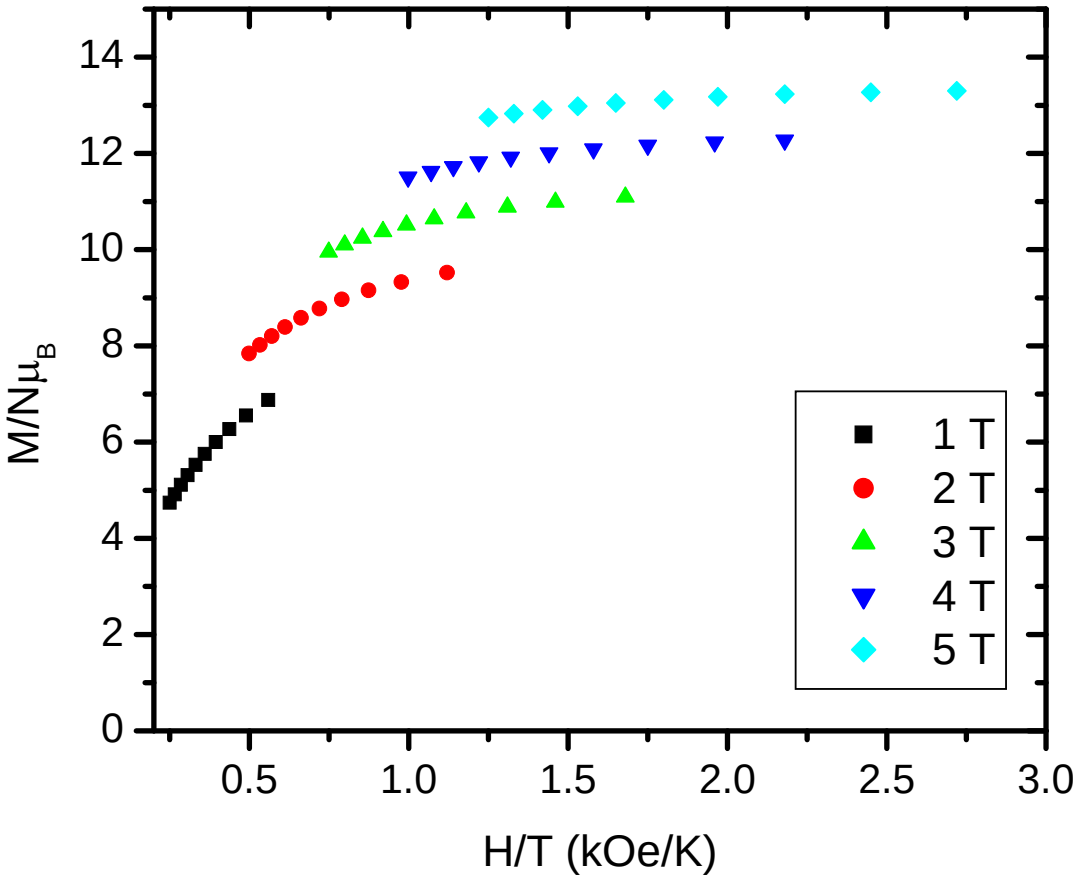

Figure 10. Plot of reduced magnetization of $[Mn^{II}Mn_{12}{}^{III}Na_6O_4(EtO\text{-}salox)_{12}(N_3)_9Cl_3(H_2O)_7(MeOH)_6]_\infty$ (**2**).

5 T are applied in a temperature range of 1.8-4.0 K. The data were fit using AXFIT which assumes a well isolated spin ground state and incorporates a full power average. The data is presented as plots of magnetization versus field in Figures 9 and 10 for complexes **1** and **2**, respectively.

Reduced magnetization for complex **1** saturates at approximately 9 $M/N\mu_B$ in a field of 5 T which suggests a spin ground state of either S = 4 or S = 5 for g = 2.00. A poor fit of 3-5 T reduced magnetization data was obtained with fit parameters of S = 5, g = 1.99, and D = -1.06 cm^{-1}.

Reduced magnetization for complex **2** saturates at approximately 13 $M/N\mu_B$ which is close to a S = 13/2 for gS for g = 2.00. Attempts at fitting reduced magnetization data for complex **2** were unsuccessful. However, complex **2** exhibits non-superimposable isofields which is indicative of a nonzero D.

4.3.4 AC Susceptibility

In order to ascertain the kinetic behavior of complexes **1** and **2**, that is, to determine the effective barrier to reversal of magnetization, U_{eff}, alternating-current (ac) magnetic susceptibility experiments were performed. Polycrystalline samples locked in eicosane were placed in zero applied dc field with a 3 Oe field oscillating at frequencies of 10, 25, 50, 100, 250, 500, 750, or 997 Hz in a temperature range of 1.8-7.0 K. The in-phase (χ_M') and out-of-phase (χ_M") components of the ac magnetic susceptibilities of complexes **1** and **2** are plotted versus temperature in Figures 11 and 12. The energy barrier (U_{eff}) can be measured by applying the Arrhenius equation to ac susceptibility data.

$$\ln(1/\tau) = \ln(1/\tau_o) - U_{eff}/kT \qquad (4.1)$$

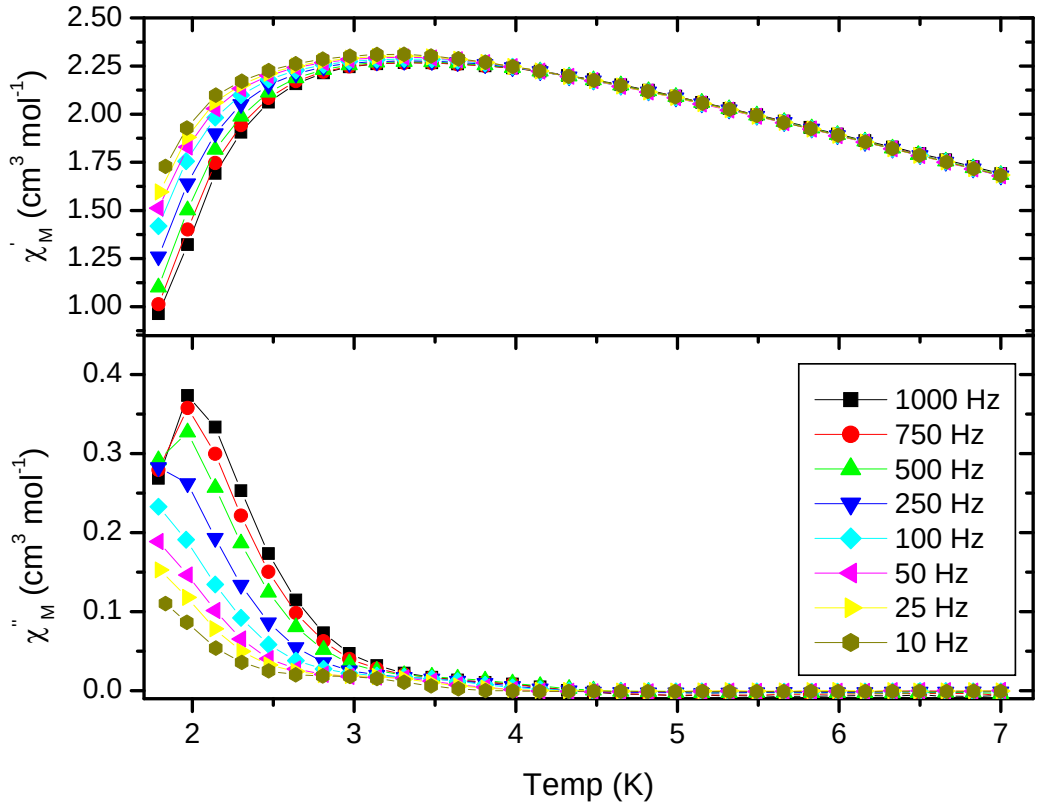

Figure 11. Plot of ac susceptibility of $[Mn_{12}{}^{III}O_4(salox)_{12}(N_3)_4(H_2O)_2(MeOH)_6]$ (**1**). Lines serve as guides for the eye.

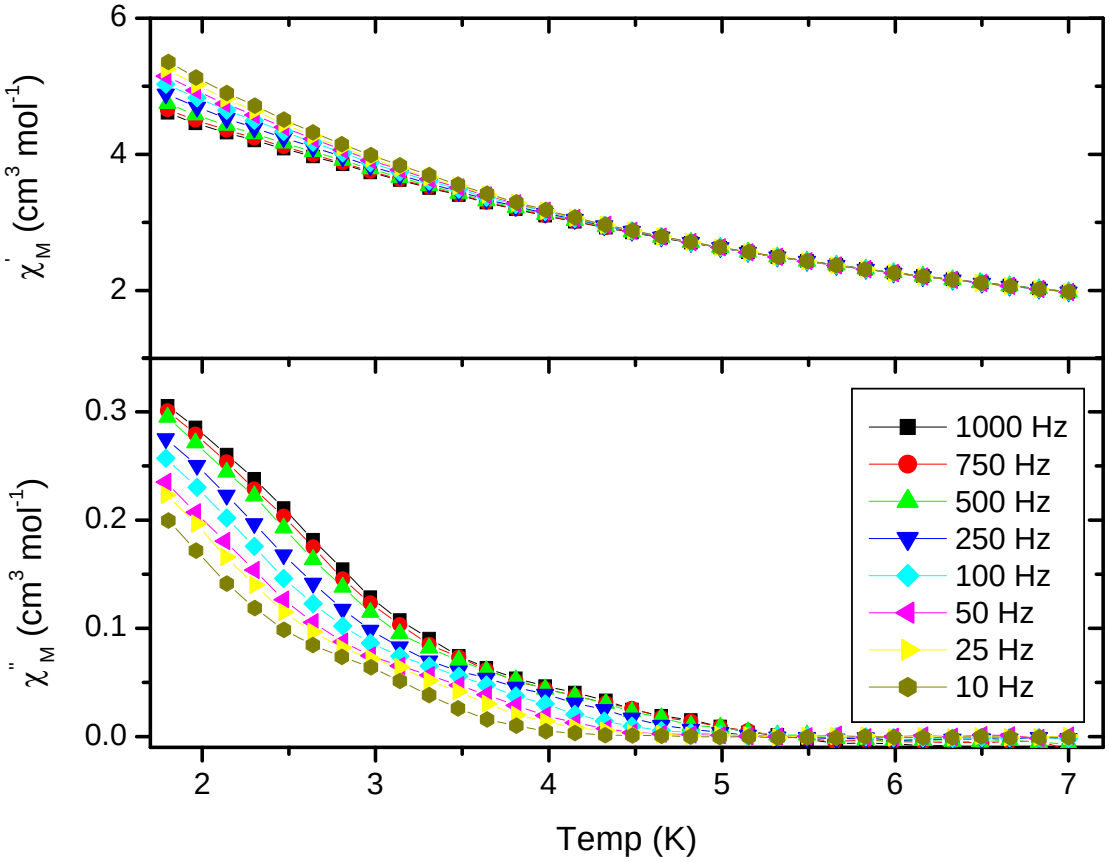

Figure 12. Plot of ac susceptibility of $[Mn^{II}Mn_{12}{}^{III}Na_6O_4(EtO\text{-}salox)_{12}(N_3)_9Cl_3(H_2O)_7(MeOH)_6]_\infty$ (**2**). Lines serve as guides for the eye.

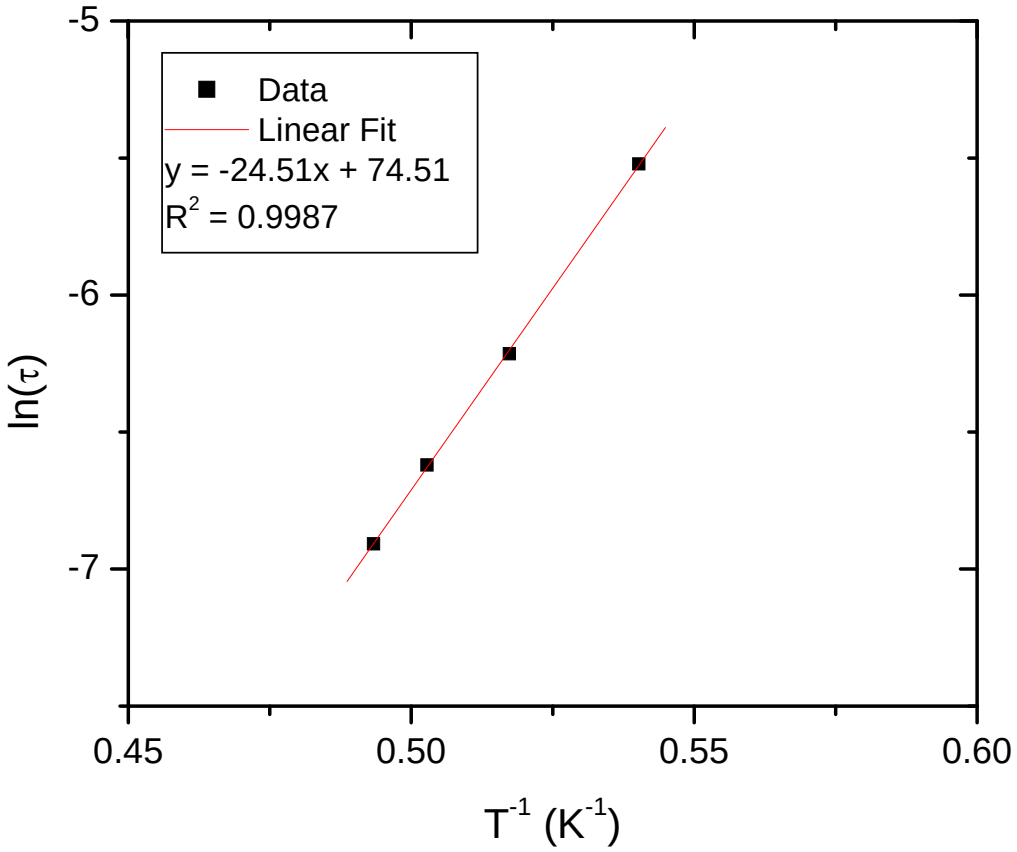

Figure 13. Arrhenius plot of ac susceptibility data for $[Mn_{12}{}^{III}O_4(salox)_{12}(N_3)_4(H_2O)_2(MeOH)_6]$ (**1**).

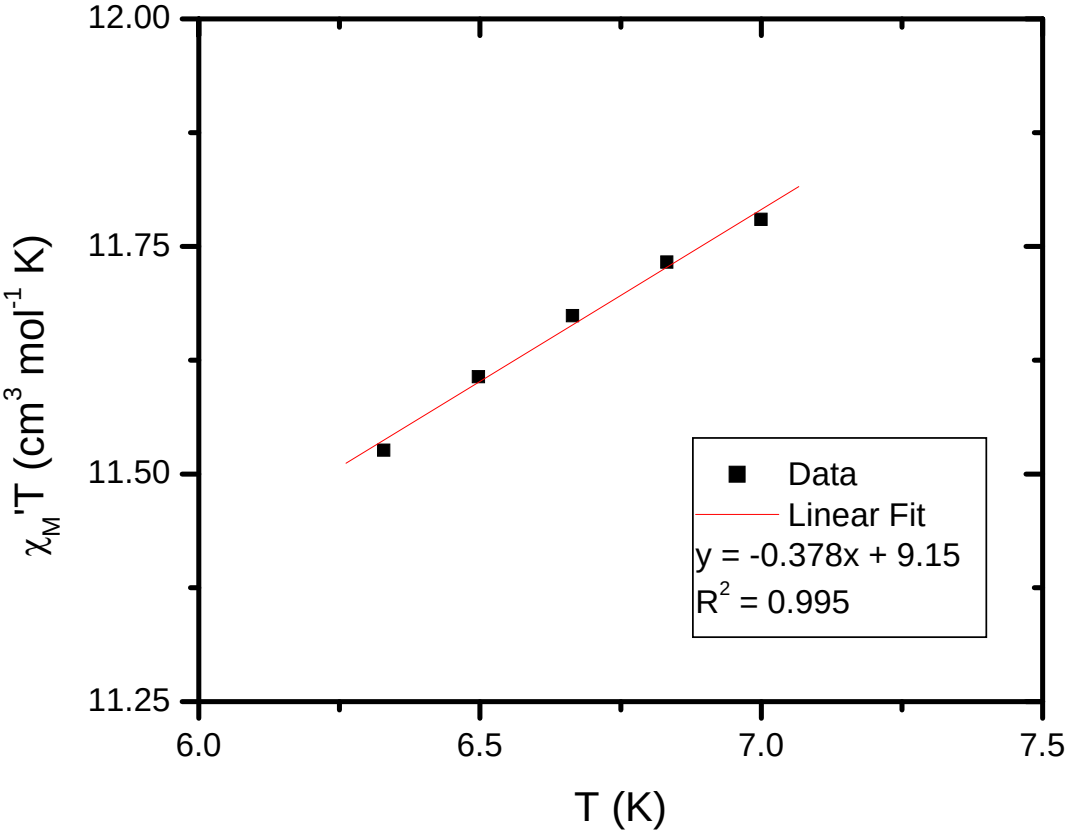

Figure 14. Plot of χ_M'T versus T extrapolated to 0 K for complex **1**.

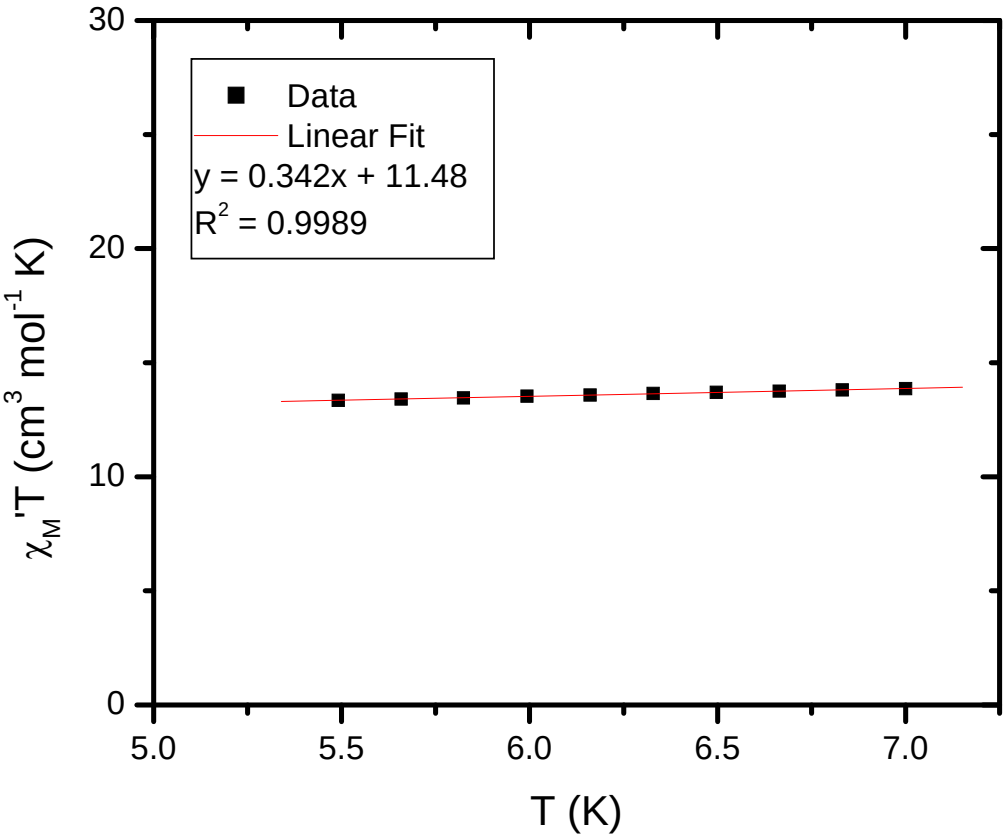

Figure 15. Plot of χ_M'T versus T extrapolated to 0 K for complex **2**.

U_{eff} is obtained by calculating the slope of an Arrhenius plot constructed from the out-of-phase susceptibility data.

The in-phase component of complex **1** increases linearly with decreasing temperature until approximately 4 K, at which point it begins to curve downward to zero K. The out-of-phase component does not exhibit much of a frequency dependence between the frequencies of 997-500 Hz. A fit of the out-of-phase component yielded an effective barrier, U_{eff} = 21.5 K. The linear portion of the in-phase component was plotted as $\chi_M T'$ vs temperature and extrapolated to 0 K, as shown in Figure 16. The resulting $\chi_M T'$ is 9.15 cm^3 mol^{-1} K which is close to the spin only value for an S = 4 system. This value is in close agreement with the spin ground state obtained from the reduced magnetization experiment.

The in-phase component of complex **2** increases almost linearly with decreasing temperature from 7.0 K until approximately 4.8 K after which it increases in a more rapid fashion. The out-of-phase ac signal χ_M", while not reaching a low enough temperature to exhibit a peak, does exhibit a frequency dependence. In many cases this frequency dependence of χ_M " is taken as a signature of SMM behavior. The linear portion of the in-phase susceptibility was plotted as $\chi_M T'$ versus temperature and extrapolated to 0 K (Figure 15). A value of 11.5 cm^3 mol^{-1} K was obtained which is close to an S = 9/2 from the spin only formula.

4.3.5 Thermal and Structural Stability

The thermal stability of complex **2** was assessed using thermogravimetric analysis. Thermogravimetric analysis was performed on single crystals of complex **2** by heating the sample in a temperature range of 25-600 ^oC. The sample mass was monitored

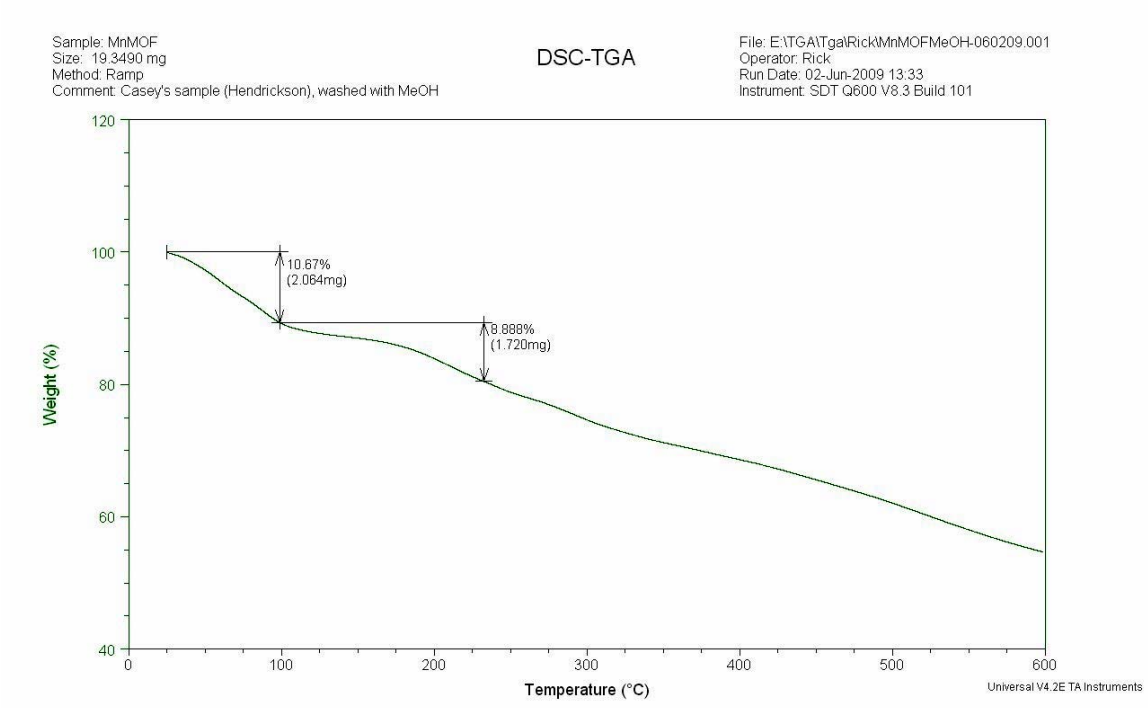

Figure 16. TGA trace for complex **2** in a 25 to 600^{o}C at a scan rate of 5^{o}C/min

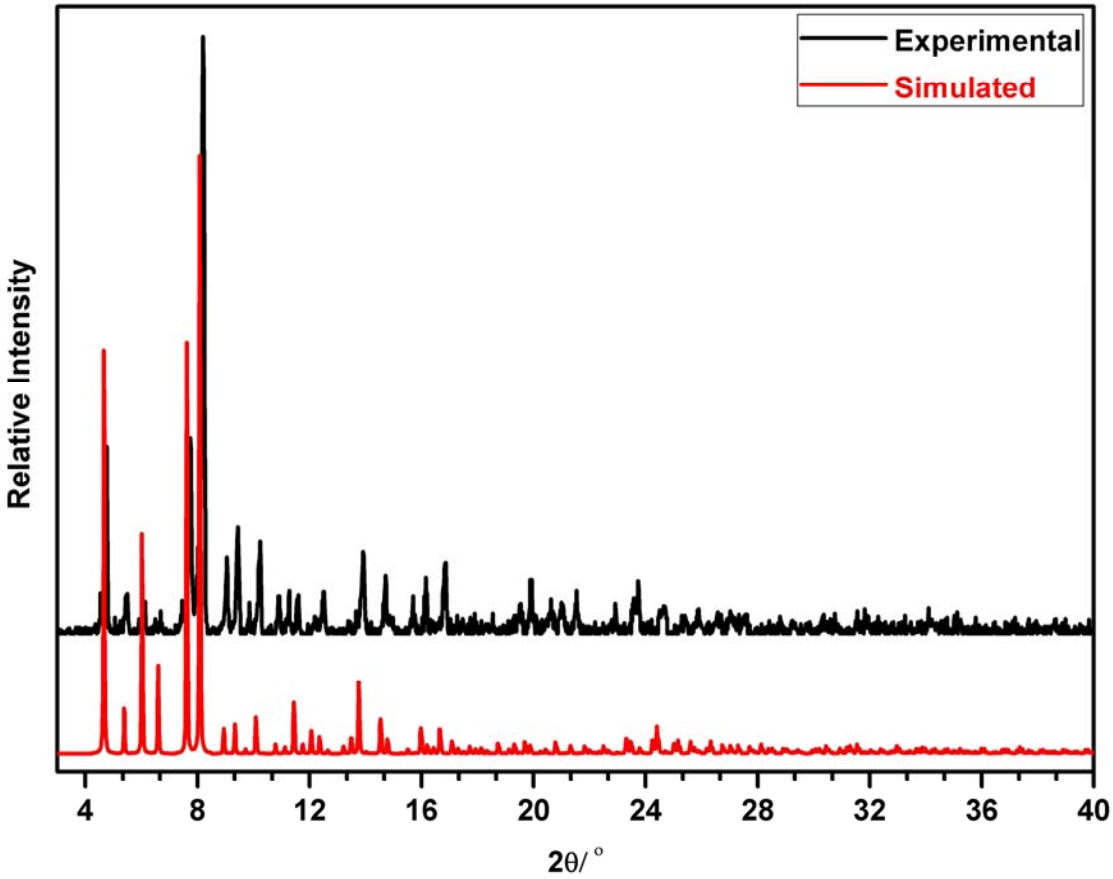

Figure 17. PXRD spectrum for complex **2** performed on a solvated sample.

over the course of the heating period. Data are presented as percent mass versus temperature in Figure 16.

The sample looses approximately 45% of its mass over the course of the measurement. Approximately 10% of the sample mass is lost between 25°C and 100°C which corresponds to the evaporation of water and methanol from the lattice (coordinated solvent comprises 9.5% of the molecular weight of the complex). Between 100 and 230 °C the sample looses an additional 9% of its mass. It is unclear what this mass loss can be attributed too, however one possibility is the coordinated azides, which are thermally unstable, may have decomposed in to N_2. Above 230°C the complex looses all thermal stability and decomposes at almost linear rate.

Bulk crystallinity was verified by PXRD measurements (Figure 17) before desolvating the samples. The large peaks at small values of 2θ indicate large distances between miller planes, which is consistent with the large unit cell parameters. The simulated spectrum closely matches the experimental spectrum at lower values of 2θ.

4.3.6 Gas Adsorption Measurements

The gas adsportion properties of complex **2** were evaluated by volumetric gas adsorption measurements using nitrogen, hydrogen, argon, and carbon dioxide gasses. All gas adsorption measurements were made on crystalline samples of **2** had been placed under vacuum with heating at 105°C. The resulting isotherms are presented in a combined plot in Figure 18.

Complex **2** did not adsorb a significant amount N_2 at pressures up to 1.0 bar at a temperature of 77 K. The adsorption curve for H_2 indicated weak up-take at 77 K and 1.1 bar. Gas adsorption improved significantly when Ar and CO_2 were used. It should be

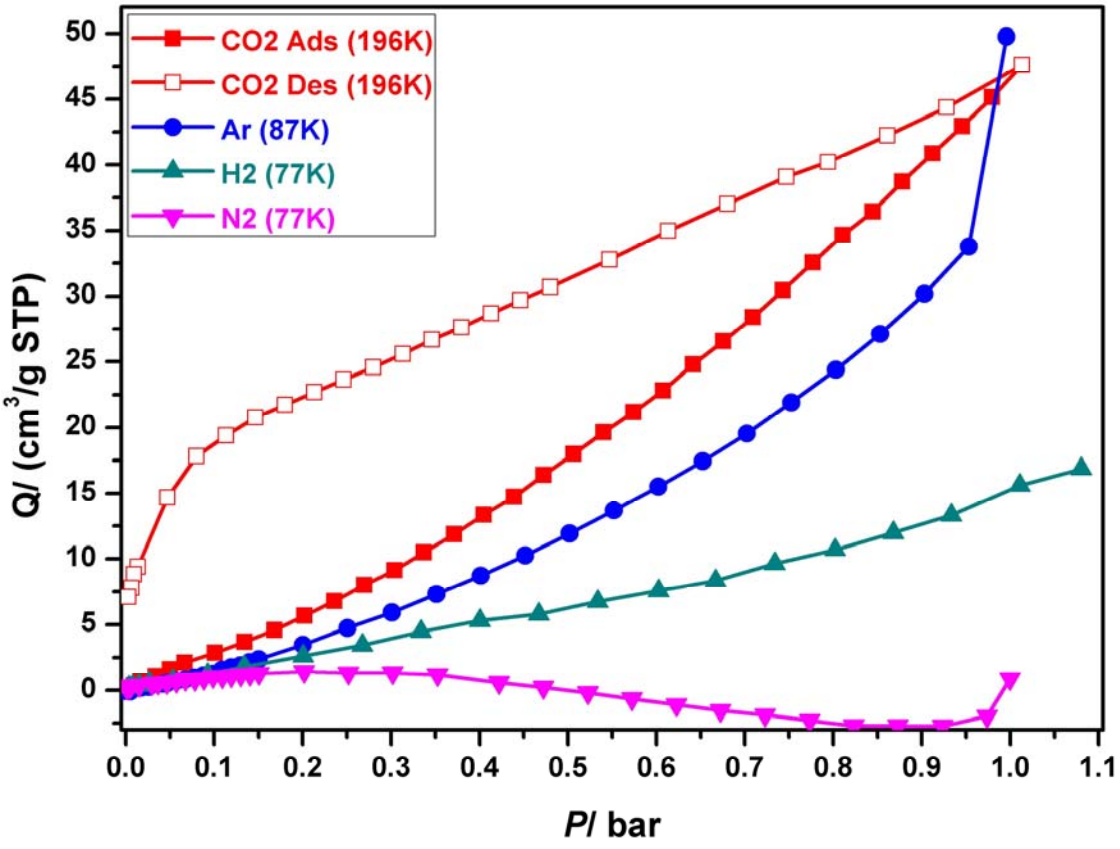

Figure 18. Gas adsorption isotherms for complex **2**.

noted that adsorption measurements with Ar and CO_2 were performed at higher temperatures of 87 K and 196 K, respectively. Adsorption of argon becomes more appreciable at higher pressures. The openings into the pores of complex **2** are very narrow, approximately 3.5 Å in diameter. Furthermore, **2** most likely has more flexibility than the more typical MOFs. Higher temperatures and pressures might be required to distort the cavity enough to enable the gas to diffuse into the cavity. CO_2 exhibits a hysteretic adsorption/desorption curve.[17] CO_2 has a larger dipole moment than Ar, so there could be a stronger interaction with the framework. Another possibility is that the much higher temperatures used during the CO_2 adsorption measurement might have resulted in larger distortion of the pores, enabling a larger volume of gas to diffuse into the pores.[17] As the pressure is lowered the gas becomes trapped and desorbs at a slower rate.

To summarize, based on its structural characteristics complex **2** is a MOF. The preliminary gas adsorption data indicates behavior that has been exhibited in only one other reported complex.[18] Gas adsorption measurements need to be repeated at higher temperatures and pressures in order to verify the effect pressure and temperature has on the framework in addition to vapor diffusion measurements using molecules with large dipole moments.

4.4 Conclusion

Two unique complexes are reported in this work. Complex **1** is an extension of work from Chapter III in which azide was used to bridge Mn^{II} ions to the faces of a Mn_6^{III} core. In this instance azide is used to couple Mn_3 triangles to the faces of a Mn_6 core. The axial coordination sites of the outer triangles of complex **1** are occupied with solvent

molecules. The addition of a bridging ligand could result in a network of interconnected Mn_{12}^{III} units. $\chi_M T$ behavior and structural geometry suggest dominant antiferromagnetic exchange within **1**. $\chi_M T$ behavior at low temperatures indicate the presence of magnetic ordering, possibly due to the one dimensional hydrogen bonding network. A poor least-squares fit of the 3-5 T reduced magnetization data gave parameters of an S = 5 spin ground state and a D value of -1.06 cm^{-1}. Extrapolation of the in-phase component of ac susceptibility data at a frequency of 10 Hz plotted as χ_M'T vs T suggested a spin ground state of S = 4 which is close to the spin ground state obtained from the fit of reduced magnetization data.

The use of a modified salicylaldoxime in the synthesis of oxime stabilized Mn_3^{III} triangles lead to the formation of a three dimensional porous material. The gas adsorption properties of complex **2** were verified in adsorption measurements with N_2, H_2, Ar, and CO_2. Complex **2** exhibited greater adsorption with larger gases including a hysteretic binding curve for CO_2. However, it is unclear if this is due to the higher experimental temperatures used in measurements with Ar and CO_2 or if there is a preferential interaction with the framework because of the small pore size or open coordination sites of the Mn^{III} ions. Further gas adsorption measurements at higher temperatures and pressures and/or gas adsorption measurements with molecules with large dipole moments such as alcohols are necessary to determine if the hysteretic behavior with CO_2 is the results of a temperature induced phase transition where the pores open up significantly or if it is the result of interactions with the framework.

The magnetic behavior of complex **2** is the result of contributions from two distinct units: the central C_3 symmetric $Mn^{II}Mn_3^{III}$ core and the outer C_1 symmetric Mn_3^{III}

triangles. This makes fitting magnetic susceptibility data using current models difficult. Reduced magnetization exhibited non-superimposible isofields indicating the presence of a nonzero D value, and saturates at a value close to 13 $M/N\mu_B$ suggesting a S = 13/2 ground state. Extrapolation of the in-phase component to zero K suggests a S = 9/2 ground state. Determination of a frequency dependent out-of-phase signal was inconclusive as the peak centers of the out-of-phase component were outside of the temperature range studied (i.e. below 1.8 K).

References

1. Sessoli, R.; Gatteschi, D.; Caneschi, A.; Novak, M. A., Magnetic Bistability in a Metal-Ion Cluster. *Nature* **1993,** 365, (6442), 141-143.

2. Christou, G.; Gatteschi, D.; Hendrickson, D. N.; Sessoli, R., Single-molecule magnets. *Mrs Bulletin* **2000,** 25, (11), 66-71

3. del Barco, E.; Kent, A. D.; Hill, S.; North, J. M.; Dalal, N. S.; Rumberger, E. M.; Hendrickson, D. N.; Chakov, N.; Christou, G., Magnetic quantum tunneling in the single-molecule magnet Mn-12-acetate. *Journal of Low Temperature Physics* **2005,** 140, (1-2), 119-174.

4. Stamatatos, T. C.; Foguet-Albiol, D.; Stoumpos, C. C.; Raptopoulou, C. P.; Terzis, A.; Wernsdorfer, W.; Perlepes, S. P.; Christou, G.; Initial Example of a Triangular Single-Molecule Magnet from Ligand Induced Structural Distortion of a [MnIII3O]7+ Complex, *Journal of the American Chemical Society*, **2005**, 127, 15380-15381.

5. Stamatatos, T. C.; Foguet-Albiol, D.; Lee, S. C.; Stoumpos, C. C.; Raptopoulou, C. P.; Terzis, A.; Wernsdorfer, W.; Hill, S. O.; Perlepes, S. P.; Christou, G. "Switching on" the Properties of Single-Molecule Magnetism in Triangular Manganese(III) Complexes, *Journal of the American Chemical Society,* **2007**, *129*, 9484–9499.

6. C. J. Milios, A. Vinslava, Wernsdorfer, W.; Moggach, S.; Parsons, S.; Perlepes, S. P.; Ghristou, G.; Brechin, E. K. A record anisotropy barrier for a single-molecule magnet *Journal of the American Chemical Society* **2007** 129, 10, 2754-2755.

7. Cano, J.; Cauchy, T.; Ruiz, E.; Constantinos, J M; Constantinos, C.; Stoumpos, C.; Stamatatos, C.; Spyros, P. P.; Christou, G.; Brechin, B. K. On the origin of ferromagnetism in oximato-based [Mn3O]7+ triangles. *Dalton* **2008** 234-240.

.8. Milios, C. J.; Piligkos, S.; Brechin, E. K. Ground state spin-switching via targeted structural distorsion: twisted single-molecule magnets from derivatised salicyaldoximes *Dalton* **2008**, 1809-1817.

9. Rowsell, J. L. C.; Yaghi, O. M., Metal-Organic Frameworks: A New Class of Porous Materials, *Microporous Mesoporous Mater.*, **2004**, *73*, 3-14

10. Rowsell, J. L. C.; Millward, A. R.; Park, K. S.; Yaghi, O. M. Hydrogen Sorption in Functionalized Metal-Organic Frameworks, *J. Am. Chem. Soc.*, **2004**, *126*, 5666-5667.

11. Sudik, A. C.; Ockwig, N. W.; Millward, A. R.; Côté, A. P.; Yaghi, O. M. Design, Synthesis, Structure, and Gas (N_2, Ar, CO_2, CH_4 and H_2) Sorption Properties of Porous Metal-Organic Tetrahedral and Heterocuboidal Polyhedra, *J. Am. Chem. Soc.*, **2005**, *127*, 7110-7118.

12. Achmann, S.; Hagen, G.; Kita, J.; Malkowsky, I. M.; Kiener, C.; Moos, R., Metal-Organic Frameworks for Sensing Applications in the Gas Phase, *Sensors* **2009**, 9, 1574-1589.

13. Kurmoo, Mohamedally, Magnetic metal-organic frameworks, *Chemical Society Reviews,* **2009**, 38, 1353-1379.

14. Stokker, G. PREPARATION OF 1,2-BENZISOXAZOLES FROM SALICYLALDOXIMES VIA TRICHLOROACETYL ISOCYANATE*, Journal of Organic Chemistry* **1983**, *48*, 2613–2615.

15. Carlin, R. L., *Magnetochemistry*. Springer-Verlag: New York, 1986.

16. Zeng, Y. F.; Hu, X.; Liu, F. C.; Bu, X. H. Azido-mediated systems showing different magnetic behaviors. *Chemical Society Reviews*, **2009**, 38, 469-480.

17. Ferey, G.; Serre C., Large breathing effects in three-dimensional porous hybrid matter: facts, analyses, rules and consequences, *Chemical Society Reviews*, **2009**, 1380-1399.

18. Kim, H.; Samsonenko, D. G.; Minyoung Y.; Yoon, J. W.; Hwang, Y. K.; Chang, J. S.; Kim K., Temperature-triggered gate opening for gas adsorption in microporous manganese formate, *Chemical Communications*, **2008**, 4697-4699.

Chapter Five

Synthesis of a Salicyaldehyde Functionalized Fullerene

5.1 Introduction

Single-molecule magnets (SMMs) represent a bottom-up approach in the synthesis and characterization of nanoscale magnetic devices.[1] In particular, they present an opportunity to discover new chemical and physical phenomena at the nanoscale and in their subsequent use in device applications. They are characterized by appreciable magnetoanisotropy (D) and a large spin ground state (S_z) that leads to slow reversal of magnetization ($|D|S_z^2$).[2-4]

One of the goals of SMM research is to incorporate SMMs into nanoscale devices. It is important to first determine how SMMs interact with semiconducting or superconducting band structure. Work has been made towards placing SMMs on gold surfaces and in break-junctions.[5, 6] However, a random orientation of SMMs on a surface will lead to a distribution of microenvironments, thus leading to quantum decoherence.[7] Integrating an SMM and a conductor into a crystalline lattice would provide an ordered environment which would minimize microenvironments.

An organic conductor that is well known for conductivity and superconductivity is C_{60}.[8] C_{60} has been cocrystallized with a range of molecules with pi conjugated systems.[9, 10] However, C_{60} has poor solubility in the solvents most commonly used in SMM synthesis. Another problem with cocrystallization is that in other hybrid magnetic-conductor systems there was not a significant interaction between the two systems.[11] By chemically modifying C_{60} to possess a chelating ligand, one can overcome the problem of poor solubility and force the metal centers of the SMM to be relatively close to the

conductor. The system could then be chemically reduced to yield the C_{60}^{n-} anion, giving rise to an electrically conducting solid.

A fullerene (i.e. C_{60}) is rather large, ~0.7 nm in diameter. Sterics have to be taken into consideration so that the C_{60} does not inhibit the formation of a polynuclear cluster. Oxo-centered Mn_3^{III} triangles are ideal as they are simple SMMs which are not sterically crowded due to the molecular C_3 symmetry. Functionalized salicylaldoximes are synthesized by a condensation reaction of a salicylaldehyde derivative with hydroxyl amine, affording the oxime in high yields. The 5-position of salicylaldehyde provides an ideal position for attachment of a fullerene as it does not inhibit the formation of Mn_3^{III} triangles due to sterics.

Fullerenes have been functionalized using alkyl lithium reagents, Grignards, and with a number of cyclization reactions.[12-14] Most of these reactions are not compatible with the functional groups used in coordination chemistry and require extensive protecting group chemistry before they can be attempted. The arylation of C_{60} with rhodium catalyst provides a facile method for the coupling of salicylaldehyde with the fullerene.[15] The rhodium catalyst is stable to the functional groups of the salicylaldehyde, thus no protecting group chemistry is necessary before coupling the salicylaldehyde to the fullerene.

A salicylaldehyde functionalized fullerene has been synthesized through the rhodium catalyzed arylation of C_{60} with 3-methoxysalicyaldehyde boronic acid. It has been characterized by $^{1}H/^{13}C$ NMR and EDS mass spectrometry.

5.2 Experimental Section

All reagents were used as received from commercial sources unless otherwise noted. The rhodium catalyst $[Rh(cod)OH]_2$ was synthesized according to literature methods.[16] o-dichlorobenzene was purified by distillation under reduced pressure and stored over molecular sieves in an argon atmosphere. All procedures were carried out under an argon atmosphere using standard Schlenk line techniques. All workup and purification procedures were performed with reagent grade solvents in air.

Thin-layer chromatorgraphy was performed using Whatman silica gel coated plates (0.25mm). The developed chromatogram was analyzed by UV lamp (254 nm) and with I_2 if necessary. Flash chromatography was performed using Fischer silica gel grade 60 (230-400 mesh). Nuclear magnetic resonance (NMR) spectra were recorded on a Mercury 4 Nucleus 300 MHz spectrometer. Chemical shifts for ^1H and ^{13}C NMR are reported in ppm relative to tetramethysilane (0.0 ppm). Data are reported as chemical shifts and multiplicity (s = singlet and d = doublet). High-resolution mass spectra (HRMS) were obtained from the UCSD Mass Spectrometry Facilities (electronspray ionization mass spectrometry, ESI-MS).

5.2.1 Compound Synthesis

1-(4-methoxysalicylaldehyde)-1,9-dihydro[60]fullerene (1).

An oven-dried 250 mL Schlenk flask equipped with magnetic stir bar and rubber septum was evacuated and backfilled with argon three times. To this flask was added o-dichlorobenzene (100 mL) and H_2O (25 mL). Three freeze-pump-thaw cycles were performed before adding $[Rh(cod)OH]_2$ (14 mg, 0.03 mmol), C_{60} (220 mg, 0.31 mmol),

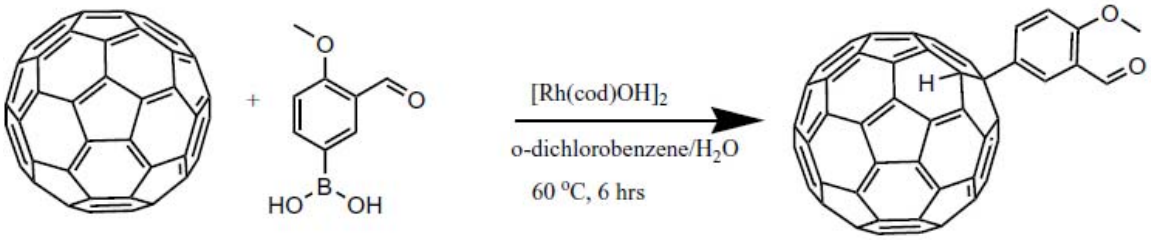

Scheme 1. Rh-catalyzed Arylation of C_{60} with 3-methoxysalicylaldehyde boronic acid

and 3-methoxysalicylaldehyde boronic acid (68 mg, 0.37 mmol) under a stream of argon. The mixture was warmed to 60^{o}C in a silicon oil bath and stirred for 6 hours. Overtime, the solution changed color from a rich purple to dark brown. The solution was cooled to room temperature and passed through a short plug of silica gel using toluene (150 mL) as an eluent. o-dichlorobenzene was removed by vacuum distillation with heating from a 90^{o}C water bath. The brown residue was concentrated under reduced pressure before being loaded onto a silica gel column (10 cm diameter x 25 cm tall) and eluted with toluene. The product was recovered as a brown solid in 22% yield (58 mg, 0.07 mmol). R_f (toluene) = . ^{1}H NMR (300 MHz, CS_2:$CDCl_3$ = 1:1) ppm 4.12 (s, 3H), 6.67 (s, 1H), 7.42 (d, 1H), 8.69 (d, 1H), 8.86 (s, 1H), 10.69 (s, 1H). ^{13}C NMR (300 MHz, CS_2/$CDCl_3$ = 1:1) ppm 56.32, 63.92, 113.44, 127.6, 135.2, 142.9, 146.7, 152.6, 153.5, 176.6, 189.9. HRMS (ESI, negative) *m/z* calc $C_{68}H_7O_2$: 855.78 (±0.007) [M-H]- found 855.13.

5.3 Results and Discussion

5.3.1 Discussion of Synthesis

1 was synthesized in low yield by rhodium catalyzed arylation of C_{60} with salicylaldehyde boronic acid. The $[Rh(cod)OH]_2$ catalyzed reaction was not as selective as hoped. Multiple side products formed over the course of the reaction and little C_{60} was recovered (15%). This might indicate that the rhodium catalyst is too reactive. A less reactive species such as the $[Rh(cod)MeCN]BF_4$ analogue might result in better yields.

1 was characterized by $^{1}H/^{13}C$ NMR and ESI mass spectrometry. ^{1}H and ^{13}C NMR Spectra are found in Figures 1 and 2. The ^{1}H spectrum of **1** is easily assigned as the complex contains very distinct protons. The single at 4.12 ppm which integrates for 3 protons corresponds to the protons of the methoxy group. The singlet at 6.67 ppm integrates for a single proton and can be attributed to the proton on the fullerene. As the fullerene is quite electron withdrawing, the phenyl protons closest to the fullerene are shifted further downfield. The doublets at 7.42 and 8.69 ppm correspond to the protons on carbons at the 5 and 6 position of the phenyl ring, respectively. The peak at 8.86 ppm corresponds to the lone phenyl proton ortho to the aldehyde group (carbon 2). Finally, the aldehyde proton is found as a singlet at 10.69 ppm. ^{13}C spectrum is more difficult to assign. As a result of the icosahedral symmetry of C_{60}, the ^{13}C spectrum of C_{60} consists of only one peak at 143 ppm (relative to TMS). Functionalizing the fullerene with methoxysalicyaldehyde reduces the molecular symmetry to C_1. The reduction in symmetry results in a number of peaks between 153 and 142 ppm attributed to the in-equivalent carbons of the fullerene. Carbons adjacent to phenol groups tend to have chemical shifts around 150 ppm; two peaks reside at 152 and 153 ppm but it is difficult

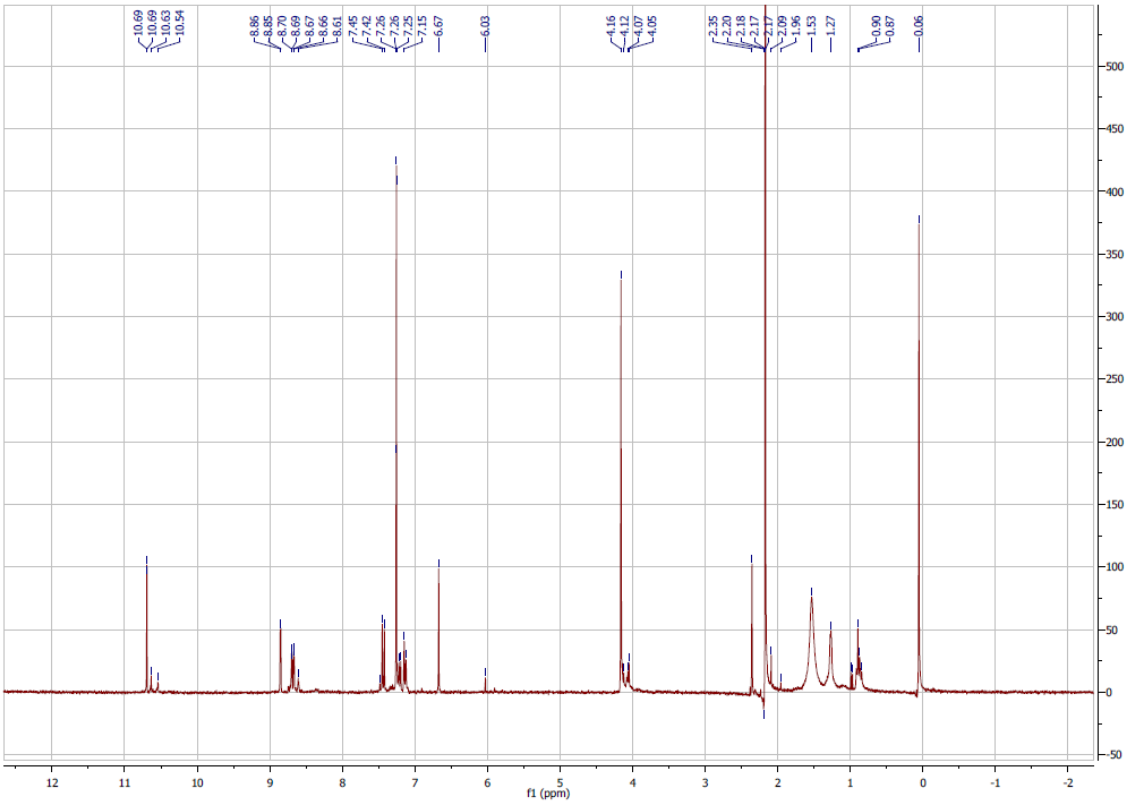

Figure 1. ^{1}H NMR recorded on a 300 MHz spectrometer.

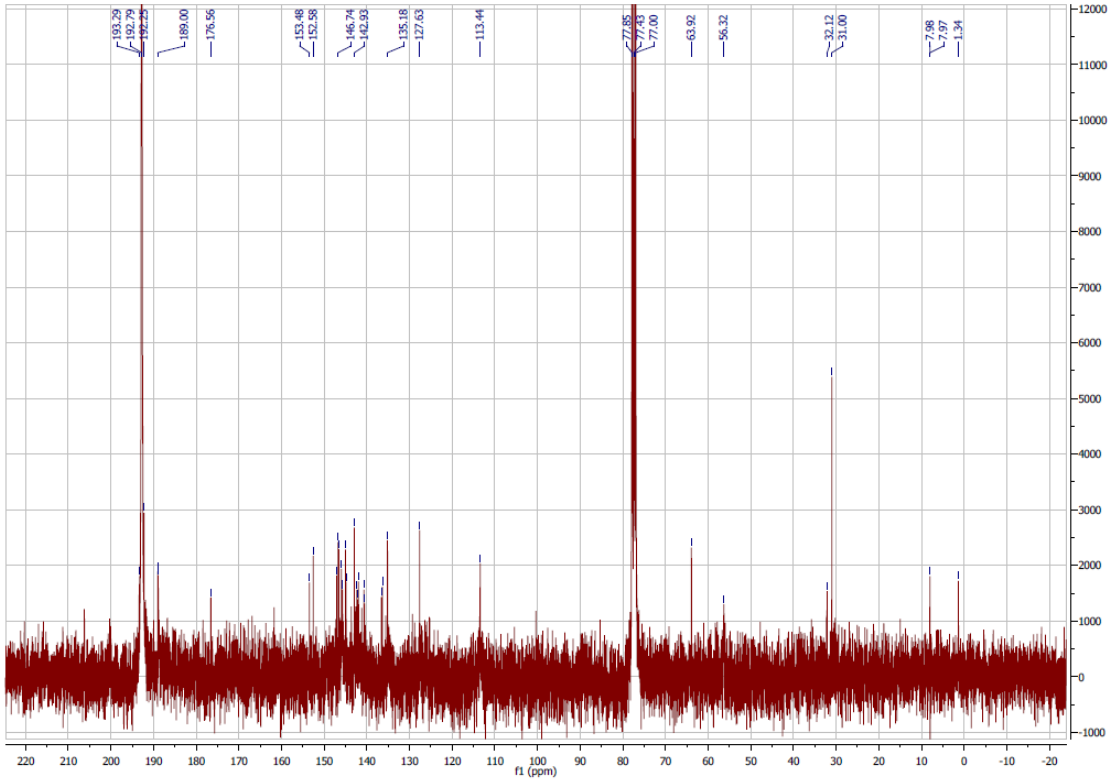

Figure 2. ^{13}C NMR recorded on a 300 MHz spectrometer.

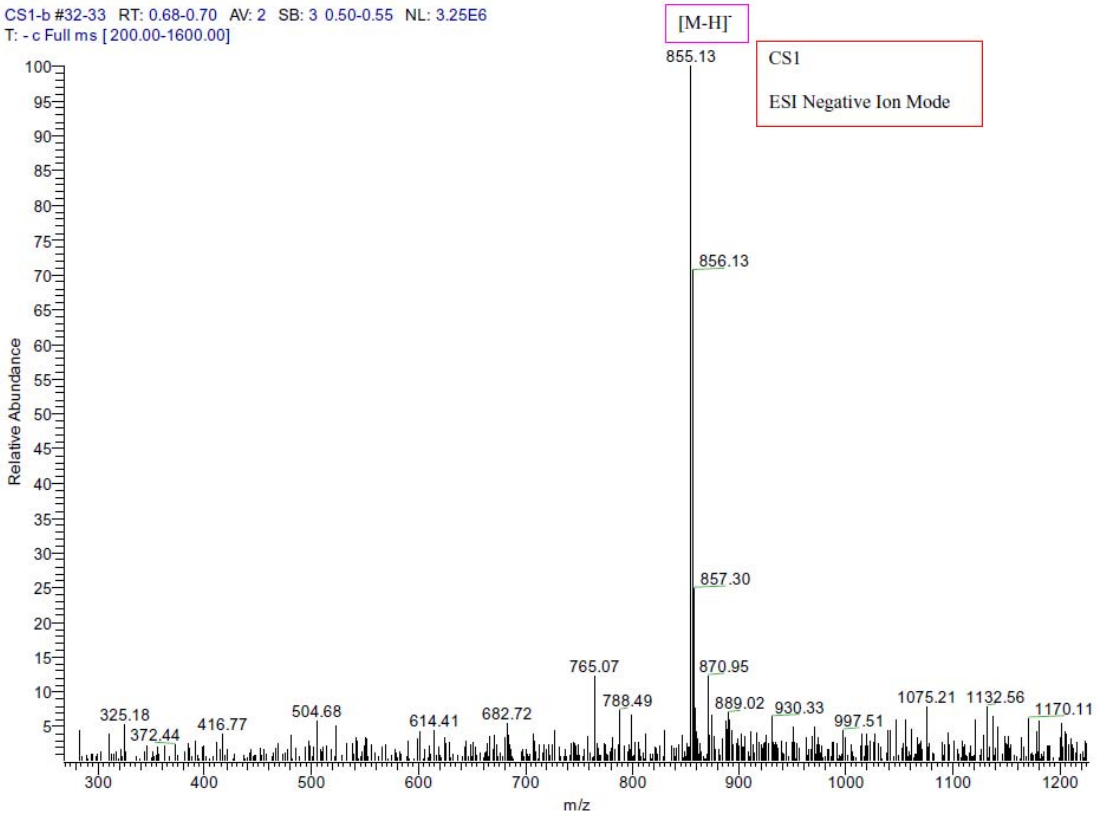

Figure 3. ESI negative ion mode spectrum. *m/z* calc $C_{68}H_7O_2$: 855.78 (±0.007) [M-H]- found 855.13.

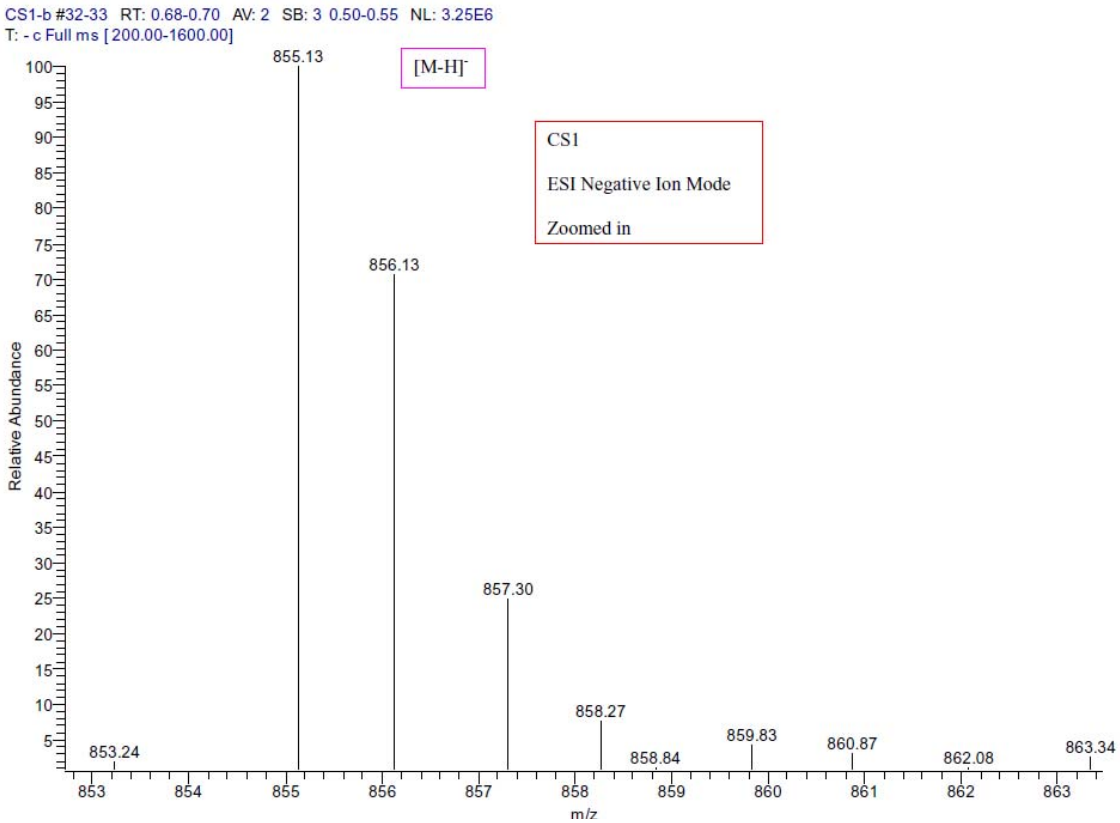

Figure 4. ESI negative ion mode spectrum of the isotopoic peaks between 856 and 890 m/z.

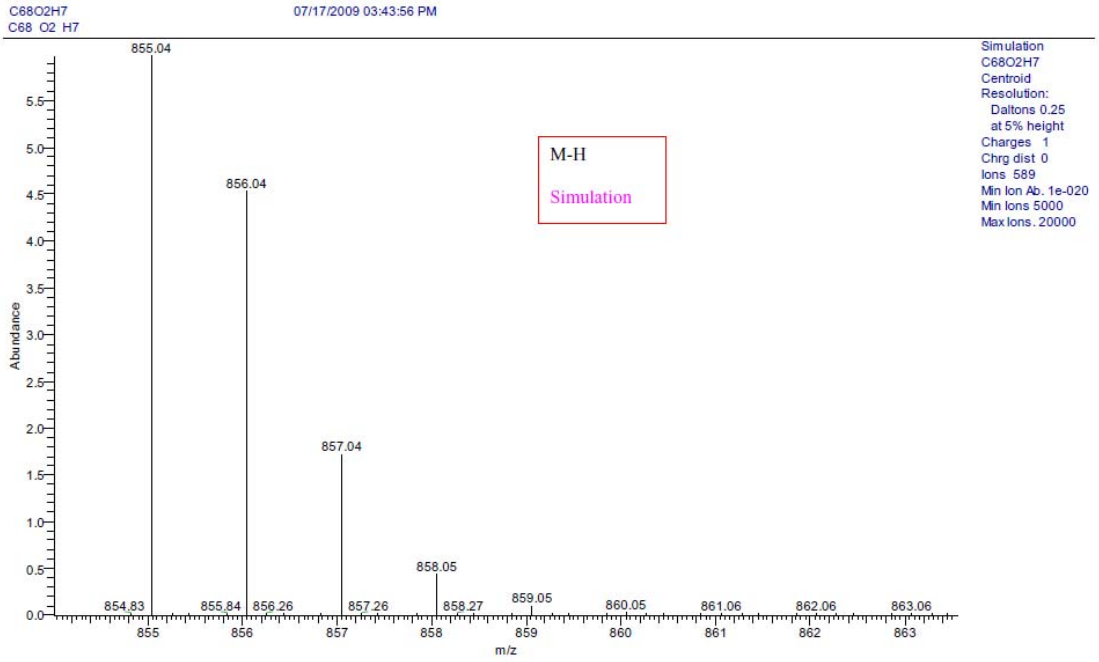

Figure 5. Simulated ESI spectrum of the peaks between 856 and 890 m/z.

to determine if one of them can be assigned to the phenyl carbon or a carbon of the fullerene. A peak at 56 ppm corresponds to the carbon of the methyl ether. The peak at 189 ppm can be assigned to the aldehyde carbon.

The ESI spectrum can be found in Figures 3 and 4. A simulated spectrum for a molecule with the composition of **1** ($C_{68}O_2H_7$) is shown in Figure 5. The full spectrum exhibits one large peak at m/z = 855.13 which is in agreement with the calculated molecular weight of **1** (calc $C_{68}H_7O_2$: 855.78). The smaller peaks at 856 and 857 correspond to isotopic fragments. The simulated fragmentation pattern is in close agreement with the experimental data. These data confirm the identity and structural characteristics of **1**.

Purification of **1** using column chromatography was relatively simple as the addition of the methoxysalicylaldehyde to the fullerene drastically altered the polarity of the molecule. C_{60} and more nonpolar side products eluted much faster than **1**. Although **1** appeared as a single band on the column and during TLC analysis, there appear to be impurities present in the ^{1}H NMR spectrum. Two small peaks at 10.63 and 10.64 ppm correspond to shifted aldehyde protons. These peaks indicate the presence of either an isomer or a multiple addition product, where the salicyladehyde was added more than once to the fullerene.

The next step is to deprotect the methyl ether. A deprotecting agent which tolerates an aldehyde group must be used. 2-diethylamino ethanethiol is a deprotecting agent which gives high yields and tolerates a number of functional groups including aldehydes.[17] Following deprotection of the methyl ether, the oxime can be formed by the reaction of the aldehyde with hydroxylamine.

5.4 Conclusion

A salicyaldehyde functionalized fullerene has been synthesized in low yield from the rhodium catalyzed arylation of C_{60}. Its composition confirmed with ^{1}H and ^{13}C NMR and ESI mass spectrometry. Future work will involve deprotection of the methyl ether and the subsequent formation of an oxime with hydroxylamine.

References

1. Christou, G.; Gatteschi, D.; Hendrickson, D. N.; Sessoli, R., Single-molecule magnets. *Mrs Bulletin* **2000,** 25, (11), 66-71.

2. Sessoli, R.; Tsai, H. L.; Schake, A. R.; Wang, S. Y.; Vincent, J. B.; Folting, K.; Gatteschi, D.; Christou, G.; Hendrickson, D. N., High-Spin Molecules - [Mn12o12(O2cr)16(H2o)4]. *Journal of the American Chemical Society* **1993,** 115, (5), 1804-1816.

3. Sessoli, R.; Gatteschi, D.; Caneschi, A.; Novak, M. A., Magnetic Bistability in a Metal-Ion Cluster. *Nature* **1993,** 365, (6442), 141-143.

4. del Barco, E.; Kent, A. D.; Hill, S.; North, J. M.; Dalal, N. S.; Rumberger, E. M.; Hendrickson, D. N.; Chakov, N.; Christou, G., Magnetic quantum tunneling in the single-molecule magnet Mn-12-acetate. *Journal of Low Temperature Physics* **2005,** 140, (1-2), 119-174.

5. Zobbi, L.; Mannini, M.; Pacchioni, M.; Chastanet, G.; Bonacchi, D.; Zanardi, C.; Biagi, R.; Del Pennino, U.; Gatteschi, D.; Cornia, A.; Sessoli, R., Isolated single-molecule magnets on native gold. *Chemical Communications* **2005**, (12), 1640-1642.

6. Ni, C.; Shah, S; Hendrickson, D. H.; Bandaru, P. R., Enhanced differential conductance through light induced current switching in Mn-12 acetate molecular junctions, *Applied Physics Letters*, **2006**, 89, 21, 212104

7. Stamp, P. C.; Gaita-Arino, A., Spin-based quantum computers made by chemistry: hows and whys, *Journal of Materials Chemistry*, **2009**, 19, 1718-1730.

8. Forro, L.; Mihaly, L., Electronic properties of doped fullerenes, *Reports on Progress in Physics* **2001,** 64, 649.

9. Boyd, P. D. W.; Reed, C. A., Fullerene-porphyrin constructs, *Accounts of Chemical Research* **2005,** 38, 235.

10. Konarev, D. V.; Kovalevsky, A. Y.; Khasanov, S. S.; Saito, G.; Otsuka, A.; Lynbovskaya, R. N., Crystal structures, EPR spectra, and magnetic properties of a series of ionic multi-component complexes [(TBPDA)(2)center dot(C-60(center dot-))center dot(D+)] (D = Cp*Cr-2, Cp*Co-2, TDAE), *European Journal of Inorganic Chemistry* **2005**, 4822.

11. Coronado, E.; Galan-mascaros, J. R.; Gomez-Garcia, C. J.; Laukhin, V., Coexistance of ferromagnetism and metallic conductivity in a molecule-based layered compound, *Nature*, **2000**, 408, 23, 447-449.

12. Fagan, P. J.; Krusic, P. J., Evans, D. H.; Lerke, S. A.; Johnston, E.; Synthesis, chemistry, and properties of a monoalkylated buckminsterfullerene derivatve, tert-BuC60 anion, *Journal of the American Chemical Society*, **1992**, 114, 9697-9699.

13. Matsuo, Y.; Iwashita, A.; Abe, Y.; Li, C.Z.; Matsuo, K.; Hashiguchi, M.; Nakamura, E. Regioselective Synthesis of 1,4-Di(organo)[60]fullerenes through DMF-assisted monoaddition of silylmethyl Grignard reagents and subsequent alkylation reaction, *Journal of the American Chemical Society*, **2008**, 130, 46, 15429-15436.

14. Yurovskaya M. A.; Ovcharenko, A. A.; 1,3-dipolar cycloaddition as a method for synthesis of fullerene C60 derivatives containing heterocyclic moieties, *Khimiya Geterotsiklicheskikh Soedinenii*, **1998**, 3, 291-297.

15. Nambo, M.; Noyori, R.; Itami, K. Rh-Catalyzed Arylation and Alkenylation of C60 Using Organoboron Compounds. *Journal of the American Chemical Society*, **2007**, 129, 8080-8081.

16. Giordano, G.; Crabtree, R. H. Di-m-chloro-bis(n4-1,5-cyclooctadiene)-dirhodium(i), *Low-valent Complexes of Rh, Ir, Ni, Pd, and Pt*, **1998**, 28, 88-90.

17. Magano, J.; Chen, M. H.; Clark, D. J.; Nussbaumer, T., 2-(Diethylamino)ethanthiol, a New Reagent for the Odorless Deprotection of Aromatic Methyl Ethers, *The Journal of Organic Chemistry*, **2006**, 71, 18, 7103-7105.